# Electron pair emission from surfaces upon $He^{2+}$ impact

DISSERTATION

zur Erlangung des akademischen Grades

doctor rerum naturalium
(Dr. rer. nat.)
genehmigt durch

Naturwissenschaftlichen Fakultät II - Chemie und Physik
der Martin-Luther-Universität Halle-Wittenberg

vorgelegt von
Herrn Changhui Li
geboren am 13.06.1982 in Liaoning, China

Gutachter:

1. Prof. J. Kirschner
2. Prof. H. Winter
3. Prof. W. Widdra

Verteidigungsdatum: 11.11.2014

# Abstract

The objective of this thesis is to investigate the neutralization of $He^{2+}$ in front of a metal surface. According to a commonly used sequential model, $He^{2+}$ is firstly converted to $He^{+}$ and then to $He^{0}$. Two electrons are emitted incoherently by the two corresponding neutralization steps. As the ionization potentials of $He^{2+} \rightarrow He^{+}$ and $He^{+} \rightarrow He^{0}$ are 54.4 eV and 24.6 eV, respectively, the electron pair prefers one fast electron and one slow electron. In other words, a very unequal energy sharing between the two electrons is expected. The electron pair emission, upon the impact of 10 eV normal incident $He^{2+}$ ions onto Ir(100) and Fe(100)-p(1×1)O surfaces, was studied by a two-electron coincidence spectrometer. In the two-electron coincidence spectra, we have found the electron pairs can be understood by the sequential model. However, we have also found the electron pair emission can only be explained by a non-sequential process. For these events, the two electrons can share the energy available to them continuously. To explain the non-sequential process, the correlation between the two emissions should be taken into account.

# Zumsammenfassung

Der Gegenstand dieser Dissertation ist die Untersuchung der Neutralisierung von $He^{2+}$ an einer Metalloberfläche. Nach einem sequentiellen Modell wird $He^{2+}$ zunächst in $He^{+}$ und dann zu $He^{0}$ überfhrt. Diese zwei Neutralisierungsschritte führen zu einer inkohärenten Emission von zwei Elektronen. Die Ionisierungspotenziale von $He^{2+} \rightarrow He^{+}$ und $He^{+} \rightarrow He^{0}$ sind 54.4 und 24.6 eV. Die Elektronenpaaremission resultiert daher in einem schnellen und einem langsamen Elektron. Anders ausgedrückt bedeutet dies eine sehr ungleiche Energieaufteilung zwischen den beiden Elektronen. Mittels senkrechtem Einfall von 10 eV $He^{2+}$-Ionen wurde die Elektronenpaaremission von Ir(100) und Fe(100)-p(1x1)O Oberflächen untersucht, wozu ein Zwei-Elektronenspektrometer benutzt wurde. Die Zwei-Elektronenspektra haben Beiträge, die mit dem sequentiellen Modell in Einklang stehen. Zusätzlich existiert Paaremission, was nur mittels eines nicht-sequentiellen Przeß erklärbar ist. Für diese Beiträge zeigt sich eine kontinuierliche Energieaufteilung. Eine Erklärung des nicht-sequentiellen Pfades bedarf der Bercksichtigung der Korrelation zwischen der Emission der beiden Elektronen.

# Contents

**1 Introduction** **1**

**2 Basic Concepts** **5**

2.1 Fundamentals of the ion-surface interaction . . . . . 5
  2.1.1 Classical-over-the-barrier model . . . . . 5
  2.1.2 Electronic transitions . . . . . 8
  2.1.3 Atomic energy level shift . . . . . 11
  2.1.4 Conventional neutralization scheme of $He^+$ near a metal surface 13
  2.1.5 Conventional neutralization scheme for $He^{2+}$ near a metal surface 13
2.2 Timescales of electron excitations . . . . . 16
  2.2.1 Timescale of escaping from the target . . . . . 18
  2.2.2 Timescale of screening . . . . . 20
  2.2.3 Timescale of quantum interference between different paths . . . 23
  2.2.4 Timescale of electron capture in ion neutralization . . . . . 24

**3 Experimental Techniques** **27**

3.1 Principle of the two-electron coincidence experiment . . . . . 27
  3.1.1 Arrival time difference . . . . . 27
  3.1.2 The determining factors for the true/random ratio . . . . . 28
3.2 Coincidence spectrometer . . . . . 29
  3.2.1 Principle of the concentric hemispherical analyzer . . . . . 30
  3.2.2 Detection system . . . . . 33
  3.2.3 Data acquisition electronics . . . . . 35
3.3 Ion source . . . . . 36
  3.3.1 Ionizer . . . . . 36
  3.3.2 Wien-filter . . . . . 37
  3.3.3 Retarding-optics . . . . . 37
3.4 The UHV system . . . . . 38
3.5 Sample preparation . . . . . 40

**4 Experimental results** **43**

4.1 Non-coincidence spectra . . . . . 43
4.2 Coincidence spectra of Ir(100) . . . . . 49
4.3 Coincidence spectra of Fe(100)-p(1×1)O . . . . . 61

**5 Discussion** **71**

**6 Conclusion** **81**

# Chapter 1

# Introduction

For condensed matter physics, the electron-electron correlation is at the heart of physical phenomena, like magnetism, metal-insulator transition, superconductivity and multiferroicity. The idea of electron-electron correlation is to say that, due to the electron interaction, which is originating from the Pauli principle and Coulomb interaction, the electrons can not be treated as independent particles. Take the magnetism and Mott insulator for example. In ferromagnet, the exchange interaction can align the electron spin of different sites parallel to each other. For a Mott insulator, the repulsive Coulomb interaction of two electrons in the same site is very large, such that the electrons can not hop freely between the next neighbor sites, consequently forming an insulating phase. In general, the electron-electron correlation can be understood through the concept of the exchange-correlation (xc)-hole [1, 2], a region of reduced charge density around each electron. According to the Pauli principle, two electrons with the same spin, can not be located at the same position. In addition, the repulsive Coulomb interaction tends to keep the two electrons apart from each other. In other words, the electrons are not randomly distributed in solids, and each electron is screened from each other. The shape of the xc-hole determines the exchange-correlation energy, which is the central part for local-density approximations (LDA) [3], a highly successful theoretical framework in condensed matter physics.

The study of electron pair emission, which can be excited by the impact of electrons (e,2e) and photons ($\gamma$,2e), has been proven to be an effective way to get access to the electron-electron correlation. First, the intensity of the pair emission is directly related to the electron-electron correlation strength [4]. Without electron-electron correlation, the pair emission intensity will vanish [5], and the pair intensity has been found to be enhanced in strongly correlated systems [6, 7]. In addition, the energy and angular distributions of the two emitted electrons contain the important information of the electron-electron correlation. For example, in the (e,2e) [8, 9] and ($\gamma$,2e) experiments [10, 11], for the given energies of the two emitted electrons and a given emission direction of one electron, the angular distribution of the other electron reflects the xc-hole in the momentum space. This concept is not accessible with single electron spectroscopy.

The study of the pair emission excited by different primary particles can help to investigate the electron-electron correlation in different aspects. For example, by using spin polarized electrons to excite the electron pairs from a magnetic surface, we can disentangle the contributions of exchange and Coulomb interaction to the xc-hole [12, 13]. The principle is that, for two electrons with parallel spins, both exchange and Coulomb interaction play a role, whereas for two electrons with anti-parallel spins, only the Coulomb interaction is relevant. Therefore, from this aspect, spin polarized electrons have an advantage over non-spin polarized electrons and photons. Another example is the so-called (p,ep) process [14, 15], in which a primary positron (p) excites a positron-electron pair. In this process, the correlation effect manifests itself also in a different manner than the counterpart (e,2e) process. Because, positron and electron are distinguishable, the Pauli principle is absent. Hence, it can also disentangle exchange interaction and Coulomb interaction. In this case, a magnetic sample is not a must. In addition, the Coulomb interaction between a positron and an electron is attractive, therefore the positron-electron interaction can form a correlation hill [15], in contrast to the xc-hole for the electron-electron interaction.

In this thesis, we will demonstrate a new mechanism for the pair emission, which is induced by the impact of slow $He^{2+}$ ions onto a metal surface, called ($\alpha$,2e). The electrons are emitted by the potential energy released in the ion neutralization. This kind of electron emission is called potential emission (PE) [16, 17].

PE contains important information of the electronic structure of the surface, for instance, the surface density-of-states [18, 19]. PE arising from the collisions of singly charged ions (SCI) on metal surfaces was firstly reported by Oliphant in 1929 [20] and then has been thoroughly studied by Hagstrum in 1950s [16, 18, 19, 21]. The relevant electronic transitions can be depicted by several competing processes, for example, direct Auger capture (AC) [16], resonant capture (RC) followed by Auger de-excitation (AD) [22] or Autoionization (AI) [23], and more recently found plasmon-assisted electron emission [24–26].

For the collisions of multiply charged ions (MCI) on metal surfaces, the increased charge state make the interacting process more complicated and several electrons can be emitted by a single collision. The study of electron-emission statistics shows that the total electron yield $\gamma$ (mean number of the emitted electrons by a single collision) is proportional to the charge state and potential energy [27, 28]. The analyses of the charge state of the reflected ions [29, 30] indicates that a nearly fully neutralized state is achieved.

The ion neutralization takes place in the vicinity of the metal surface. The neutralization distance can be estimated by the so-called classical-over-the-barrier (COB) model [31]. This model assumes that, the neutralization (charge transfer) starts when the one-electron potential barrier separating the surface and the ion is lowered down to the Fermi level. This sets up an upper limit for the neutralization distance. A typical value is several Å with respect to the topmost layer. When an ion is approaching a metal surface, the ion is attracted to the surface by its own image charge inside the solid. This sets up a upper limit of time (typically a few tens to hundreds fs) for the ion neutralization. In other words, during the neutralization of MCI, several electrons are emitted in a short limited time. For example, the impact of $Th^{79+}$ ion on a clean gold surface [28] can induce the emission of about 280 electrons in less than $10^{-13}$ s. The neutralization of MCI is conventionally described by a sequential model. In this model, the above mentioned electronic transitions for SCI are treated as fundamental transitions. The MCI is neutralized by a sequence of these transitions [23, 30–35], step by step. In this model, usually, it requires many "steps" to achieve the final full neutralized state. As an example, for the collision of $N^{6+}$ ions on a Cu(100) surface, in theory, at least 15 steps are needed [33].

Similar sequential descriptions are used in other processes. For example, in the two-photon double ionization of He, He is double ionized sequentially by two photons, He $\xrightarrow{\hbar\omega}$ $He^{+}(1s) + e_1 \xrightarrow{\hbar\omega} He^{2+} + e_2$. In the Auger effect upon photon excitation, it assumes that the emission of a photoelectron is followed by an Auger electron emission. These sequential models are based on an important assumption: there is a well defined intermediate state between two successive transitions. For two-photon double-ionization, the intermediate state is $He^{+}(1s)$, and for the Auger effect, it is the so-called core-hole state after photoemission. The intermediate state serves to span all the excited single-electron states. If this assumption is invalid, the sequential description is inappropriate. In the two-photon double-ionization, since the first and second ionization energy of He is 24.6 eV and 54.4 eV, respectively, the sequential model requires that the photon energy should be large enough to eject the second electron, $\hbar\omega > 54.4$ eV. However, it have been found that, He can be double ionized by an intense sub-femtosecond photon pulse, with an energy of $39.5 \text{ eV} < \hbar\omega < 54.4 \text{ eV}$ [36–38]. This can only be explained by a non-sequential path. The study of the recoil-ion momentum distribution of $He^{2+}$ has revealed that in the non-sequential path, the two electrons are emitted almost simultaneously, with an equal energy [36]. In the Auger effect, it has been demonstrated that if the lifetime of the core-hole state after photoemission is not long enough, the emitted two electrons can interact each other in the continuum, for example, by Coulomb interaction [39–41]. This leads to a continuously energy sharing between the two electrons. In other words, the energy of a single electron is not identical, and it is meaningless to distinguish which electron is Auger-electron or photoelectron. In this case, the sequential description for the Auger effect is inappropriate.

The sequential neutralization model for MCI is questionable. For one hand, in the sequential model, the time interval between two successive steps can not be infinitely small, since building up of a well defined intermediate state requires a finite time. For another hand, MCI is neutralized in a short limited time, leading to the emission of several electrons. Therefore, it is very likely that the electrons involved in different emissions interact with each other during the neutralization. In this case, the sequential description is inappropriate. In the previous experiments, the non-sequential paths have been observed. Typical examples are the so-called three-electron Auger [42] and two electron-one photon transitions [43], in which the two outer shell electrons can fill the two inner shell vacancies instantaneously, leading to the emission of one electron or one photon, respectively, instead of by two successive Auger or radiative decays.

In order to study the neutralization of MCI beyond the sequential model, $He^{2+}$ is a good choice. First, an obvious reason is that, in principle, $He^{2+}$ has the simplest sequential neutralization model of MCI. According to the literature [23, 30, 35], $He^{2+}$ is firstly converted to $He^{+}$ and then to $He^{0}$. Two electrons are emitted incoherently in the two corresponding neutralization steps. Second, the sequential model predicts there is no relationship between the two emitted electron, and our two-electron coincidence spectroscopy can test it in the energy space. For example, in a previous double photoemission study of a Cu(100) surface we proved that the Auger decay proceeds via a non-sequential process rather than a sequential process. The evidence was that the two emitted electrons conserve the energy available to them continuously [44].

For the above motivation, the collisions of $He^{2+}$ ions on Ir(100) and Fe(100)-p(1×1)O (referred to as O/Fe(100)) surfaces are good candidates for the following reasons. First, compared to the low work function surfaces, the neutralization model for the high work function surfaces is simpler (Ir(100) 5.67 eV [45], O/Fe(100) 4.9 eV [46]) [23]. Second Ir(100) and O/Fe(100) surfaces are relatively inert, and can stay clean in Ultra High Vacuum (UHV) for one day. This is a crucial requirement. On one hand, the ion neutralization experiments are extremely sensitive to the adsorbates [47, 48]. On the other hand, coincidence experiments usually suffer from low coincidence count rate and then the acquisition time is usually very long (several weeks in the context of this work).

# Chapter 2

# Basic Concepts

## 2.1 Fundamentals of the ion-surface interaction

### 2.1.1 Classical-over-the-barrier model

For the ion-surface interaction, one conventional model is the so-called classical-over-the-barrier (COB) model [31]. The basic idea behind is that when the electron potential barrier between an ion and a surface is lowered down to the Fermi level, the electron capture (i.e. from the surface to the ion) can take place (classical picture). This model can provide some basic parameters of the ion-surface interaction. For example, it gives the distance to the surface where electron capture starts. Furthermore, the upper time limit for the ion-surface interaction process, and the kinetic energy gain of the primary ion is given.

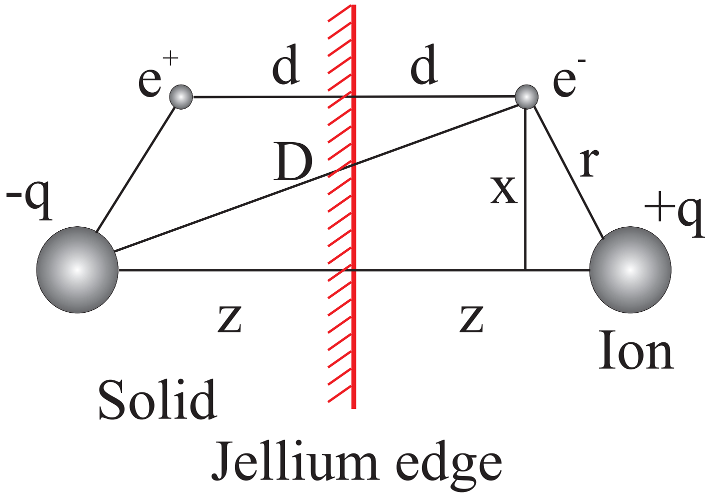

**Figure 2.1:** Sketch of the ion-surface interaction, using the concept of the image charge. A primary ion and an "active" electron have induced the corresponding image charges inside the solid, with the jellium edge being the reference plane.

When a primary ion is approaching a metal surface, the surface electrons will respond to the electric field of this ion in order to screen it. For a large ion-surface distance and a small ion velocity ($v \ll$ the Fermi velocity) [51], this response can be described by the concept of the image charge [52]. As shown in Fig. 2.1, an ion (charge $+q$, distance $z$) above the surface can induce an image charge (charge $-q$, distance $-z$) inside the solid, and so does an "active" electron. The concept of the image charge satisfies the electrostatic boundary condition, that the electric field along the metal surface must be zero. It should be noted that the reference plane is localized at the jellium edge [53], where the electron density drops to half of its bulk value. The jellium edge is about half a lattice constant outside the topmost layer. In this thesis, we take the value of 3 a.u. to be consistent with the literature [54].

One consequence of the ion-surface interaction is the reduction of the one electron potential barrier between the ion and the metal surface. For the situation shown in Fig. 2.1, the electric potential of the electron above the surface can be described as (atomic units, see Appendix B),

$$V = V_{i-e} + V_{i-e}^{image} + V_{e-e}^{image} = -\frac{q}{\sqrt{x^2+(z-d)^2}} + \frac{q}{\sqrt{x^2+(z+d)^2}} - \frac{1}{4d}, \tag{2.1}$$

where $V_{i-e}$, $V_{i-e}^{image}$ and $V_{e-e}^{image}$ are the ion-electron, image ion-electron and image electron-electron interaction potentials, respectively. The electron potential landscape is exemplified in Fig. 2.2, for a doubly-charged ion at a distance $z = 11$ a.u. (panel a) and 6 a.u. (panel b), respectively. The potential barrier separating the surface and the ion is determined by a saddle point, which is indicated by a red arrow. The plot shows that the potential barrier decreases, when the ion is approaching the surface.

For the position of the saddle point, $x_s = 0$ a.u. and $d_s$ is determined by setting the derivative of the $V(d)$ to zero,

$$\frac{\partial V(d)}{\partial d} = 0. \tag{2.2}$$

The solution is,

$$d_s^2 = \frac{-(8q+2) + 8\sqrt{q^2+q}}{2(8q-1)} z^2. \tag{2.3}$$

For a multiply charged ion (MCI), $d_s$ can be approximated by $d_s \approx z/\sqrt{8q}$, and $V(d_s) \approx -\sqrt{2q}/z$ (for $q = 2$, only a error of 8% is made). According to the COB model, electron capture can take place when the effective barrier (-$V(d_s)$) is lowered down to the Fermi level. This means $\sqrt{2q}/z = W$. Thus, the critical distance $z_c$ is given by,

$$z_c = \frac{\sqrt{2q}}{W}. \tag{2.4}$$

For a MCI, of which the neutralization process is conventionally described by a sequence of several steps, the critical distance $z_c$ indicates where the neutralization starts or where the first neutralization step can take place. For a primary $^3$He$^{2+}$ ion (the case in this thesis) impact onto a metal surface with workfunction $W = 5$ eV, the numerical result is $z_c = 11$ a.u. (5.8 Å) with respect to the jellium edge, $z_c^t = 14$ a.u. (7.4 Å) with respect to the topmost layer.

Another consequence of the ion-surface interaction is the acceleration of the ion towards the surface, which is due to the Coulomb interaction between the real ion and

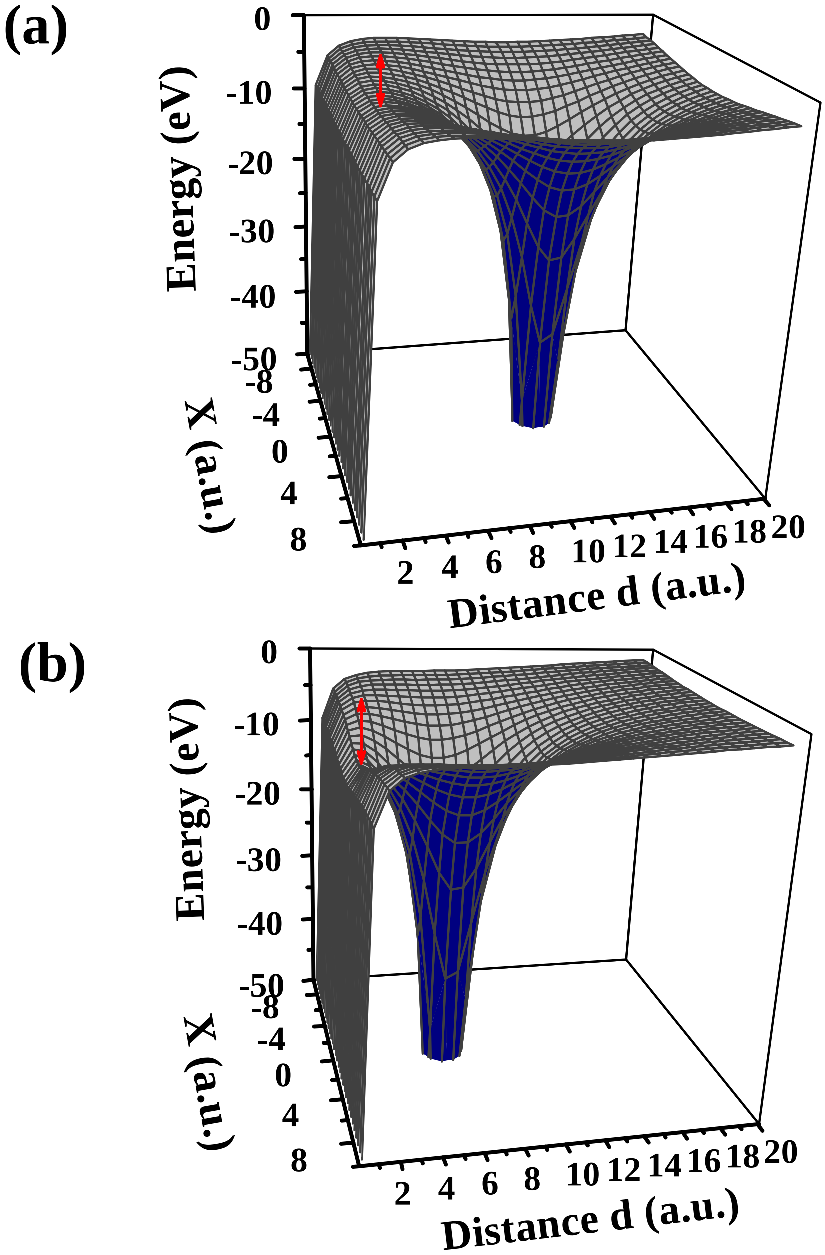

**Figure 2.2:** One-electron potential for a doubly-charged ion in front of a metal surface, at a distance of 11 a.u. (upper) and 6 a.u. (lower), respectively. The red arrow indicates the saddle point, and the length represents the effective barrier separating the surface and the ion.

the image ion, referred to as the image interaction. The attractive force acting on the ion is,

$$F_{im} = -\frac{q^2}{4z^2} \ . \tag{2.5}$$

The ion can be accelerated until fully neutralized. The acceleration process can be separated into two regions: the one goes from infinity to the critical distance ($z_c$), and the one starts at $z_c$ until the end of the ion neutralization process. The calculation of the first part has been just demonstrated, while the second one is complicated. However, the timescale for the neutralization process is just in the order of fs, therefore, for simplicity we can neglect the acceleration in the second process. In other words, the image acceleration disappears once the neutralization process starts, and the kinetic energy gain $E_{im}$ and the final velocity of the ion $v_f$ are,

$$E_{im} = \int_{z_c}^{\infty} \frac{q^2}{4z^2} \mathrm{d}z \ , \tag{2.6}$$

and

$$v_f = \sqrt{\frac{2(E_{im} + E_0)}{m}} \ , \tag{2.7}$$

where $E_0$ is the initial kinetic energy. For a primary $^3\mathrm{He}^{2+}$ with $E_0 = 10$ eV, the numerical results of the final kinetic energy and velocity are 11.3 eV and 0.27 Å/fs.

After the neutralization process starts, there is an upper time limit for the ion to be in front of the surface, which is determined by,

$$t_l = \frac{z_c^t}{v_f} \ . \tag{2.8}$$

For the above mentioned $\mathrm{He}^{2+}$, the numerical result is about $t_l = 27$ fs. According to literature [30], the majority of the reflected helium particles (above 99%) are fully neutralized, and the neutralization takes place above the surface. This indicates the timescale of the whole neutralization process of $\mathrm{He}^{2+}$ should be less than 27 fs. It should be noted that, even if the initial normal velocity of the ion is zero, there is still a non-zero normal velocity for the primary ion due to the image interaction. For example, for a $\mathrm{He}^{2+}$ with almost zero kinetic energy, the upper limit interaction time is 80 fs. Therefore, the neutralization time for a MCI near a metal surface is short and limited.

### 2.1.2 Electronic transitions

The electron emission during the ion-surface collision can be classified into two mechanisms [17]: (1) kinetic emission, in which the kinetic energy of the ion is transferred to the valence electrons, and (2) potential emission, in which the potential energy (i.e. from the potential differences) of the ion is transferred to the valence electrons. For slow ions (up to tens of eV), the electronic transitions take place above the surface and the potential emission plays a dominant role. In the context of this thesis, we focus on the potential emission by slow ions, specifically $\mathrm{He}^{2+}$ with a kinetic energy of 10 eV and a potential energy of 79 eV. For the potential emission, the fundamental electronic transitions have been established in the pioneering work of Hagstrum [16, 18, 19, 21].

The prominent types of electronic transitions are shown in Fig. 2.3. $E_F$, $W$ and $E_b$ are the Fermi level, work function of the surface and the binding energy of the projectile atomic level, respectively. When a primary ion is close to a metal surface, the atomic levels are shifted. This will be explained in Sec. 2.1.3. These transition models are based on an adiabatic picture (Born-Oppenheimer approximation), which neglects the coupling between the electronic and ion motion. These processes are discussed in the followings.

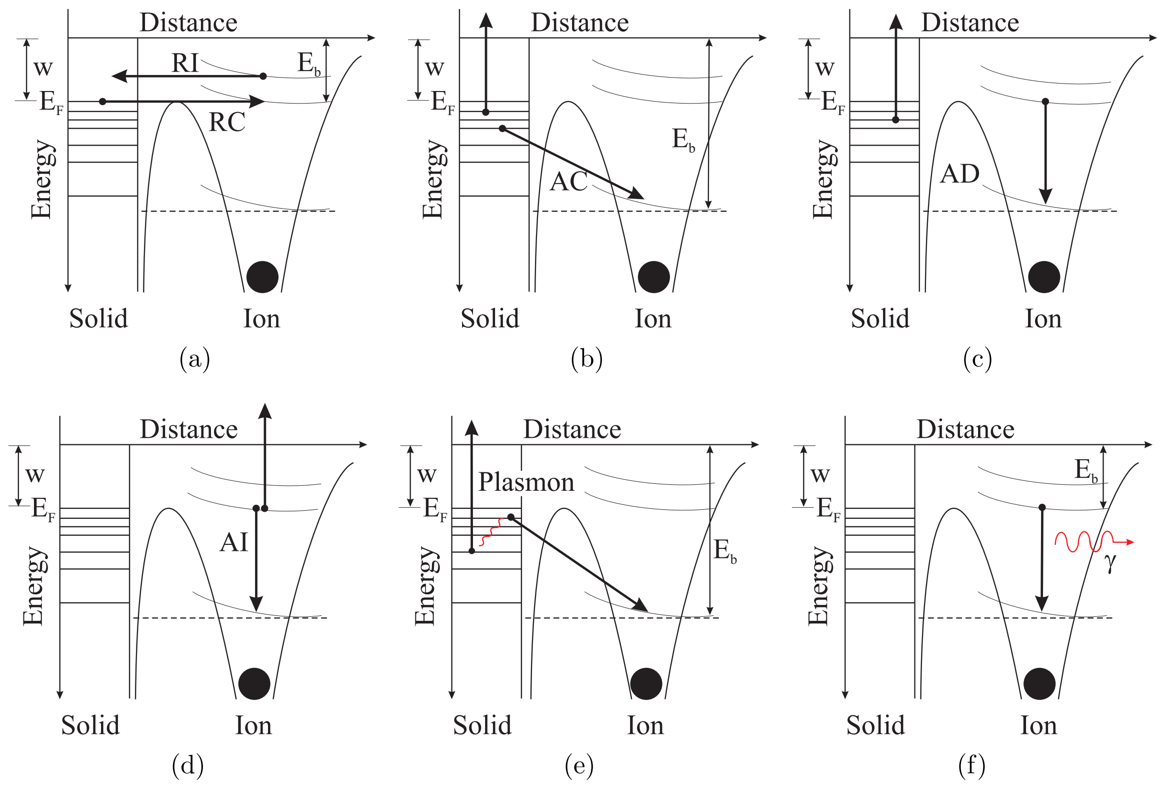

**Figure 2.3:** Schematic representations of the charge transfer processes: (a) resonant transition (RT) (b) Auger capture (AC) (c) Auger de-excitation (AD) (d) autoionization (AI) (e) plasmon-assisted neutralization and (f) radiative de-excitation. $E_F$, $W$ and $E_b$ are the Fermi level, work function and binding energy of the projectile atomic level at infinite distance, respectively. The dashed horizontal line indicates the atomic level for the free ion. In the vicinity of the surface, the atomic levels are shifted due to the image charge effect.

(a) Resonant transitions (RT, Fig. 2.3(a)) are elastic tunneling processes, which include resonant capture (RC) and resonant ionization (RI). In RC, a valence electron can be resonantly captured into an empty projectile atomic level. RC can not induce the emission of electrons but it can act as a precursor for subsequent electron emitting transitions. RI is the opposite process of RC, where an electron from a high-lying level of the excited projectile is transferred to an empty state of the solid. For a MCI, after RC the higher atomic levels are occupied, while the inner levels are still empty, forming a short lived multiply-excited particle, called “hollow atom” [55].

(b) In an Auger capture process (AC, Fig. 2.3(b)), two valence electrons are involved, one is transferred to a deeper empty projectile atomic level, while the other one is emitted into the vacuum with an excess energy. If the two electrons originate from the Fermi level, the emitted Auger electron will have the maximum kinetic energy,

$$\varepsilon_k^{max} = E_b - 2W, \tag{2.9}$$

where $E_b$ is the binding energy (or ionization energy) of the relevant atomic level. Because two electrons of the valence band are involved, the respective energy distribution of the Auger electrons reflects a self-convolution of the surface density-of-states (SDOS).

(c) Auger de-excitation (AD, Fig. 2.3(c)) takes place after one valence band electron is captured by the ion. The excited projectile electron interacts with a surface electron, the result is one electron being transferred into the lower atomic level, one electron being emitted. The maximum kinetic energy of the Auger electron is,

$$\varepsilon_k^{max} = E_{b,f} - E_{b,i} - W, \tag{2.10}$$

where $E_{b,f}$ and $E_{b,i}$ are the binding energies for the final and initial atomic states. The respective energy distribution of the Auger electrons directly reflects the SDOS.

(d) Autoionization (AI, Fig. 2.3(d)) is an intra-atomic process. It takes place after the formation of a "hollow atom" by RC. In an AI process, one projectile electron is transferred from the outer orbit of the ion to an inner orbit, while another electron (Auger electron) is emitted to the vacuum. The kinetic energy of the Auger electron is given by,

$$\varepsilon_k = E_{b,f} - E_{b,i}. \tag{2.11}$$

For the narrow atomic levels, the respective energy distribution of the Auger electron exhibits sharp features.

(e) Plasmon-assisted neutralization (Fig. 2.3(e)). When one valence electron is captured by the projectile, the rapid switch of the potential in the surface can generate a surface/bulk plasmon, $\hbar\omega$, called potential excitation [25, 26]. After several oscillations, this plasmon will decay, in some cases, by emitting a valence electron. The maximum kinetic energy of this electron is,

$$\varepsilon_k^{max} = \hbar\omega - W. \tag{2.12}$$

It should be noted that the plasmon-assisted neutralization is a resonant process, which can only happen when the resonant condition is fulfilled. The resonant condition is

$$\hbar\omega = E_b - \delta - W - \varepsilon, \tag{2.13}$$

where $\delta$ is the potential shift by the image interaction and $E_b$ is the binding energy of the captured valence electron, with respect to the Fermi level. Once energetically allowed, the plasmon-assisted neutralization will play an important role in the ion neutralization [25, 26].

(f) Radiative de-excitation (Fig. 2.3(f)) takes place after the formation of a excited projectile state by RC or AC. In a radiative de-excitation, a photon is emitted, taking away the excess energy given by the de-excitation of the projectile. As the radiative lifetimes for the neutralization of SCI and DCI are about $10^{-8}$s [34], $10^6$ times longer than the transition time for the Auger process, the radiative deexcitation (RD) process can be neglected in this thesis.

In the case of the neutralization of $\text{He}^{2+}$, the above electronic transitions can be classified into three types, resonant (RC and RI), Auger (AC, AD, AI) and plasmon-assisted transitions. Resonant transitions can not induce electron emission. Whereas, one electron can be emitted during an Auger type or a plasmon-assisted transition.

### 2.1.3 Atomic energy level shift

The atomic energy levels of an ion can be shifted by the presence of a metal surface. When the ion-surface distance is large, the atomic energy level shift can be described by the concept of image charge. Consider that an ion transition takes place at a distance $z$ from the image plane. The rapid change of the ion charge can lead to the change of the charge-image charge interaction potential. Hence, the energy (-$\epsilon(z)$) released in the transition can be expressed by the form,

$$-\epsilon(z) = -\epsilon(\infty) - V_i(z) + V_f(z), \tag{2.14}$$

where $\epsilon(\infty)$ is the potential level for a free ion, $V_i$ and $V_f$ are the charge-image charge interaction potentials of the initial and final states, respectively. We consider an adiabatic picture, in which the surface electrons can respond to the change of the ion charge instantaneously. Then $V_i$ and $V_f$ can be described as,

$$V_i = -\frac{Q_i^2}{4z}, \quad V_f = -\frac{Q_f^2}{4z}. \tag{2.15}$$

The potential level of the ion can be described as,

$$\epsilon(z) = \epsilon(\infty) + \frac{Q_i^2}{4z} - \frac{Q_f^2}{4z}. \tag{2.16}$$

For short distances, the potential energy level shift can be influenced dramatically by the chemical interaction between the ion and metal. In Fig. 2.4, We present a theoretical calculation [56] for the He-1s level shift in front of an Al(100) surface (black), in which the chemical interaction is taken into account. For comparison, we present a red curve generated from the image charge model (Eq. 2.16). For distances larger than 3 a.u. the two curves agree with each other. For distances shorter than 3 a.u. the effect of the chemical interaction starts to appear. When the He-1s level penetrates the electronic charge associated with Al orbitals, the electrostatic interaction with the Al atoms can pull down the He-1s level. At even smaller distances, the He-level and the Al-core wave functions overlap. The Al-core wave functions repel the He-1s level, and shift it to higher energies [56]. It has been observed, the mean atomic level shift for the He-1s potential level in front of a metal surface, like Al [57], Cu [58], is about 2 eV. According to the transition rates of $\text{He}^+ \to \text{He}^0$, see Sec 2.1.4, the most likely neutralization distance is around the jellium edge ($z = 0$). See Fig. 2.4, the energy shift at the distance of $z = 0$ a.u. is 2 eV. This is in accordance with the above observations.

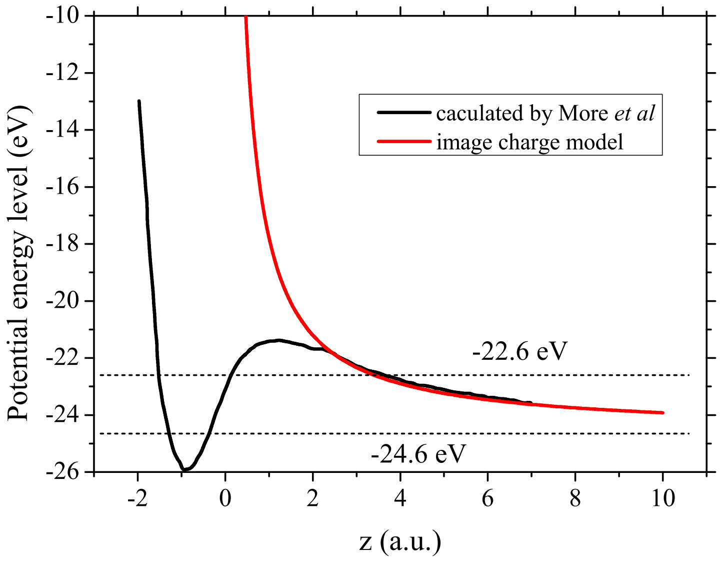

**Figure 2.4:** Position of He-1s energy level as a function of distance $z$ with respect to the jellium edge. The red curve is from the image charge model (Eq. 2.16). The black curve is from Ref. [56], for a $He^+$-Al(100) system. The lower dashed line labels the potential energy level when $z = \infty$. The upper dashed line labels the potential energy shift of 2 eV.

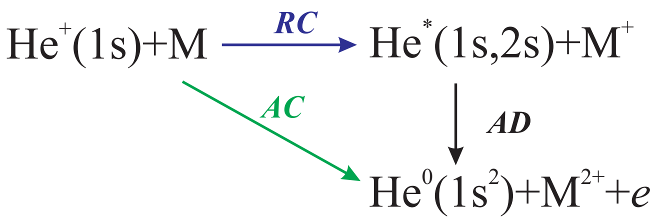

**Figure 2.5:** Neutralization scheme of $He^+$ near a metal surface, via Auger capture (AC), resonant transitions (RC), and Auger de-excitation (AD). M denotes the metal surface.

### 2.1.4 Conventional neutralization scheme of $He^+$ near a metal surface

The conventional neutralization scheme of $He^+$ near a metal surface (M) can be depicted by two competing processes, Auger capture (AC) and Resonant capture (RC) followed by Auger deexcitation (AD), see Fig. 2.5. For the RC, the one-electron potential with respect to the vacuum level is, $E_b(\mathrm{He}^+(1s))$ - $E_b(\mathrm{He}^*(1s,2s))$ = -4 eV, see Table 2.1. This means, for a metal surface with workfunction, $W \geq 4$ eV, the potential level of $\mathrm{He}^*(1s,2s)$ lies above the Fermi level, and the RC is not energetically allowed. Since the workfunction for Ir(100) and O/Fe(100) is 5.67 eV [45] and W=4.9 eV [46], respectively, in this thesis, the AC path is expected to be dominant in the neutralization of $He^+$.

The AC transition rate $(1/\tau)$ is a function of the ion-surface distance $z$ (with respect to the jellium edge). The transition rate $(1/\tau)$ is proportional to the overlap of the conduction band states and the atomic states. In the jellium model, the electron density above the surface is proportional to exp(-$az$), where $a$ is a constant. When the ion-surface distance is large (several Å), the AC transition rate can be expressed by the form,

$$\frac{1}{\tau} = Aexp(-az) \ . \tag{2.17}$$

The information of the neutralization rate can be extracted by measuring the angular distributions and the ion fractions of scattered projectiles [59]. The principle is that, if the transition rate is lower, the fractions of surviving ions after ion-surface collision will be higher, because the ion-surface interaction time is short and limited. In addition, a lower transition rate can bring the neutralization distance more closer to the surface, and the kinetic energy gain in the perpendicular direction is higher (Eq. 2.6). In a glancing incidence geometry, this leads to a larger scattering angle. Therefore, combined with a computer simulation for the classical trajectories of the reflected beams, the information of the transition rate can be deduced. Such a curve is shown in Fig. 2.6, see the black curve. It is for the $He^+$-Ag system, from Ref. [54]. $1/\tau$ is plotted as a function of the ion distance $z$ from the jellium edge, in atomic unit (1 a.u. = 40 $\mathrm{fs}^{-1}$). In this situation, the most likely position for AC is estimated to be at the jellium edge, $z_{AC} = 0$ a.u..

For comparison, we present some recent calculations of AC for the $He^+$-M system in Fig. 2.6. The full black curve is calculated for the $He^+$-Al system, from Ref. [60], with the most likely neutralization distance being $z_s = 1.5$ a.u.. The red curve is calculated for $He^+$-Al, from Ref. [56], with the most likely neutralization distance being $z_s = 0$ a.u.. For these calculations, they agree with each other that the most likely neutralization position is around the jellium edge. The neutralization rates at the jellium edge are slightly different, but all in the range, 0.01 a.u. $\geq 1/\tau \geq$ 0.001 a.u. (2.41 fs $\leq \tau \leq$ 24.1 fs).

### 2.1.5 Conventional neutralization scheme for $He^{2+}$ near a metal surface

Fig. 2.7 shows the sketch of the commonly used neutralization scheme of $He^{2+}$ near a metal surface. The whole neutralization process finally leads to $He^0$+$M^{4+}$, in which in total four electrons are taken from the metal surface, two are transferred to the

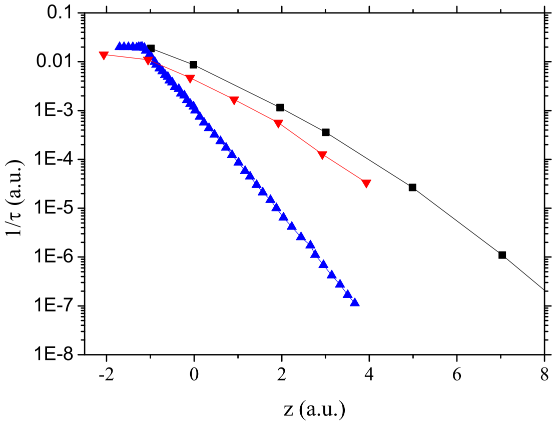

**Figure 2.6:** Auger transition rates ($1/\tau$) in a.u. as a function of the distance ($z$) from the jellium edge. The Blue curve is for $He^+$-Ag from Ref. [54]. The red curve is for $He^+$-Al from Ref. [56]. The black curve is for $He^+$-Al from Ref. [60].

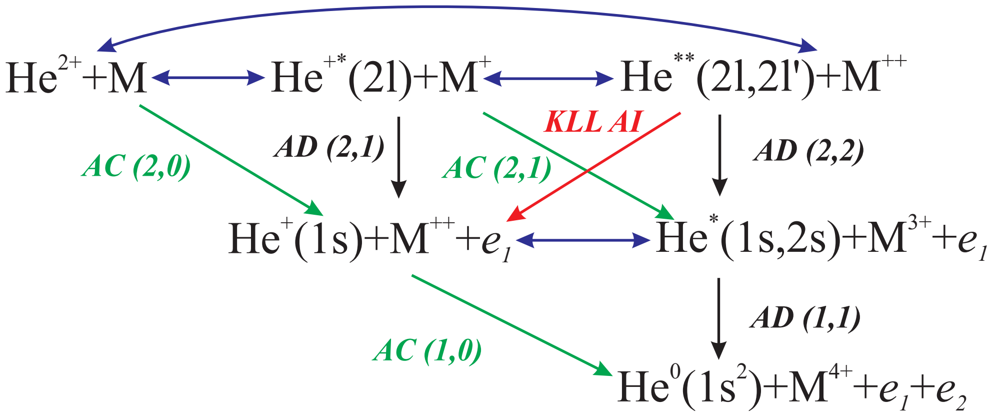
$He^{2+}$+M
$He^{+*}$(2l)+$M^+$
$He^{**}$(2l,2l')+$M^{++}$
AC (2,0)
AD (2,1)
AC (2,1)
KLL AI
AD (2,2)
$He^+$(1s)+$M^{++}$+$e_1$
$He^*$(1s,2s)+$M^{3+}$+$e_1$
AD (1,1)
AC (1,0)
$He^0$($1s^2$)+$M^{4+}$+$e_1$+$e_2$

**Figure 2.7:** Neutralization scheme of $He^{2+}$ near a metal surface (M), via resonant transitions (RT), Auger capture (AC), Auger de-excitation (AD) and KLL Autoionization (KLL AI). The numbers after transitions denote the number of holes in the ground state (n = 1) and the number of excited electrons (n = 2) of the initial transition states, respectively.

**Table 2.1:** Binding energies $E_b$ [62] of the helium atomic states involved in the neutralization processes, the He**(2l,2l') is listed in Table 2.2.

| state | $E_b$(eV) |
|---|---|
| $He^{2+}$ | 0 |
| $He^{+*}$(2s) | 13.6 |
| $He^{+}$(1s) | 54.4 |
| $He^{*}(1s,2s)^1S$ | 58.4 |
| $He^{0}(1s^2)^1S$ | 79 |

**Table 2.2:** Electronic states, binding energies $E_b$ and kinetic energies of the Auger electrons for the He**(2l,2l') states. The data are taken from the literature [63] calculated for free ions.

| state | $E_b$(eV) | $\varepsilon_k$(eV) |
|---|---|---|
| $(2s,2p)^1P$ | 18.86 | 35.5 |
| $(2p^2)^1D$ | 19.10 | 35.3 |
| $(2s,2p)^3P$ | 20.69 | 33.7 |
| $(2s^2)^1S$ | 21.17 | 32.2 |

ion, two are emitted into the vacuum. Between the states of the same row, resonant transitions can take place, → for RC, ← for RI. The transition from $He^{2+}$ to $He^{**}$ can take place via two successive single-electron RCs, or via a double-electron RC [61]. Between the states of different rows, Auger type transitions (AC, AD and KLL AI) can take place, with one Auger electron being emitted. The binding energies $E_b$ [62, 63] of the relevant helium atomic states are listed in Tables 2.1 and 2.2. For Ir(100) and O/Fe(100), the one-electron potential level for $He^{+*}(3l)$ lies above the Fermi level, therefore, the transition $He^{2+}+M \xrightarrow{RC} He^{+*}(3l)+M^{+}$ is not energetically allowed. The transition from $He^{2+}$ to $He^{+*}(2l)$ via AC, can in principle take place with one Auger electron being emitted. However, the kinetic energy of this Auger electron is quite low ($\varepsilon_k^{max} = 2.26$ eV for Ir(100), 3.8 eV for O/Fe(100)). Due to secondary electron emission at these energies, it is difficult to identify this process in the collected spectra. So this process will not be considered in this thesis. According to the literature [30], for the collisions of $He^{2+}$ with a metal surface, more than 99% of the reflected ions are found to be neutral. Therefore it is expected that, by this neutralization scheme, nearly all the emitted electrons belong to a pair. Since in this scheme, the two electrons are emitted sequentially in two successive transitions, we refer to this scheme as the sequential emission model (or sequential neutralization model).

For the He**(2l,2l') states, the electronic states, binding energies $E_b$ and kinetic energies of the Auger electrons are listed in Table 2.2. These data are taken from a theoretical calculation for the free helium atom. The relevant doubly excited states of helium are $(2s^2)$ $^1S$, (2s2p) $^3P$, $(2p^2)$ $^1D$ and (2s2p) $^1P$. Since the states $(2s^2)$ $^1S$ and (2s2p) $^3P$ as well as the $(2p^2)$ $^1D$ and (2s2p) $^1P$ are very close in energy, only two peaks from the AI process (He**(2l,2l') → $He^{+*}(2l)$) could be resolved experimentally.

Table 2.3 shows the maximum kinetic energies of the electrons emitted by the different processes, see Fig. 2.7. The primary energy $E_p$ is the energy gained by filling the

**Table 2.3:** Emission processes, neutralization energies, the maximum kinetic energies for the collision of $He^{++}$ on the Ir(100) and O/Fe(100) surface, the Auger electron energy distribution type.

| | Process | $E_p$ (eV) | $\varepsilon_k^{max}$ (eV) for Ir | $\varepsilon_k^{max}$ (eV) for O/Fe | Distribution |
|---|---|---|---|---|---|
| 1st | AC(2,0) | 54.4 | 43.06 | 44.6 | self-convolution of SDOS |
| | AD(2,1) | 40.8 | 35.13 | 35.9 | SDOS |
| | AC(2,1) | 45.6 | 34.26 | 35.8 | self-convolution of SDOS |
| | AD(2,0) | 39.2 | 33.53 | 34.3 | SDOS |
| | KLL AI | $\sim$ 34.5 | $\sim$34.5 | $\sim$34.5 | double peak $\sim$ 35 eV |
| 2nd | AC(1,0) | 24.6 | 13.26 | 14.8 | self-convolution of SDOS |
| | AD(1,1) | 20.6 | 14.93 | 15.7 | SDOS |

inner projectile atomic level. The numerical results are calculated by using Eqs. (2.9-2.11). In this case, the valence electrons are taken from the Fermi level, and the image interaction shift is not considered. As shown in table 2.3, apparently, the 1st electron has a higher maximum kinetic energy than the 2nd one. The electron pair emission prefers one fast electron with one slow electron. We emphasize, this discussion is based on the sequential model.

According to literature, the emitted electrons by the impact of $He^{2+}$ are mainly contributed from the transitions of AC(1,0), AC(2,0) and KLL AI. The transition rates of AC(1,0) and AC(2,0) are relevant to the discussion for our experimental results. In Fig. 2.8, we present the transition rates of AC(1,0) and AC(2,0) from literature. The black curves are from Ref. [30], calculated for the $He^{2+}$-Cu system, by an empirical model. The AC(1,0) rate is higher than the AC(2,0) rate. An explanation is that the transition rate is proportional to the "volume" $V$ of the atomic hole state to be filled, where $V = \frac{3}{4}\pi r_{max}$, $r_{max}$ is the radius of the hole estimated by the Slater's rules [64]. For $He^{+}$, the core is screened by a 1s electron, with the radius of the hole being $r_{max}$ = 0.59 a.u. ($V$ = 0.85 a.u.). This is larger than the $r_{max}$ for $He^{2+}$, where $r_{max}$ = 0.5 a.u. ($V$ = 0.52 a.u.). The red curves are from Ref. [65], calculated for the $He^{2+}$-jellium surface system. A so-called WKB approach is used, which assumes the transition rate is proportional to the wave function of the captured electron tunneling through the ion-surface barrier. The difference with the black curves, AC(2,0) count rate is bigger than for AC(1,0). The explanation is that, for $He^{2+}$ the ion-surface barrier felt by the metal electrons is thinner. An important agreement between the two calculations is that the transition rates at the jellium edge are in the range 0.01 a.u. $\geq 1/\tau \geq$ 0.001 a.u. (2.41 fs $\leq \tau \leq$ 24.1 fs), which is the same as the transition rates for $He^{+}$.

## 2.2 Timescales of electron excitations

The sequential neutralization model of $He^{2+}$ assumes that the whole neutralization process $He^{2+} \rightarrow He^{0}$ can be separated into two steps: $He^{2+} \rightarrow He^{+}$ and $He^{+} \rightarrow He^{0}$. The two electrons emitted in the corresponding two steps can be treated independently.

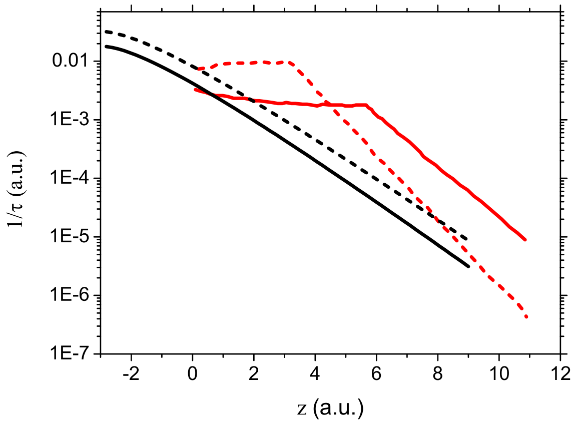

**Figure 2.8:** Auger transition rates ($1/\tau$) in a.u. as a function of the distance ($z$) from the jellium edge. The red curves are from Ref. [65], for $He^{2+}$-jellium surface, the black curves are from Ref. [30], for $He^{2+}$-Cu. The dashed curves: AC(1,0), the solid curves: AC(2,0).

Similarly, a sequential description is also used in other processes. One example is the Auger effect upon photon excitation, in which the emission of a photoelectron is followed by the emission of an Auger electron. Another example is the two-photon double ionization of He. In the corresponding sequential model, He is double ionized by two photons sequentially, He $\xrightarrow{\hbar\omega}$ $He^{+}(1s) + e_1 \xrightarrow{\hbar\omega} He^{2+} + e_2$.

For these processes, however, due to the electron-electron correlation, all the electrons involved should be treated as a whole system. This system evolves continuously in time, which can be described by the corresponding time-dependent Schrödinger equation. From this point of view, the sequential description, can only be an approximation. In some cases, the sequential description is a good approximation, and it can help us to simplify the many-particle problem. For example, if the sequential description of the Auger effect is valid, the photoelectron and Auger electron can be identified by the corresponding characteristic energies, as described in textbooks. In this case, the whole process can be studied by the conventional single electron spectroscopy, i.e. photoelectron and Auger-electron spectroscopy. If the sequential model is invalid, the two emitted electrons can only be understood by a correlated electron pair. In this case, the assignment which is photoelectron/Auger-electron will lose its meaning. The information of the correlation is only accessible by detecting the two electrons in coincidence [66–68].

We have looked through these similar sequential models. The central assumption for these sequential models is that there is a well defined intermediate state between two successive transitions. These intermediate states server to span all the excited single-electron states. However, building up of an intermediate state is not instantaneous, but requires a finite time. If the second electron is emitted after a well defined intermediate state is established, the sequential model is applicable. Otherwise the assumed intermediate state does not exist, the development of the system should be treated as a non-sequential process. Specifically speaking, consider a general picture of these sequential processes, two electrons are emitted from a N-electron system within a short time interval. After the first electron is removed, it requires a finite time to reach a stationary (N-1)-electron state. This stationary state is $He^+(1s)$ for TPDI, and a so-called one-hole state for the Auger effect. To understand how long the stationary state can be established after the first electron is removed, we have to discuss the timescales of electron excitations. For example, how long it is needed to separate the first emitted electron state and the remaining (N-1)-electron state? When the first electron is removed, the remaining (N-1)-electron system is also excited. How long it is needed for the remaining (N-1)-electron to relax to a new ground state? In the following, we will try to answer these questions. In addition, concrete examples are given to illustrate the importance of these timescales in the sequential models.

### 2.2.1 Timescale of escaping from the target

When an electron is ejected, the timescale of escaping is defined such that, the time for this electron to move far away from the ionized target, and has little influence on the residual electrons. Consider that two electrons are emitted from a N-electron system with a time interval $t_{inter}$. If when the second electron is emitted, the first electron is still in the vicinity of the ionized target, the two electrons can interact each other, leading to an energy exchange between the two electrons [40, 41]. Consider a simple case, the velocity of the first electron is constant $v_1$. When the first electron has propagated to a distance of $v_1 t_{inter}$ from the ionized target, the second electron is remove instantaneously. In a classical picture, the first outgoing electron can feel an increase of the charge of the ionized target from +1 to +2. As a consequence, the energy of the first electron is decreased by about $1/(v_1 t_{inter})$ (atomic units). In other words, because the sum energy of the two electrons is conserved, the two electrons can exchange an energy of about $1/(v_1 t_{inter})$. If we define that, when the exchange energy is smaller than a certain value $E_{ex}$, the sequential model is a good approximation, **the timescale of the electron to escape from the target can be roughly estimated by $1/(v_1 E_{ex})$ (atomic units).**

In order to illustrate the importance of this timescale in sequential models, we cite a coincidence experiment for Ar 2s photoelectron and the associated Auger electrons, from Ref. [41]. The whole process can be depicted by,

$$h\nu + Ar \rightarrow Ar^+(2l, 2l') + e_{ph} \rightarrow Ar^{2+*}(2p^{-1}3l^{-1}) + e_{A1} + e_{ph} \rightarrow Ar^{3+}(3p^{-3}) + e_{A1} + e_{A2} + e_{ph}.$$

It should be noticed that, the first Auger electron ($e_{A1}$) is released from a Coster-Kronig decay, the associated Ar 2s hole lifetime is very short (~ 290 as). According to the timescale we just proposed, a short time interval indicates a strong interaction between the photoelectron and the first Auger electron ($e_{A1}$). The first released Auger electron ($e_{A1}$) is in the 20-50 eV range, while the second Auger ($e_{A2}$) is ~ 190 eV.

Fig. 2.9 shows the coincidence between the Ar 2s photoelectron (y axis) and the first released Auger electron ($e_{A1}$). The interesting observation is the diagonal lines. The diagonal lines correspond to different intermediate $Ar^{2+*}(2p^{-1}3l^{-1})$ states, for example, A: $2p^{-1}3p^{-1}(^3D_3)$, B: $2p^{-1}3p^{-1}(^1S_0)$, C: $2p^{-1}3s^{-1}(^1P_1)$. The diagonal lines indicate the photoelectron and the first Auger electron can share the available sum energy. It can be noticed that the energy of Ar 2s photoelectron (red line at 11.5 eV) is shifted from the normal position (black line at 12.5 eV). This energy shift (1 eV) is smaller than the

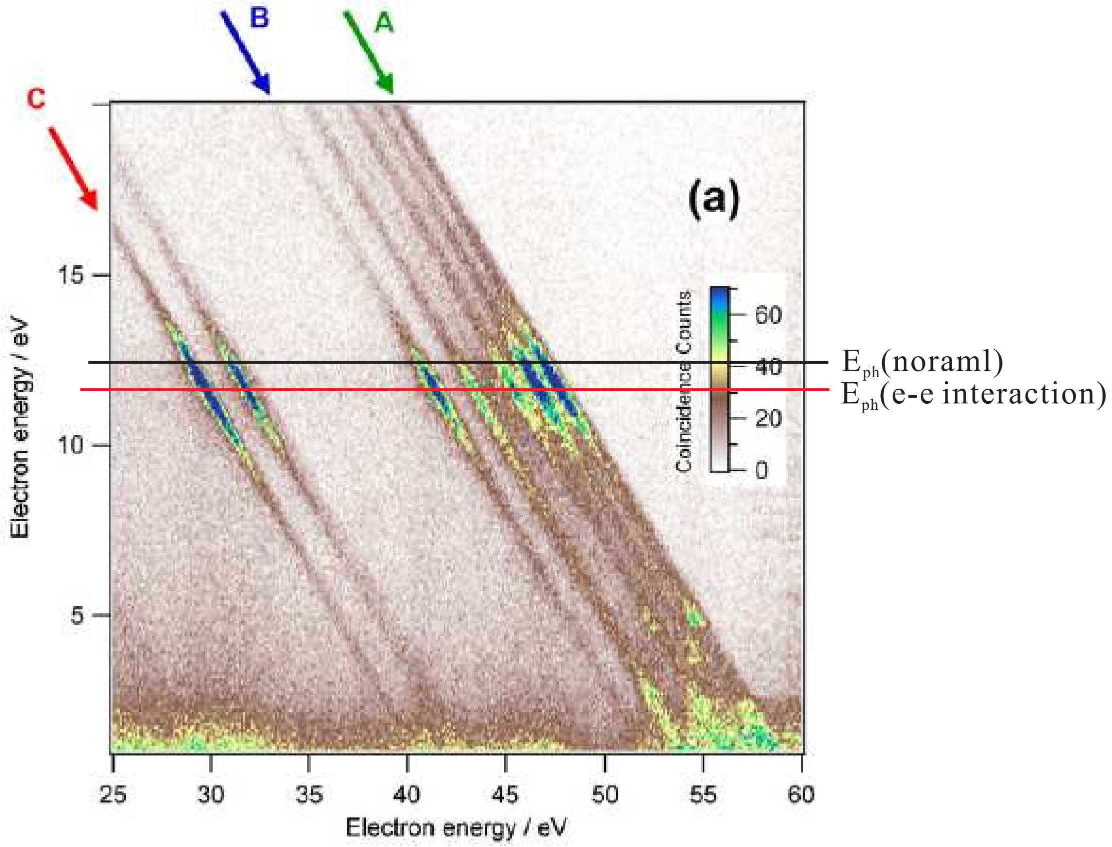

**Figure 2.9:** 2D-energy spectrum for the 2s photoelectron (y axis) and the first emitted Auger electron (x axis), from Ref. [41]. The Diagonal lines correspond to different intermediate $Ar^{2+}$ states. The black line labels the normal 2s photoelectron energy, the red line labels the photoelectron energy in this experiment, distorted by the interaction between the two electrons.

prediction of the above timescale, $1/(v_1 t) = 2$ eV. This is because the velocity of the first Auger electron and the second Auger electron have influence. This has been can be well described in Ref. [41]. This experiment shows that, the interaction of the two electrons in the continuum can lead to an energy sharing between the two successively emitted electrons, in which the sequential description is inappropriate.

### 2.2.2 Timescale of screening

When an electron is removed instantaneously from a surface, a hole with a positive charge is left. The existence of a bare hole alters the potential seen by the surrounding electrons. They will try to screen this positive charge, in order to reduce the system energy. This process is called screening. The stationary state after the screening is called one-hole state. **The timescale of screening is of the order of the inverse plasmon frequency.**

The timescale of screening has been directly measured by Huber *et al* [69], by a so-called pump-probe technique. First, a GaAS sample is excited with a 10-fs laser at 800 nm (visible range). The first pulse severs to create randomly distributed electrons and holes. The second pulse (THz range), with a delay time $t_D$, is used to measure the complex dielectric function. The complex dielectric function describes how the particles act to screen the interparticles Coulomb interaction. By varying the $t_D$ values, a picture how the dielectric function changes over a very short time is built up, shown in Fig. 2.10. Between $t_D = 0$ and 25 fs, the variation of the imaginary part and the real part is little. This indicates, at $t_D = 25$ fs the particles still interact with each other via bare Coulomb interaction. A resonant structure at 14.4 THz, which is due to emerging plasmons, becomes narrow quickly as the delay time between pulses increases from 25 to 100 fs. This is comparable to the inverse of plasmon frequency, which is about 70 fs in this case. In other words, this experiment shows directly the development from the bare Coulomb interaction to its fully screened form requires a time of roughly the inverse plasmon frequency. A theoretical demonstration of this timescale can be found in the Ref. [70].

To illustrate the importance of the screening timescale, we cite our previous study of DPE on clean Cu(100) [44] and S overlayers on Cu(100) (S/Cu(100)) [71]. For clean Cu(100), the electron pairs are excited by primary photons with energy 125 eV. The main experiment result is a 2D-energy spectrum for the two coincidence electrons, which is presented in Fig. 2.11(a). In the 2D spectrum, two high intense regions ($E_1$, $E_2$)=(56 eV, 46 eV) and (46 eV, 56 eV) can be observed, which are labeled by A and B. According to the binding energies of Cu, they can be explained by a photo-Auger electron pair, with photoelectron ($3p_{1/2}$ and $3p_{3/2}$) $\sim$ 46 eV and Auger electron ($M_{2,3}$-$M_{45}M_{45}$) $\sim$ 56 eV. The striking observation is the diagonal line connecting these two regions. The appearance of this diagonal line indicates that the two electrons conserve the energy available to them, and they share the energy continuously. In other words, the photoelectron and Auger electron can have equal energy at the center of this line, therefore, it is impossible and meaningless to distinguish them as Auger electron or photoelectron. The intensity along this line must be understood by a non-sequential process.

For S/Cu(100), the electron pairs are excited by 301 eV photons. The corresponding

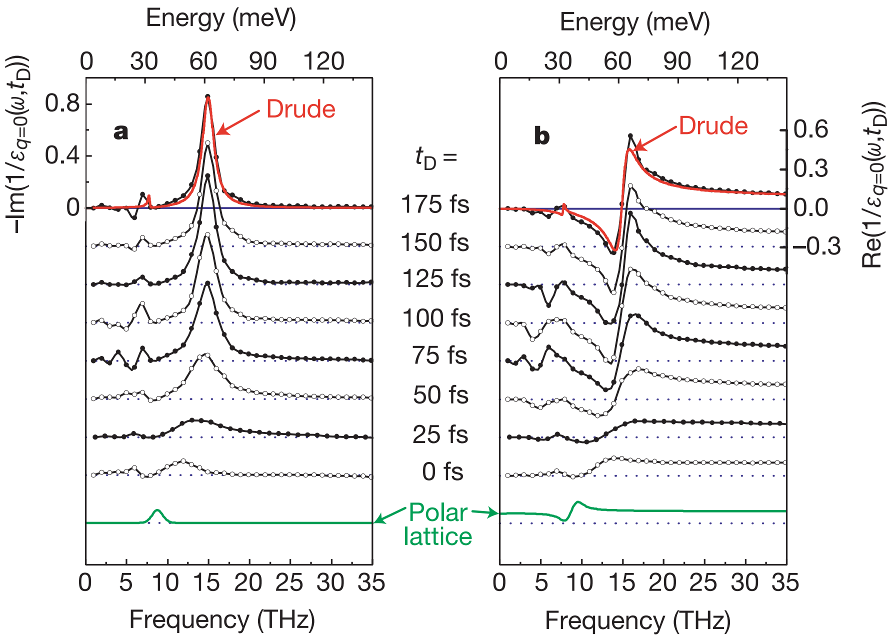

**Figure 2.10:** Complex dielectric function of GaAs for different pump-probe delay values $t_D$, (a):imaginary part, (b): real part.

2D-energy spectrum is presented in Fig. 2.11(b). In the 2D-energy spectrum, two vertical and two horizontal lines with high intensity can be observed, which are situated at $E_1$=134 eV, 135 eV and $E_2$=134 eV, 135 eV, respectively. These energies correspond to the S 3p$_{1/2}$ and 3p$_{3/2}$ photoelectrons. The energy along these lines correspond to the S L$_{2,3}$VV Auger electrons. The two vertical (or horizontal) double lines are parallel to the x-axis (or y-axis) within the energy window, which implies the energies of the photoelectrons do not change with the variation of Auger electrons kinetic energies. The above observations indicate there is not a clear relationship between photoelectron and Auger electron in energy. The the sequential model is applicable for S L$_{2,3}$VV of S/Cu(100).

A clear difference between the two Auger processes is the Auger transition rate. In this case of Cu(100), the Auger decay M$_{2,3}$-M$_{45}$M$_{45}$ belongs to the so-called super coster-kronig (SCK) transition, where the three electron involved are from the same atomic shell ($n$ = 3). The timescale of this Auger decay is about 0.4 fs [72]. While the S L$_{2,3}$VV Auger decay is a slow process, about 4 fs [73]. The screening time of the core-hole in surface can be roughly estimated by $t_sc = 1/\omega_{sp}$ [74], where $\omega_{sp}$ is the surface plasmon frequency. The surface plasmon for Cu(100) is about $\hbar\omega_{sp} = 2.2$ eV [75], corresponding to the time $1/\omega_{sp} = 0.3$ fs. We assume the surface plasmon of S/Cu(100) is very close to that of Cu(100). The timescale of the Cu M$_{2,3}$-M$_{45}$M$_{45}$ Auger decay is comparable to the screening process, while the S L$_{2,3}$VV Auger decay is much longer than it. In this case of Cu(100), the screening process is involved in the Auger decay, the Auger spectrum should be hence described by a one-step approach [76].

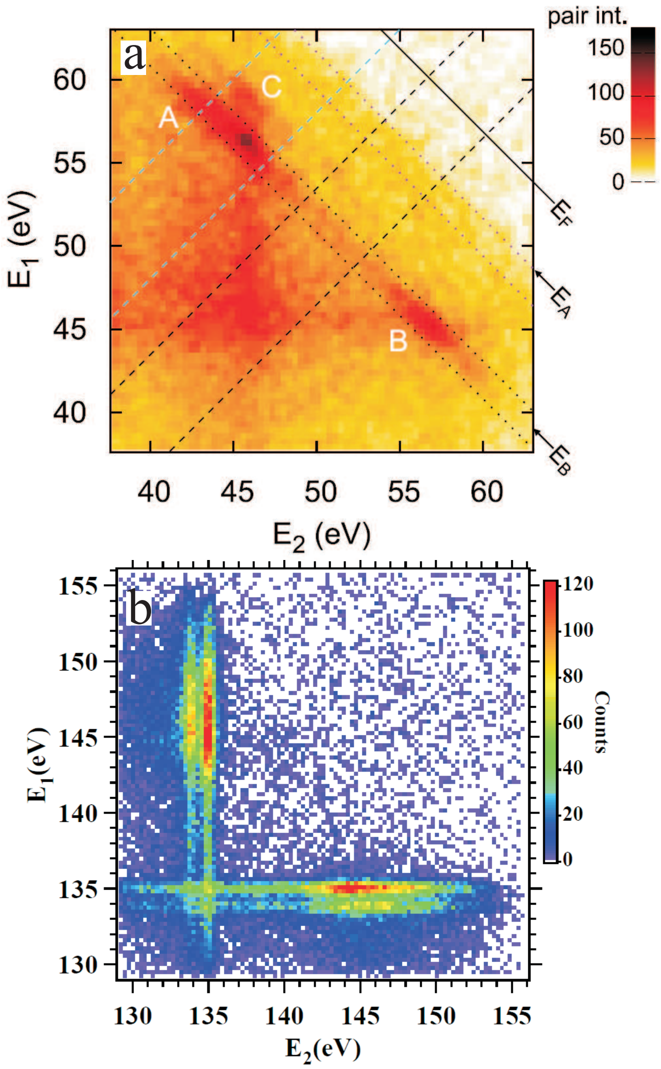

**Figure 2.11:** 2D-energy spectrum for the electron pairs emission, (a) from clean Cu(001) surface by 125 eV photons [44], (b) from S overlayer on Cu(100) by 301 eV photons [71].

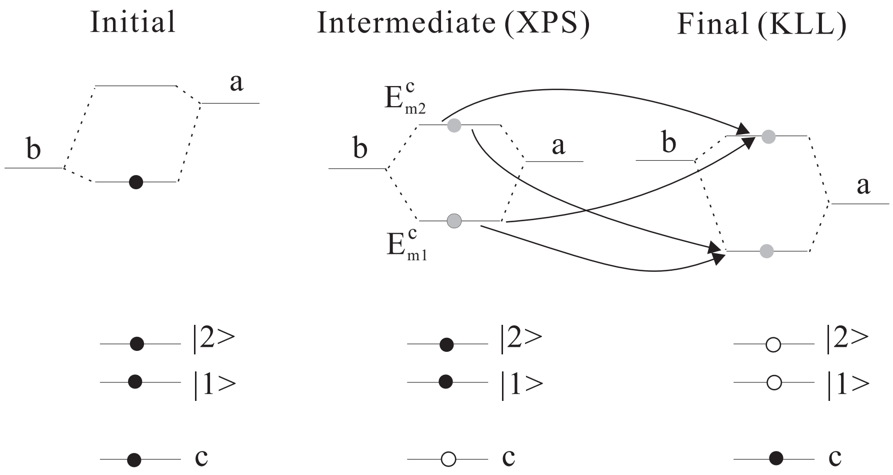

**Figure 2.12:** Schematic view of the two-level model for the Auger process of a surface with a di-molecule absorbed on it, from Ref. [76, 77]. From left to right, we present the zero (initial), one (XPS), and two (KLL) core hole states. The upper lines represent the molecular levels, the lower lines represent the solid levels. There are four paths, corresponding to the combinations of the two XPS states and two KLL states.

### 2.2.3 Timescale of quantum interference between different paths

We first recall the interference effect in real space, for example, low-energy electron diffraction (LEED) experiment. In LEED, the interference effect of the electron beam due to the diffraction on a surface, requires that the wave length of the electrons is comparable to the lattice constant. For the propagation of a wave function in a sequential process, if there are two intermediate states, there will be two different evolution paths correspondingly. If the energy broadening due to the finite lifetime of an intermediate state is larger or comparable to the energy separation between the two intermediate states, the difference transition path, i.e. via different intermediate states, will interfere with each other in wave function space. **The timescale of the quantum interference is about $\hbar/\Delta E$, where $\Delta E$ is the energy separation between the intermediate states.**

To illustrate the importance of this timescale, we cite a theoretical calculation for Auger decay, by Gunnarsson and Schönhammer [76]. This calculation concerns the Auger spectrum of a surface, with di-molecules adsorbed on it. Fig. 2.12 shows the corresponding energy levels. There is only one valence electron in the molecular. In the initial state, this electron is in the lowest molecular level. In the intermediate (final) state, it has two options: excited or ground states. Therefore, there are four different paths for the Auger decay. The simulated Auger spectra are shown in Fig. 2.13. The Auger spectrum is separated into two terms: direct term (solid line) and interference term (dashed line). $\Gamma_{KLL}$ is the lifetime broadening due to the KLL Auger decay.

For small $\Gamma_{KLL}$ values, the direct term dominates the Auger spectrum. If $\Gamma_{KLL}$ is large compared to $|E^c_{m_2} - E^c_{m_1}|$, the interference term becomes important. The upper and lower panels show, respectively, the calculated Auger spectrum for $\Gamma_{KLL} = 0.5$ eV and $\Gamma_{KLL} = 2$ eV, with a given parameter $|E^c_{m_2} - E^c_{m_1}| = 3$ eV. In the upper panel, the spectrum consists of four peaks, corresponding to the four different combinations

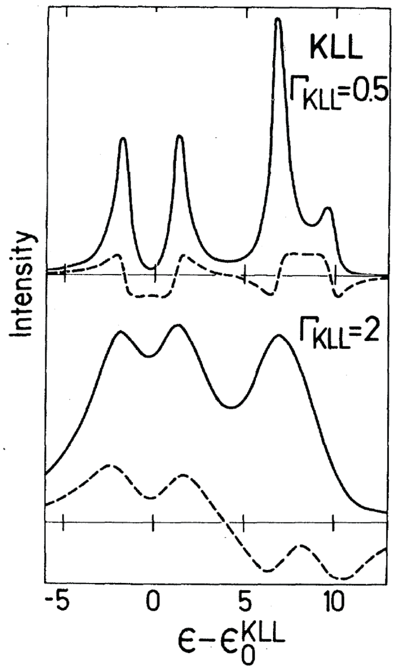

**Figure 2.13:** Simulated Auger spectrum for the two-level model for two lifetime broadening values ($\Gamma_{KLL}$), from Ref. [76]. The corresponding Auger process is depicted in Fig. 2.12. The solid curve represents the total spectrum and the dashed curve represents the interference contribution. The insert shows the center gravity of the spectrum as a function of $\Gamma_{KLL}$. All energies are given in eV.

of XPS and final states. In the upper panel, the interference contribution is small. By contrast, in lower panel, the interference contribution becomes larger, and the boundary of the peaks becomes obscure. In this case, it is more difficult to determine from which intermediate states the Auger decay starts. In this case, the intermediate states are not well defined, thereby the sequential description is inappropriate.

For a sequential neutralization scheme of MCI, like Fig. 2.7, there are usually several neutralization paths (via different intermediate states) competing with each other. Therefore, if the lifetime of the intermediate states are not long enough, the quantum interference effect will be active.

### 2.2.4 Timescale of electron capture in ion neutralization

We discuss an important timescale for the ion neutralization process, the time it takes for an electron to travel from the topmost layer to the ion in front of the surface. The relevant geometry is depicted in Fig. 2.14. At time $t = 0$, the electron is staying in the topmost layer. The velocity of a valence electron in surface is in the range, $0 \leq v(r_{t=0})$ $\leq v_{fe}$, where $v_{fe}$ is the Fermi velocity. A typical value for the Fermi velocity of a metal surface is about 0.5 a.u. (10.9 Å/fs) [78]. We consider a $He^{2+}$ is located at the most likely position for AC(2,0), $z = 1.3$ a.u.. for Ir(100), and 1.9 a.u. for O/Fe(100). Then, the travel time is, $t_{tra} \geq 6.6$ a.u. (0.16 fs) and 9.8 a.u. (0.24 fs).

This timescale is important, because in the sequential description, the ion captures

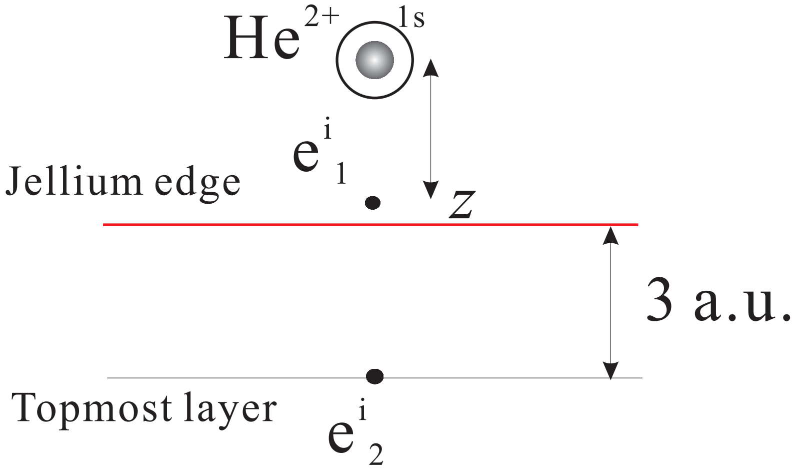

**Figure 2.14:** sketch for a $He^{2+}$ captures two valence electrons.

the second electron after the first electron has arrived at the ion. Otherwise, when the second capture occurs, the first electron is still in the path, since the path is short about 4-5 a.u., the interaction, for example Coulomb interaction, between the two electrons is non-negligible. Therefore, the two electrons are correlated, the sequential description is inappropriate.

# Chapter 3

# Experimental Techniques

## 3.1 Principle of the two-electron coincidence experiment

In the two-electron coincidence experiments, we want to study the 2D-energy distribution of the two emitted electrons, like the one shown in Fig. 2.11. The detection of an electron pair obviously requires two electron detectors. In addition, an electronic circuit is needed, which can impose a temporal constraint of the two detection signals. In other words, a valid pair emission is defined when the arrival time difference of the two electrons is less than a threshold value (200 ns in our case). An important issue should be noticed, the detected two electrons can be from one collision event ("true" coincidence), but also can be from two different collision events ("random" coincidence). Hence, in our dataset, we have the contributions from both the "true" coincidences and the "random" coincidences. As only the "true" coincidences are what we are interested, we naturally aim for a high true/random ratio. Therefore, how to estimate and increase the true/random ratio is important for the two-electron coincidence experiments.

### 3.1.1 Arrival time difference

In a coincidence experiment, one important parameter for an electron pair is the arrival time difference at the two detectors. The way how to measure it will be described in Sec. 3.2.3. The distribution of the arrival time differences, referred to as time histogram, is exemplified in Fig. 3.1. The main feature is a peak positioned on a constant background (shaded area). As just mentioned, the detected electron pairs have the contributions both from the "true" coincidences and the "random" coincidences. An assumption is that, without any time relations the time intervals of the "random" coincidences distribute homogeneously. By contrast, the time intervals of the "true" coincidences only distribute in a narrow range. Therefore, the emergence of the peak is due to "true" coincidences, while the constant background is due to "random" coincidences. The width of the peak reflects the time resolution of the instrument.

It is obvious that we only want to select the events under the peak for further analysis. Hence, we define a time window centered at the peak, and the width of the time window is chosen such that it can cover almost all the "true" coincidences. In

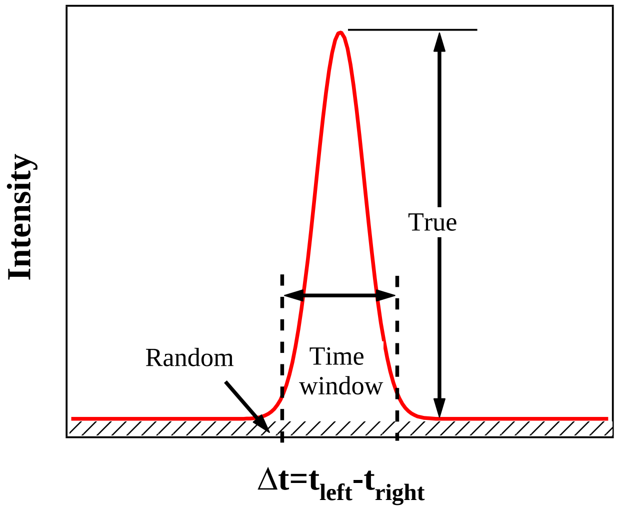

**Figure 3.1:** The time difference histogram: Events versus arrival time differences (Δt). The background (shaded area) is due to "random" coincidences, and the peak above the background is due to "true" coincidences. A time window is defined by two vertical dashed black lines, within which the events are selected for further analysis.

the context of this thesis, we chose the width to be 1.9×full width at half maximum (FWHM) of the peak, indicated by the dashed lines in Fig. 3.1. The reason is that if we assume a Gaussian distribution for the time histogram for the "true" coincidence, in this case, the window will cover 90% of the "true" coincidences. For the selected events, the true/random ratio can be determined by comparing the areas above and below the baseline.

### 3.1.2 The determining factors for the true/random ratio

We want to emphasize that it is impossible to separate the "true" coincidences and the "random" coincidences. Once a "random" coincidence is taken, it can never be removed from the dataset. Hence, a "good" true/random ratio (higher than 1:1) is required. Here, we want to discuss the key factors that can influence the true/random ratio.

Consider a coincidence experiment with a time window $t_w$ (defined the same way as for Fig. 3.1) and a low primary flux $I$, $I \cdot t_w \ll 1$. In our experiments, a typical value is of the order of $I \sim 2 \times 10^6$ primary ions/s, $t_w \sim 20$ ns, and $I \cdot t_w = 0.04$. The "true" ("random") coincidences are due to one (two) primary particle accidentally distributed within the time window $t_w$. Then, the "true" and "random" coincidence count rate has the relation, respectively,

$$r_t \propto \frac{P(1)}{t_w}, \tag{3.1}$$

$$r_r \propto \frac{P(2)}{t_w}, \tag{3.2}$$

where $P(n)$ is defined as the probability to find $n$ primary particles within $t_w$. We assume that the primary particles are randomly distributed in time, and then $P(n)$ can be described by the Poisson statistics,

$$P(n) = \frac{\lambda^n \cdot e^{-\lambda}}{n!}, \tag{3.3}$$

where $\lambda$ is defined as $\lambda = I \cdot t_w$. Therefore, we obtain

$$\begin{aligned} P(1) &= I \cdot t_w \cdot e^{-I \cdot t_w}, & (3.4) \\ P(2) &= \frac{(I \cdot t_w)^2 \cdot e^{-I \cdot t_w}}{2}. & (3.5) \end{aligned}$$

Since $I \cdot t_w \ll 1$, we can use the approximation $e^{-t_w \cdot I} \approx 1$, and we can simplify,

$$\begin{aligned} P(1) &= I \cdot t_w, & (3.6) \\ P(2) &= \frac{(I \cdot t_w)^2}{2}. & (3.7) \end{aligned}$$

The "true" and"random" coincidence count rate is,

$$\begin{aligned} r_t &\propto \frac{P(1)}{t_w} \propto I, & (3.8) \\ r_r &\propto \frac{P(2)}{t_w} \propto \frac{I^2 \cdot t_w}{2}. & (3.9) \end{aligned}$$

Then, we have the true/random ratio,

$$\frac{r_t}{r_r} \propto \frac{1}{I \cdot t_w}. \tag{3.10}$$

There are two ways to increase the true/random ratio, reduce the primary flux and improve the time resolution. The time resolution is determined by the instrument, see Sec. 3.2.1. Then, for a given instrument, the only option is to reduce the primary flux. However, as a consequence, the coincidence count rate is low. In the context of this thesis, the typical coincidence count rate is 1 - 10 counts/s, while the true/random coincidence ratios were better than 2.

## 3.2 Coincidence spectrometer

Basically, there are two available techniques for pair emission spectroscopy: time dispersive (time-of-flight) spectrometer [8] and energy dispersive spectrometer [6]. The time-of-flight spectrometer measures the time for an electron to travel through a particular distance in order to obtain the kinetic energy. The advantages of this technique are large acceptance angle and high transmission, whereas the drawbacks are, first, it needs a short pulsed source as the reference start time; second, the energy resolution is poorer for higher kinetic energy electrons. For the energy dispersive spectrometer, for example the concentric hemispherical analyzer (CHA), the kinetic energy is deduced

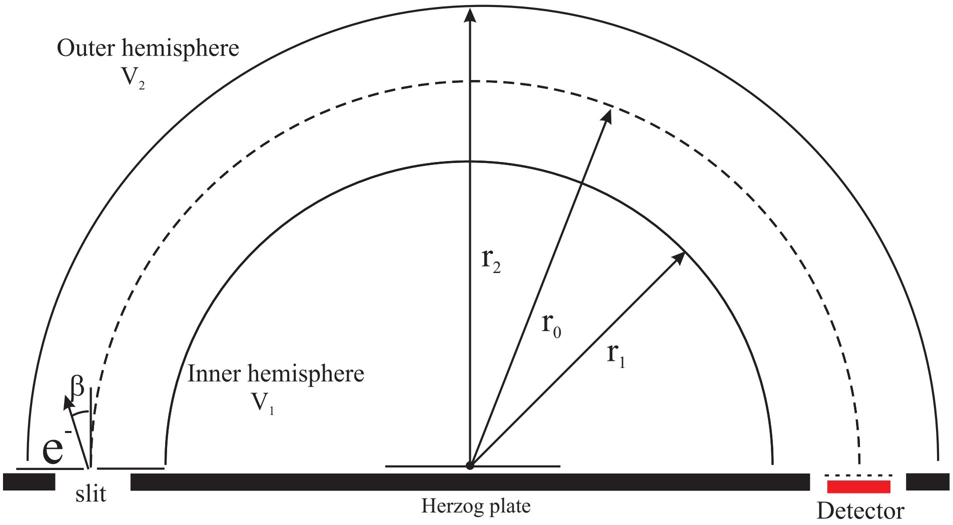

**Figure 3.2:** Schematic cross section of a CHA without transfer lens. Two hemispheres of radii $r_1$ (inner) and $r_2$ (outer) are concentrically positioned, with electric potential $V_2$ and $V_1$ respectively. The semicircle (dashed line) of radius $r_0=\frac{1}{2}(r_1+r_2)$ represents the orbit of electrons entering the slit normally, with initial radius $r_{in}=r_0$, kinetic energy $E=eV_0$, where $V_0$ is the pass energy.

from the impact position on the detector. The advantages are that it does not need a pulsed source and the energy resolution (can be adjusted by the entrance slit) is constant for all kinetic energies, whereas the drawback is the small solid angle.

A pulsed ion source is unavailable, therefore we employ two energy dispersive spectrometers to measure the kinetic energies of the two emitted electrons. The kinetic energy of the electrons is measured over a range of 5 - 40 eV, with a constant energy resolution of 0.7 eV.

We use two spectrometers were bought from VG Scienta, model R4000. Each spectrometer is composed of a CHA with a mean radius of 200 mm, a transfer lens with an acceptance angle of ±15° and an electron detector. Instead of scanning the energy, we want to measure the kinetic energies of the two electrons in parallel. The kinetic energy is deduced from the electron impact position on the detector. The original detector consists of a channel plate and a phosphorous screen imaged by a charge-coupled device (CCD) camera. This does not allow for single-electron detection of the impact position. Consequently, we replaced the original detectors by the installation of microchannel plates (MCP) with a 40-mm diameter active area and a resistive anode (Sec. 3.2.2).

### 3.2.1 Principle of the concentric hemispherical analyzer

Fig. 3.2 shows the schematic cross section of a CHA. Two hemispheres of radii $r_1$ (inner) and $r_2$ (outer) are concentrically positioned, with electric potential $V_1$ and $V_2$, respectively. Here we consider an ideal situation, which neglects the fringing field effect near the entrance and exist of the hemisphere. In other words, we assume a spherical 1/r potential. Let an electron enter the CHA through the slit, with initial radius $r_{in}$, kinetic energy $E = eV$ and angle $\beta$ respect to the normal. The trajectory of this electron $r(\theta)$ can be described by [79],

$$y(\theta) = -y_0 \cdot tan\beta \cdot sin\theta + (y_0 - c^2)cos\theta + c^2, \tag{3.11}$$

where

$$y(\theta) = \frac{r_0}{r(\theta)}, \quad y_0 = \frac{r_0}{r_{in}}, \tag{3.12}$$

$$c^2(V) = \frac{V_0 y_0^2}{V cos^2\beta - 2V_0(1 - y_0)}, \tag{3.13}$$

and

$$V_0(\frac{r_2}{r_1} - \frac{r_1}{r_2}) = (V_1 - V_2), \tag{3.14}$$

where $eV_0$ is the pass energy. When the electrons enter the slit with kinetic energy $eV_0$, initial radius $r_{in} = r_0$ and angle $\beta = 0$, then

$$r(\theta) = r_0. \tag{3.15}$$

The corresponding orbit is a semicircle with radius $r_0 = \frac{1}{2}(r_1 + r_2)$, as the dashed line shown in Fig. 3.2.

The final radius $r_{out}$, when $\theta = 180^o$ can be deduced from equation (3.11),

$$r_{out}(V) = \frac{r_0}{2c^2(V) - y_0}. \tag{3.16}$$

If V $\approx V_0$, we can expand $r_{out}(V)$ by a Taylor series. If we use the linear term only, we obtain,

$$r_{out} = r_0 + \left.\frac{\partial r_{out}}{\partial V}\right|_{\beta=0; r_{in}=r_0} (V - V_0) = 2\frac{V}{V_0} r_0 - r_0. \tag{3.17}$$

The relationship between the electron kinetic energy and the impact position $R = r_{out} - r_0$ can be described by a linear function,

$$E = eV = eV_0 + \frac{eV_0}{2r_0} R. \tag{3.18}$$

For our spectrometer, the mean radius of the CHA is $r_0 = 200$ mm, the diameter of the active area of detector is 40 mm. From equation 3.17 the energy interval for our spectrometer is supposed to be 10% of the pass energy. However, the experimental observation is 9%. The difference arise from the fringing effect. In other words, the spherical 1/r potential considered here is just an approximation.

It has to be noticed that the kinetic energy $E$ of the electron is with respect to the Herzog plate. At the Herzog plate, a voltage of $E_k$ - e$V_0$ is applied with respect to the ground. In this case, the kinetic energy of the electron with respect to the ground is,

$$E_{ground} = E_k + W_{sp} + \frac{eV_0}{2r_0} R, \tag{3.19}$$

where $W_{sp}$ is the work function of the spectrometer. While the kinetic energy with respect to the sample is,

$$E_{sample} = E_k + W_{sp} - W_{sa} + \frac{eV_0}{2r_0}R, \tag{3.20}$$

where $W_{sa}$ is the work function of the sample. We refer to $E_k$ as the mean energy of the spectrometer. If we want to move the energy window, we can just tune the value of $E_k$.

As explained in Sec 3.1.2, the time resolution is important for a coincidence experiment. A good time resolution or a narrow time dispersion can help to increase the true/accidental ratio. Here we discuss the time resolution for a CHA. As the Coulomb force applied on an electron inside the hemisphere points to the center, see Fig. 3.2, in a polar coordinates centered at the center the angular momentum is conserved,

$$J = mr^2\frac{d\theta}{dt}. \tag{3.21}$$

Then the time for the electron to pass through the hemisphere is,

$$T = \int \mathrm{d}t = \frac{m}{J}\int_0^\pi r^2(\theta)\,\mathrm{d}\theta = \frac{A\sqrt{2m/e}}{[Vcos^2\beta - 2V_0(1-y_0)]^{1/2}r_{in}}, \tag{3.22}$$

where $A = \frac{1}{2}\int_0^\pi r^2(\theta)d\theta$. According to a standard ellipse equation,

$$r(\theta)[1 + \varepsilon cos(\theta - \theta_0)] = l, \tag{3.23}$$

where $\epsilon$ and $l$ are the eccentricity and scale of the ellipse, and $A$ is given by,

$$A = \frac{l^2}{2(1-l^2)}[\frac{2}{\sqrt{1-\varepsilon^2}} \times tan^{-1}(\frac{\sqrt{1-\varepsilon^2}}{\varepsilon \cdot sin\theta_0}) - \frac{2\varepsilon sin\theta_0}{1-\varepsilon^2 cos^2\theta_0}]. \tag{3.24}$$

From Eq. 3.22, there are three parameters of a CHA can contribute to the time dispersion. They are the energy interval $V$, entrance angle $\beta$, and entrance slit $r_{in}$. For simplicity, we want to discuss the three contributions, separately.

From Eqs. 3.11- 3.24, with only the first order being considered, we have the relations,

$$\begin{aligned} \Delta T_V &= \left.\frac{\partial T}{\partial V}\right|_{V=V_0,\beta=0,r_{in}=r_0} \cdot \Delta V \\ &= \frac{3}{4}\sqrt{\frac{2m}{e}}r_0\pi V_0^{-3/2} \cdot \Delta V. \end{aligned} \tag{3.25}$$

$$\begin{aligned} \Delta T_\beta &= \left.\frac{\partial T}{\partial \beta}\right|_{V=V_0,\beta=0,r_{in}=r_0} \cdot \Delta\beta \\ &= 2\sqrt{\frac{2m}{e}}r_0 V_0^{-1/2} \cdot \Delta\beta \end{aligned} \tag{3.26}$$

$$\begin{aligned}\Delta T_{r_{in}} &= \left.\frac{\partial T}{\partial r_{in}}\right|_{V=V_0,\beta=0,r_{in}=r_0} \cdot \Delta r_{in} \\ &= 0. \end{aligned} \tag{3.27}$$

From Eqs. 3.24-3.27, we can get some relations for the time dispersion in the hemisphere,

(i) As $\Delta T_{r_{in}} = 0$, the entrance slit has no influence on the time dispersion. The main contributions are from the energy dispersion and the entrance angle dispersion.

(ii) The time dispersion increases linearly with the mean radius of the CHA.

(iii) The time dispersion increases linearly with $V_0^{-1/2}$ (for Eq. 3.25, in our case, ΔV = 9% × $V_0$).

In this work $V_0$ = 300 V, hence the energy interval is eΔV = 27 eV. For a 1 mm entrance slit, the acceptance angle is $\Delta\ \beta = 6.1^o$ $(-3.05^o \leq \beta \leq 3.05^o)$, and we obtain $\Delta T_\beta = 8$ ns, and $\Delta T_V = 8$ ns. If these contributions are Gaussian distributed,

$$\Delta T = \sqrt{\Delta T_V^2 + \Delta T_\beta^2} = 11.3 \text{ ns.} \tag{3.28}$$

In a coincidence experiment with two spectrometers, the time resolution becomes,

$$\Delta T_c = \sqrt{\Delta T^2 + \Delta T^2} = 16 \text{ ns.} \tag{3.29}$$

The experimental observation is 17 ns, which is about 1 ns longer than the calculation. That is because, for the time resolution of the whole system, besides the contribution from hemisphere, the lens and electronics (∼ 0.7 ns) can also contribute. However, our calculation is very close to the experimental observation. We conclude that the main contribution of the time dispersion arises from the electron motion within the two hemispheres. This is consistent with the observation in literature [80], which was using a CHA also from VG Scienta.

### 3.2.2 Detection system

Fig. 3.3 shows the schematic view of the detector bought from Quantar Technology Incorporated, Model 3300 SERIES. After passing through the Grid, which has the same electric potential as the Herzog plate, the incidence electrons strike the front surface of the first MCP, resulting in secondary electrons emission from the wall of one or more microchannels. Accelerated by the electric field, these secondary electrons strike the adjacent channel wall, creating an electron avalanche. After passing through two MCPs successively, a single electron charge is amplified by $5\times10^6$ [81], resulting a charge cloud, which travels in a uniform electric field and is deposited on the resistive anode. The charge cloud diffuses on the uniform sheet surface of the resistive anode towards the collection electrodes located on the periphery of anode. The four charge pulses are converted into high level shaped bipolar pulse by charge-sensitive/shaper amplifiers and then read by the position computer, which outputs the position signal “X, Y”. The relationship between the four charge pulses (A,B,C,D) and electron impact position (X, Y) can be described by,

$$X = \frac{B+C}{A+B+C+D}, \tag{3.30}$$

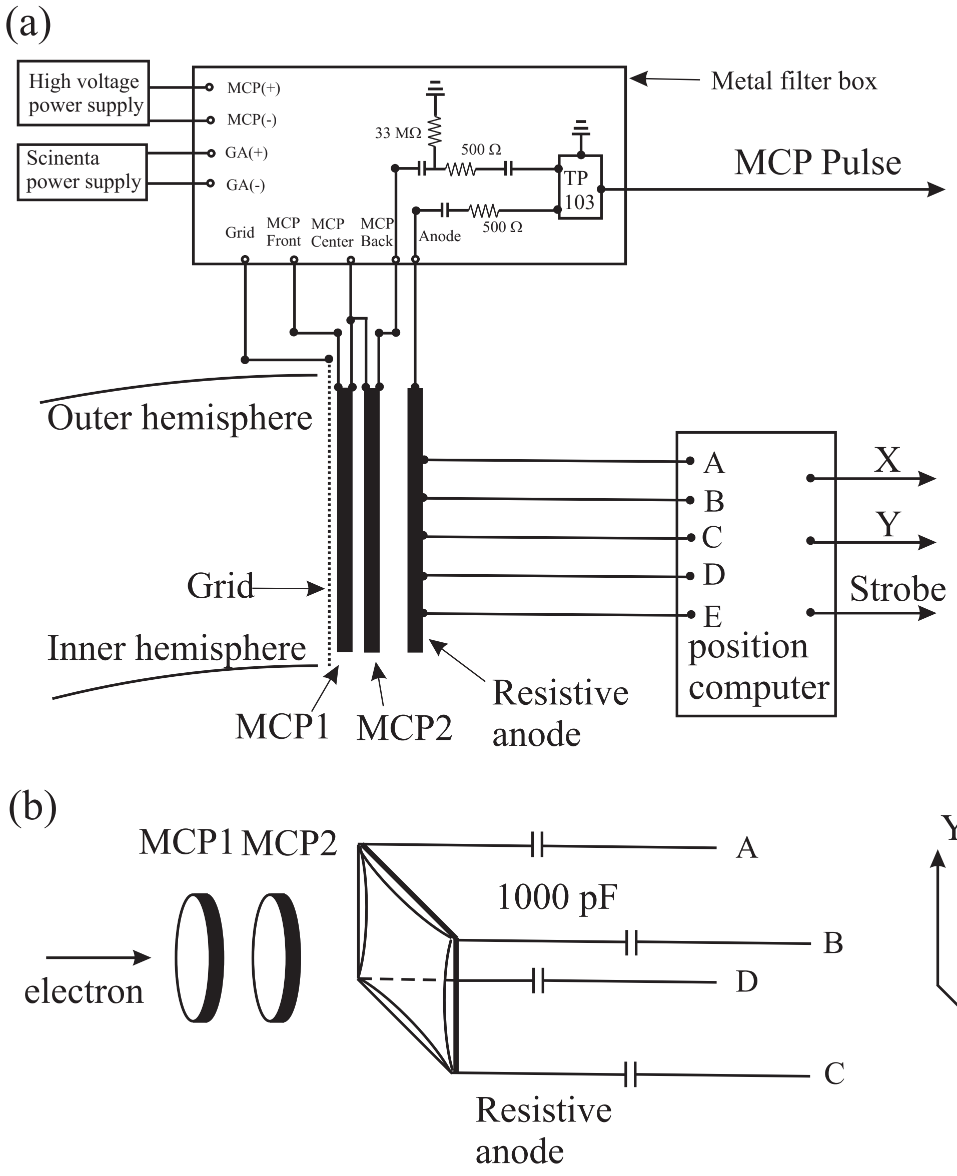
(a)
High voltage power supply
Scienta power supply
MCP(+)
MCP(-)
GA(+)
GA(-)
33 MΩ
500 Ω
500 Ω
TP 103
Grid
MCP Front
MCP Center
MCP Back
Anode
Metal filter box
MCP Pulse
Outer hemisphere
Grid
Inner hemisphere
MCP1
MCP2
Resistive anode
A
B
C
D
E
position computer
X
Y
Strobe
(b)
MCP1 MCP2
electron
1000 pF
A
B
D
C
Resistive anode
Y
X

**Figure 3.3:** (a) Schematic view of the detector. (b) Schematic view of the microchannel plate and resistive anode.

and

$$Y = \frac{A + D}{A + B + C + D}, \tag{3.31}$$

where X, and Y are the coordinates of the impact position as shown in Fig. 3.3(b).

The abrupt change of the potential between the second MCP and the resistive anode can generate a short pulse. After passing through a filter box (extraction, inversion and amplification), this pulse, referred to as the MCP pulse, will be used as the fast "timing" signal. The MCP pulse and "X, Y" signals will be further processed in the coincidence and data acquisition electronics (Sec. 3.2.3).

The voltages of the grid, MCP and resistive anode are provided by a High Voltage power supply and a Scienta power supply through a filter box, whose electric circuit is described in more details in the appendix. The function of the filter box is to distribute the voltage between grid, MCP and resistive anode, avoid ground loops and reduce the noise.

### 3.2.3 Data acquisition electronics

The measurements of the employed instrument are the impact positions on the MCP (this provides the kinetic energies) and two time signals, which are used to determine the arrival time difference. This information can be taken from the "X, Y" signals and the "MCP pulse" output from the two detectors (see Sec. 3.2.2). The information acquisition and processing will be introduced in following.

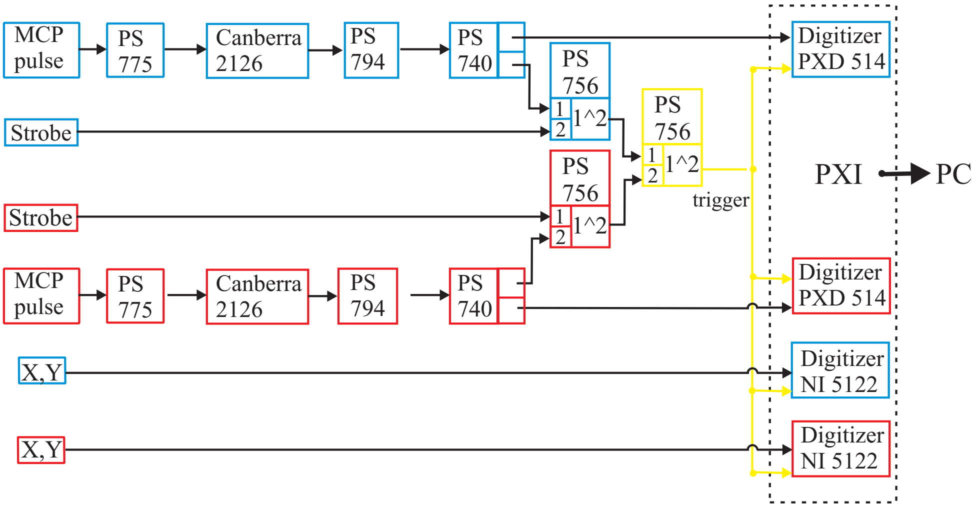
MCP pulse
PS 775
Canberra 2126
PS 794
PS 740
PS 756
1
2
1^2
Strobe
PS 756
1
2
1^2
trigger
Strobe
PS 756
1
2
1^2
MCP pulse
PS 775
Canberra 2126
PS 794
PS 740
X,Y
X,Y
Digitizer PXD 514
PXI
PC
Digitizer PXD 514
Digitizer NI 5122
Digitizer NI 5122

**Figure 3.4:** Schematic picture of the signal processing and data acquisition.

Fig. 3.4 shows the sketch of the data acquisition electronics. The colors "blue" and "red" label the signals from the "left" and "right" spectrometers (see Fig. 3.8), respectively. The color "yellow" defines the "coincidence events" signal. The left side of the panel shows the input signals: two "X, Y", two "strobe" and two "MCP pulse" signals. The "X, Y" are two analog signals, whose amplitudes are proportional to the X and Y coordinates of the electron impact position. The strobe signal indicates that a valid impaction position determination has been performed. The "MCP pulse" signal provides the fast timing information of the detected electron.

The “MCP pulse” signal from a detector is amplified (PS 775) and passed through a Constant Fraction Discriminator (CFD, Canberra 2126), which outputs Nuclear Instrumentation Module (NIM) pulses for further processing. The NIM signal triggers a delay generator (PS 794), where the pulse width is adjusted to 100 ns, and then is replicated by a linear gate (PS 740), one of these signals is fed into the coincidence unit (PS 756), while another signal goes into the digitizer (PXD 514).

The “strobe” signal from (blue or red) detector firstly are delayed (PS 794) to keep pace with MCP pulse signal and then fed into the coincidence unit (PS 756). When the two input channels of coincidence unit (PS 756) overlap, a valid single electron event is defined. The outputs of the two coincidence units (PS 756) marked with “blue” and “red” box, are fed into the third coincidence unit (yellow box). In the case of an overlap between the two pulses, a valid coincidence event is defined (arrival time difference is less than 100 ns), and the output will trigger four digitizers, where the two timing and two position “X, Y” signals are recorded. The data is transferred to PC for further analysis.

## 3.3 Ion source

For ($\alpha$, 2e) experiments, to have enough interaction time between ions and surfaces low energy ions (tens of eV) are required. However most of the commercial ion sources provide ions with energies above a few hundreds of eV. In order to obtain low energies, while keeping the high transmission and sharp focus, some modifications of a commercial ion gun (IQE 12/38 from SPECS) were made. These modifications were done by Dr. Tusche [82]. The key idea is to operate the ion gun at 2 KeV beam energy, but to float the gun with respect to the ground potential. The diagram of the ion gun is schematically shown in Fig. 3.5.

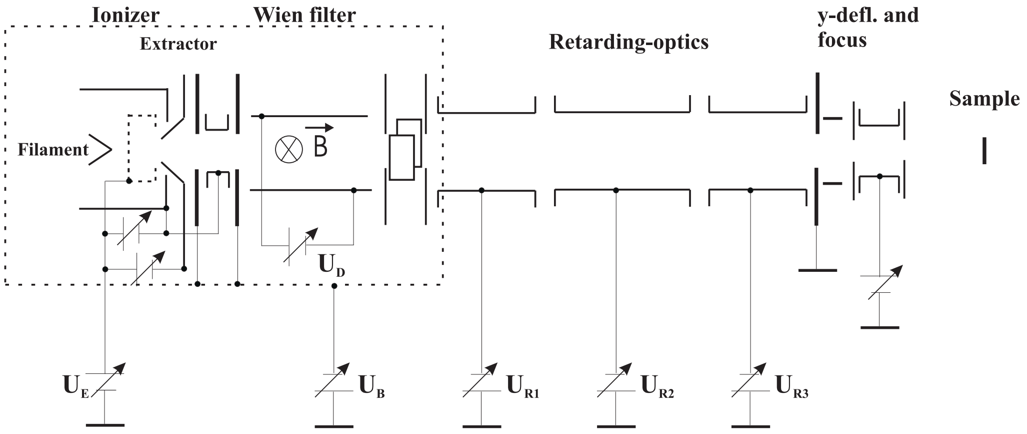

**Figure 3.5:** Schematic diagram of the low energy ion source

### 3.3.1 Ionizer

The neutral gas atoms are ionized by electron collision inside the ionizer. After emitted from the filament, electrons are accelerated towards the anode and enter the inner grid cylinder with an energy of about 100 eV, where they may bombard the neutral gas atoms, ionize them and form an electron-ion plasma [83]. The conical shape extractor electrode extracts the ions out of the plasma area by an electric potential $U_V = U_E + U_B$, see Fig. 3.5. The velocity of the ions can be obtained by the energy conservation,

$$v = \sqrt{\frac{2QU_V}{m}}, \tag{3.32}$$

where $m$ and $Q$ are the mass and charge of the ion, respectively.

In the experiments, $^3He$ with a purity of 99.997% was used. The possible compositions of the ion beam are $^3He^{2+}$, $^3He^+$ and small amount of impurities $^4He^{2+}$, $^4He^+$ and $H_2^+$. The reason to choose $^3He$ instead of $^4He$ is that the mass-to-charge ratio of $^3He^{2+}$ or $^3He^+$ is different from that of the main impurity $H_2^+$, and this allows to suppress the $H_2^+$ contribution by a Wien-filter.

### 3.3.2 Wien-filter

After extraction, the ions are mass-to-charge selected by a Wien-filter. The Wien-filter consists of a permanent magnet and a pair of electrostatic deflection plates, which are mounted between the magnetic poles to produce an electric field E perpendicular to the magnetic field $B$. The magnetic field is fixed at 1956 Gauss, whereas the electric field $E$ can be adjusted by applying different voltage $U_D$ on the electrostatic deflection plates,

$$E = \frac{U_D}{d}, \tag{3.33}$$

where d is the distance between the two plates.

Within the field region, the ions will experience a Lorentz force and a Coulomb force,

$$\mathbf{F} = Q[(\mathbf{v} \times \mathbf{B}) + \mathbf{E}]. \tag{3.34}$$

Only for the ions with certain velocity $v_0$,

$$v_0 = \frac{E}{B}, \tag{3.35}$$

the net force is zero and the ions can pass through the Wien-filter. Combining the Eqs. 3.32, 3.33 and 3.35 , we get,

$$\frac{m}{Q} = \frac{2U_V B^2 d^2}{U_D^2}. \tag{3.36}$$

By varying the deflecting voltage $U_D$, the ions can be selected by the mass-to-charge ratio, for example, $^3He^+$ and $^3He^{2+}$.

### 3.3.3 Retarding-optics

After leaving the Wien-filter, the kinetic energies of the ions are in the keV range. Both the ionizer and the Wien-filter are floated by a potential $U_B$. To reduce the kinetic energies of the ions down to tens of eV, a homemade retarding-optics, which is composed of a three element electrostatic lens, is inserted between the Wien-filter and original ion gun focus components. The kinetic energy of the ions entering the retarding-optics is $QU_C$=$Q(U_E - U_B)$, where $U_E$ is the anode potential. The kinetic energy of the ions at the sample is $QU_E$, and the retarding ratio is defined as,

$$R = \frac{U_C}{U_E}. \tag{3.37}$$

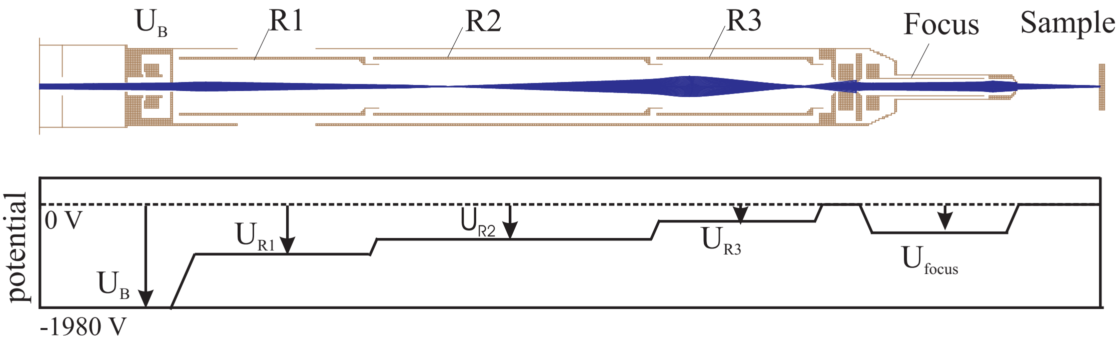

**Figure 3.6:** Sketch of the retarding-optics components. The simulated [84] ion trajectories for the ion beam with an initial kinetic energy of 4 keV are shown in blue. The lower part indicates the voltage applied to the lens elements.

Fig. 3.6 shows the simulation of the trajectories of a bunch of $^3He^{2+}$ ions, with $U_E$ = 20 V, $U_B$ = -1980 V. The kinetic energy of $He^{2+}$ ions entering the retarding lens is 4000 eV. The beam energy is retarded by 3 steps, and the final beam energy is $QU_E$ = 40 eV. The retard ratio in this case is $R$ = 100, with a transmission of 90% and a beam focus of 3 mm at the sample.

## 3.4 The UHV system

Fig. 3.7 shows the UHV chamber used for the purpose of the coincidence spectroscopy. The chamber is equipped with two wide angle transfer lenses, two hemisphere electron energy analyzers (Scienta R4000) and two micro-channel plates (MCP) mounted at the exits of the hemispheres. For the ($\alpha$,2e) experiments, a modified commercial ion gun (Sec. 3.3) was mounted. It can also be equipped with an electron source or a photo source to perform the (e,2e) and ($\gamma$,2e) experiments. For all the measurements, the sample preparations were carried out in-situ.

Fig. 3.8 shows the sketch of the ($\alpha$,2e) experiment. The kinetic energies of the two emitted electrons are measured by two hemispherical analyzers, referred to as "left" and "right", respectively. A primary ion beam is aligned parallel to the surface normal. The two transfer lenses are symmetrically aligned, 45° with respect to the surface normal, with the acceptance angle ±15°. The electronic optical components were optimized to have a high transmission and kept constant during the coincidence experiments.

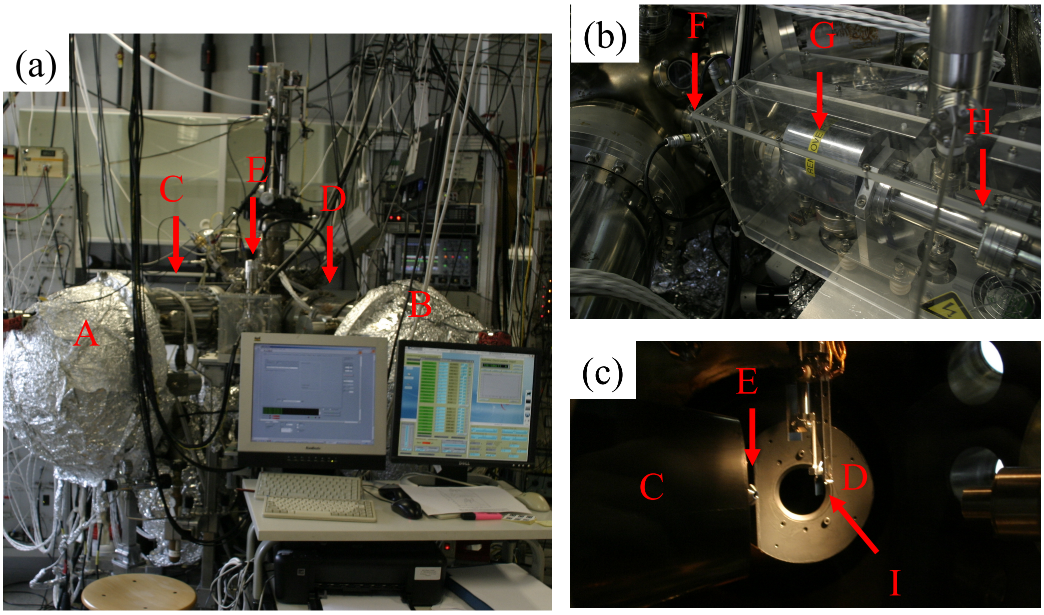
(a)
C
E
D
A
B
(b)
F
G
H
(c)
E
C
D
I

**Figure 3.7:** Photo of the UHV system (a), the ion gun (b), and the sample (c). A and B label the left and right hemispheres, while C and D mark their transfer lenses. E: the end of the ion gun, F: home made retarding optics, G: Wien-filter, H: ionizer, I: sample.

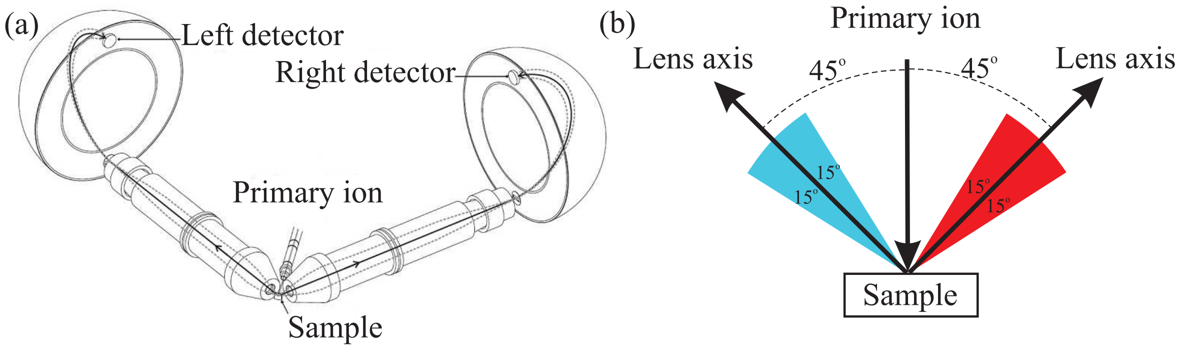
(a)
Left detector
Right detector
Primary ion
Sample
(b)
Primary ion
Lens axis
45°
45°
Lens axis
15°
15°
15°
15°
Sample

**Figure 3.8:** Sketch of the ($\alpha$,2e) experiment. A primary ion beam is aligned parallel to the surface normal, and the two lens axes are ±45° with respect to the surface normal, with the acceptance angle in the scattering plane ±15°.

## 3.5 Sample preparation

For the ($\alpha$,2e) experiments, we have prepared two types of surfaces, Ir(100) and Fe(100)-p(1×1)O thin films grown on Ir(100) substrate.

A well polished Ir(100) crystal was used in the study and was cleaned according to a procedure, similar to the case of tungsten [85]. It consists of two steps.

The aim of the first step is to remove the carbon contamination. As shown in Fig. 3.9(a), cycles of low temperature flashes (∼700 K) were performed in an oxygen atmosphere ($P_{O_2} = 5 \times 10^{-8}$ mbar). The partial pressure of CO inside the UHV chamber, which was measured by a quadrupole mass spectrometer, is presented as a function of time. As the low temperature flash power is switched on and off, the CO partial pressure increases and decreases correspondingly. As more cycles of low temperature flashes are applied, the CO partial background pressure decreases continuously.

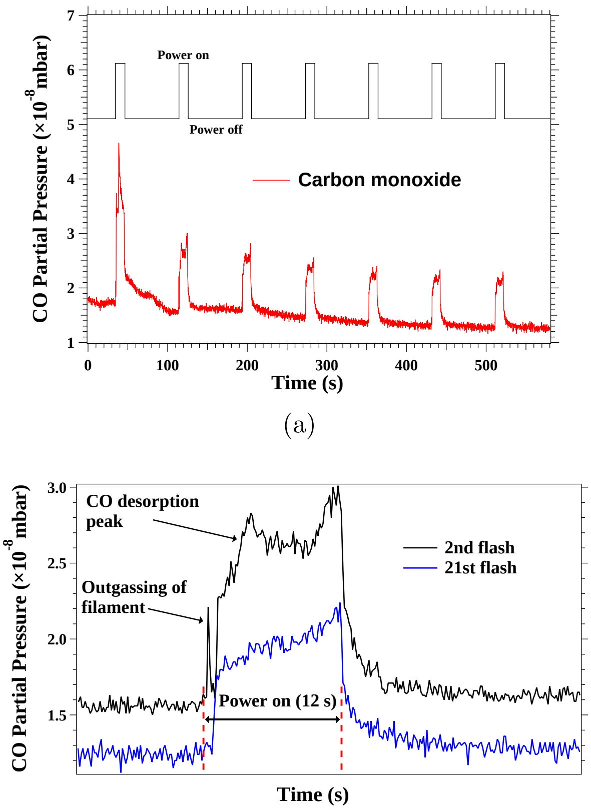

(a)

(b)

**Figure 3.9:** (a) The CO partial pressure as a function of time during cycles of low temperature flashes (∼700 K), in an oxygen atmosphere ($P_{O_2} = 5 \times 10^{-8}$ mbar). (b) The amplifications of the CO partial pressure as a function of time during the 2nd flash and the 21st flash.

Fig. 3.9(b) shows the detailed variation of the CO partial pressure during the 2nd and 21st low temperature flash cycles. In the 2nd cycle, the spectrum shows a sharp peak after the power is switched on, which is due to outgassing of the filament. This feature is followed by an increase of CO partial pressure due to the heat dissipation into the sample holder, giving rise to a flat background in the spectra. In addition, a CO desorption peak arises above the background. This peak is due to the chemical reaction of the oxygen with the segregated carbon from the bulk to surface. After cycles of low temperature flashes, the peak from the filament and sample decreases and finally disappears (see the 21st cycle). This means the carbon in the sample bulk and surface was removed.

The aim of the second step is to remove the oxide layer, through applying a single high power flash ($\sim$1600 K) on the Ir(100) sample.

The Fe(100)-p(1×1)O surface was prepared by evaporating a thick Fe film (estimated coverage 40 ML) onto the Ir(100) substrate, and then exposing it to oxygen at $P_{O_2} = 5 \times 10^{-8}$ mbar for 100 s and subsequent annealing to 700 K.

The clean Ir(100) and Fe(100)-p(1×1)O surfaces can be kept about one day in the UHV environment ($P = 5\times11^{-10}$ mbar). To desorb the contaminants (CO, $H_2O$), a single low temperature flash ($\sim$700 K) was applied every day.

# Chapter 4

# Experimental results

The experimental results of the pair emission from Ir(100) and Fe(100)-p(1×1)O surfaces upon $He^{2+}$ impact are presented in this chapter. The corresponding experimental setup and sample preparation are introduced in Secs. 3.4 and 3.5, respectively.

For the conventional ion neutralization spectrum, referred to as non-coincidence spectrum, we scanned the electron energy with a constant pass energy of 50 eV. The energy resolution is 0.2 eV. During the corresponding coincidence experiments, instead of scanning, we use a pass energy of 300 eV and keep the lens voltages of the spectrometers fixed during the experiments. The energy resolution of one spectrometer is 0.7 eV. The spectrometer covers an energy interval of 9% of the pass energy. Therefore, the energy window is 27 eV × 27 eV. The advantage of this operation mode is that the kinetic energies of the two emitted electrons can be measured over a large energy window by the two spectrometers in parallel. An important parameter for the hemispherical spectrometer is the mean kinetic energy $E_k$, which is the middle energy in the energy window, corresponding to the center impact position on the micro-channel plate. By varying the $E_k$ of the two spectrometers, different 2D-energy distribution regions can be studied.

As the non-coincidence and coincidence spectra are measured by two different manners, it is important to guarantee that the two corresponding electron transmissions are consistent with each other. To do that, we have simulated the electron-optical components by a commercial software [84]. An acceptable setting is defined such that the non-coincidence spectra measured by the two manners are quite similar to each other, and the main features of the non-coincidence spectra should be both reflected.

## 4.1 Non-coincidence spectra

In Figs. 4.1(a) and 4.2(a), we report the non-coincidence spectrum (blue dots) upon the impact of 5 eV $He^+$ on Ir(100) and O/Fe(100), respectively. The original data are smoothed by the Savitzky-Golay method (black lines). The smoothed data are used to calculate the derivative spectrum, shown in the lower panel. The dashed line labels the high energy edge of the spectrum. The high energy edge is best observed in the derivative spectrum, where it corresponds to a minimum, 10.8 eV for Ir(100) and 7.8 eV for O/Fe(100). See the neutralization scheme of $He^+$ in Fig. 2.5, there are two neutralization paths: (i) Auger capture (AC); (ii) resonant capture (RC) followed by Auger

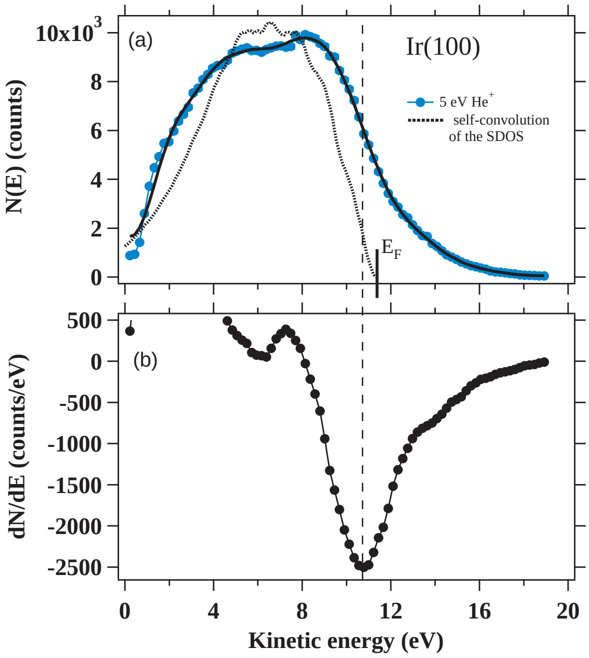

**Figure 4.1:** (a) Non-coincidence spectrum (blue dots) for the collision of normal incident 5 eV He$^+$ on the Ir(100) surface. The original data are smoothed by the Savitzky-Golay method (black line). The black-dotted curve shows the self-convolution of the density-of-states (SDOS) of Ir(100), see Fig. 4.3. $E_F$ is the Fermi level, 11.26 eV. (b) The derivative spectrum $dN(E)/dE$ is calculated from the smoothed spectrum. The dashed line at 10.8 eV labels the high energy edge of the spectrum $N(E)$.

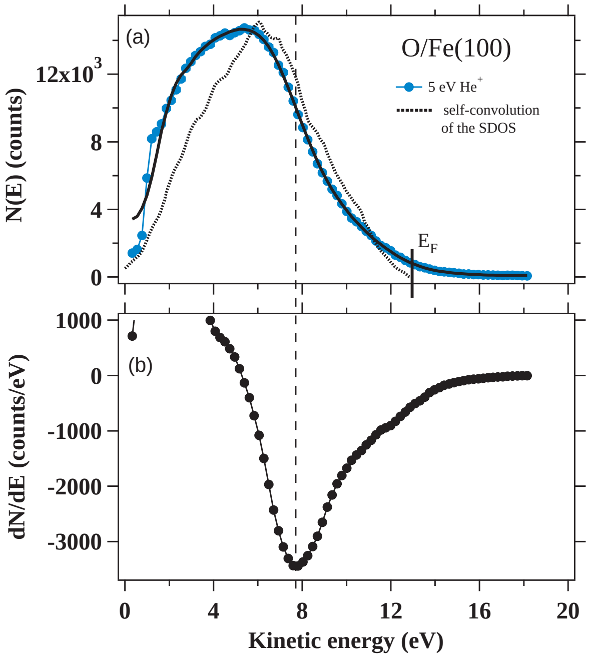

**Figure 4.2:** Similar to Fig. 4.1, but for O/Fe(100). The high energy edge and the $E_F$ is at 7.8 eV and 12.8 eV, respectively.

deexcitation (AD). The path (ii) is the following one, $\mathrm{He}^+(1s)+\mathrm{M} \xrightarrow{RC} \mathrm{He}^*(1s,2s)+\mathrm{M}^+ \xrightarrow{AD} \mathrm{He}^0+\mathrm{M}^{2+}+e$, where "M" stands for the metal surface. The one-electron potential of $\mathrm{He}^*(1s,2s)$ is 4 eV below the $\mathrm{He}^+(1s)$ state, see Table 2.1. This means, in the case of Ir(100) ($W = 5.67$ eV) and O/Fe(100) ($W = 4.9$ eV), the one-electron potential of $\mathrm{He}^*(1s,2s)$ lies above the Fermi level. Therefore, the RC is not energetically allowed. Consequently, the path (i), i.e. AC, $\mathrm{He}^+ + \mathrm{M} \xrightarrow{AC} \mathrm{He}^+ + \mathrm{M}^{2+}+e$, is the only path for the neutralization of $\mathrm{He}^+$ on Ir(100) and O/Fe(100) surfaces.

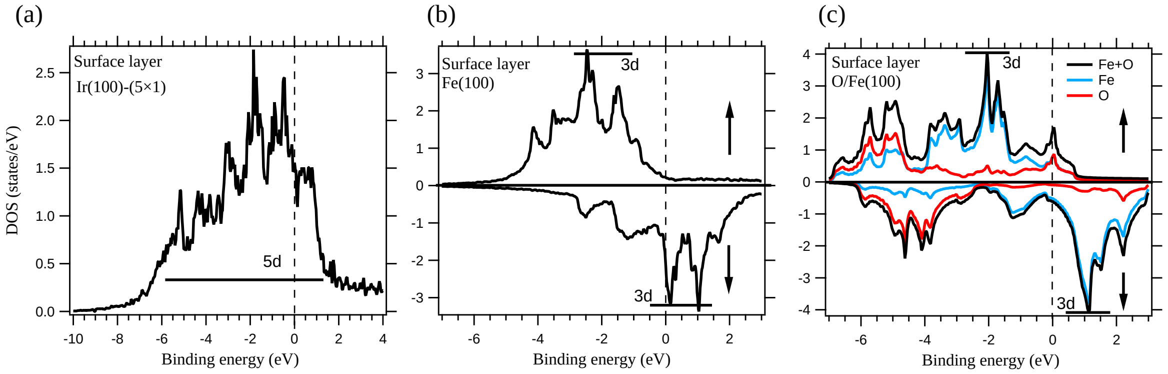

**Figure 4.3:** Calculated surface density-of-states (SDOS) for Ir(100) (a), Fe(100) (b), and O/Fe(100) (c). The calculations for (b) and (c) are spin resolved, published in Ref. [86]. In panel (c), the blue, red, and black lines represent the SDOS for the Fe, O, and Fe+O, respectively.

As introduced in Sec.2.1.2, the energy distribution of the electrons emitted by AC reflects the self-convolution of the surface density-of-states (SDOS). Therefore, in order to interpret the spectrum, it is useful to discuss the electronic band structure of Ir(100) and O/Fe(100). We present the calculated [87] SDOS of Ir(100), Fe(100) and O/Fe(100) in Fig. 4.3. The SDOS of Fe(100), and O/Fe(100) is spin resolved, and has been published in Ref. [86]. The DOS of Ir(100) originates mainly from the 5d band, which is half filled. The case for clean Fe(100) is similar, the main contribution is from the 3d band, and the 3d(↓) band is half filled. It should be noticed, the situation for O/Fe(100) is different. In case of O/Fe(100), the Fe 3d(↓) band is shifted 1 eV above the Fermi level and becomes unoccupied. The main contributions of the occupied SDOS are from Fe 3d(↑) band (2 eV below $E_F$) and O 2p band (5.5 eV below $E_F$). The SDOS between the Fe 3d(↑) and the Fermi level is relatively low.

For the purpose of comparison, the self-convolution of the SDOS of Ir(100) and O/Fe(100) is presented in Figs. 4.1(a) and 4.2(a), respectively. These are shown as dotted curves. The position of the Fermi level is calculated as follows. In AC, two valence electrons have over come the vacuum barrier, one is emitted to the vacuum, the other is captured by the ion. In addition, we have to consider the atomic level shift ($\delta_1$) due to the ion-surface interaction, see Sec. 2.1.3. The atomic level shift is a function of the ion-surface distance. According to literature [54, 56], the most likely neutralization position for slow $\mathrm{He}^+$ (tens of eV) is around the jellium edge. This corresponds to $\delta \sim 2$ eV, see Fig. 2.4. Therefore, the energy for the Fermi level is given by, $E_F = E_b - \delta - 2W$, where $E_b$ is the ionization potential of $\mathrm{He}^+$, 24.6 eV. The numerical

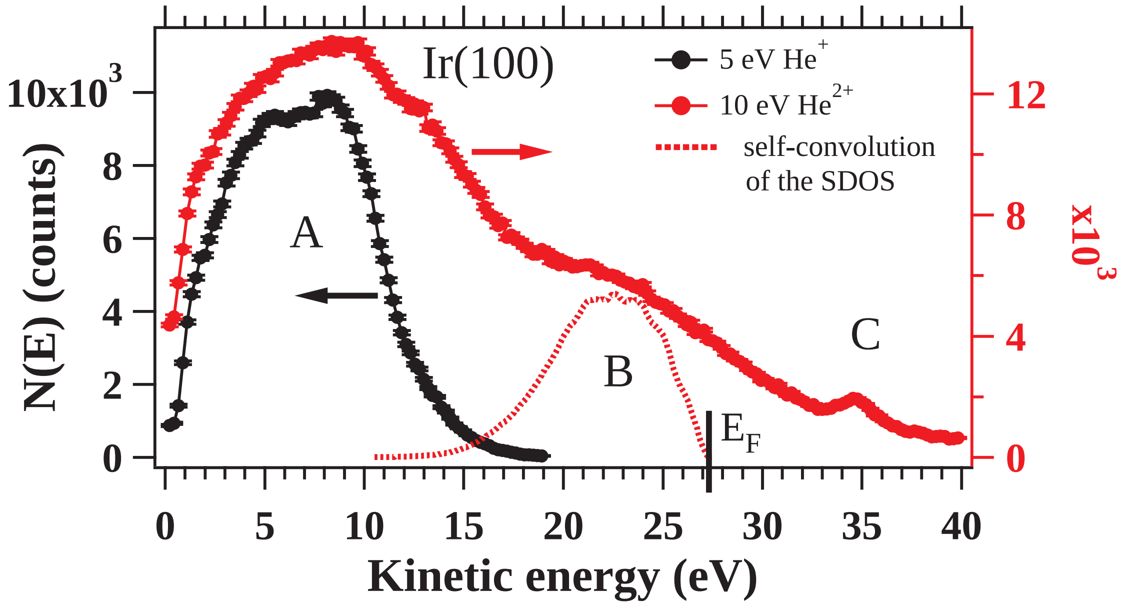

**Figure 4.4:** (a) Non-coincidence spectrum for the collision of normal incident 10 eV He$^{2+}$ (blue dots) on the Ir(100) surface. The black-dotted curve shows the AC(2,0) emission, which is the self-convolution of the density-of-states (SDOS) of Ir(100). The corresponding Fermi level is at 27.07 eV.

result is 11.26 eV for Ir(100), 12.8 eV for O/Fe(100). The AC can also take place at a longer ion-surface distance, but with a lower probability. The ion-surface distance $z$ is with respect to the jellium edge. For $z \to \infty$ , $\delta \sim 0$ eV, and this defines the maximum kinetic energy.

In Figs. 4.1(a) and 4.2(a), the self-convolution of the SDOS can qualitatively explain the He$^+$ spectrum. For Ir(100), the high energy edge of 10.8 eV is close to the Fermi level 11.26 eV. In this case, the high energy edge reflects the Fermi edge. For O/Fe(100), the high energy edge at 7.8 eV is far from the Fermi level 12.8 eV, but close to the energy for the Fe 3d(↑) band (2 eV below $E_F$) 8.8 eV. This is because, for O/Fe(100), the SDOS around the Fermi level is relatively low, by contrast the Fe 3d(↑) band is more pronounced. Therefore, the high energy edge at 7.8 eV reflects the edge of Fe 3d(↑) band.

It should be noticed that there are still non-negligible counts above the high energy edge. They are due to the energy broadening in the ion neutralization [88]. The mechanisms of the broadening effect can be, the uncertainty of the atomic level shift, and finite lifetime of He$^+$ in front of a metal surface. The broadening effect is smaller for slow ions. For the ions around several eV, the broadening effect is about 4 eV [88].

In Figs. 4.4 and 4.5, we report the non-coincidence spectrum (red dots) upon the impact of 10 eV He$^{2+}$ on Ir(100) and O/Fe(100), respectively. The He$^+$ spectrum (blue dots) is displayed for comparison. We want to mention that, for slow ions (tens of eV), the kinetic energy of the ion does not play a role in the ion neutralization spectrum. The advantage to choose 5 eV He$^+$ and 10 eV He$^{2+}$ is that the acceleration voltage of the ion gun can be kept constant. The He$^{2+}$ spectrum displays three pronounced features, labeled as A, B, and C. For Ir(100), they are two wide peaks centered at 9 eV (A), 23

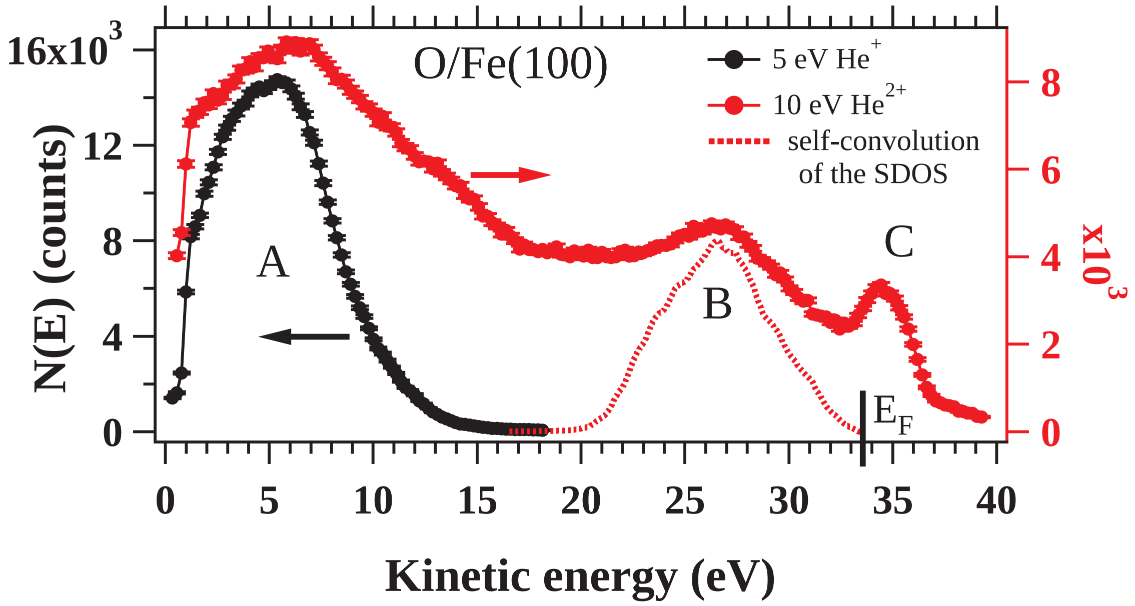

**Figure 4.5:** Similar to Fig. 4.1, but for O/Fe(100). The Fermi level is at 33.06 eV.

eV (B), and a narrow peak at 35 eV (D). For O/Fe(100), they are at 6 eV (A), 27 eV (B) and 35 eV (C). These features resemble the previously reported spectra [23, 30, 89].

The feature C (35 eV) is assigned to the KLL AI process, which is an intra-atomic Auger decay, He**(2l,2l') $\xrightarrow{KLL\ AI}$ He$^+$(1s)+$e_1$. The first emitted electron during the neutralization of He$^{2+}$ is denoted by $e_1$, while with $e_2$ the second electron is labeled. The He**(2l,2l') is formed via resonant capture by two valence electrons of the metal, He$^{2+}$ $\xrightarrow{RC}$ He$^{+*}$(2l) $\xrightarrow{RC}$ He**(2l,2l'). In literature [30, 47, 48], the KLL AI shows a double-peak feature around 35 eV. The lower energy peak is attributed to the He**$(2s^2)$ $^1S$ and (2s2p) $^3P$ states, and the higher energy peak is attributed to the He**$(2p^2)$ $^1D$ and (2s2p) $^1P$ states. However, in the case shown in Figs. 4.4 and 4.5, only a single peak is observed. The potential levels of the $^1D$, $^1P$, $^1S$ and $^3P$ states are 5.26 eV, 5.5 eV, 7.09 eV and 7.57 eV below the He$^{+*}$(2s) state. For the RC transition, He$^{+*}$(2l) $\xrightarrow{RC}$ He**(2l,2l'), by taking into account the atomic level shift, about several eV, the $^1D$ and (2s2p) $^1P$ states lie above the Fermi level. Hence, they can not be populated via RC. The peak at 35 eV has to be attributed to the KLL AI of the $^1S$ and $^3P$ states. This resembles the scattering of He$^{2+}$ on Ni(100) ($W = 4.61$ eV) [90]. It can be observed that the feature C is more pronounced for O/Fe(100) than for Ir(100). The RC transition takes place when the potential barrier between the surface and the ion is lowered down to the Fermi level, COB model, see Sec. 2. This critical neutralization distance is, $z_c = 2\sqrt{q}/W$ (atomic units). The numerical result is $z_c = 10.3$ a.u. and 11.2 a.u. for Ir(100) and O/Fe(100), respectively. For the same perpendicular velocity of the ion, the longer distance means that there are more time available for the KLL AI decay of He**(2l,2l'), and more intensity of feature C.

The feature B is extending from 17 eV to 33 eV. According to literature [23], this feature is assigned to AC(2,0), He$^{2+}$+M $\xrightarrow{AC(1,0)}$ He$^+$+M$^{2+}$+$e_1$. As introduced above, the energy distribution of AC(2,0) can be estimated by the self-convolution of SDOS.

The self-convolution of SDOS for Ir(100) and O/Fe(100) is presented as dashed curves in Figs. 4.4 and 4.5, respectively. The energy of the Fermi level is given by, $E_F = E_b - \delta_2 - 2W$, where $E_b$ is neutralization energy for $\mathrm{He}^{2+} \rightarrow \mathrm{He}^{+}$, 54.4 eV, $\delta_2$ is the corresponding atomic level shift. The atomic level shift for AC(1,0) is labeled as $\delta_1$. The value of $\delta_2$ is not well known. To match the peak position of feature B, we choose $\delta_2 = 16$ eV and 11 eV for Ir(100) and O/Fe(100), respectively. We estimate when the $\mathrm{He}^{2+}$ is at a distance $z \geq 1$ a.u. (the radius of the $\mathrm{He}^{2+}$-1s orbital is 0.5 a.u.), the atomic level shift for the transition $\mathrm{He}^{2+} \rightarrow \mathrm{He}^{+}$ can be described by the image model, which follows $3/4z$. Then, the most likely neutralization distance of AC(2,0) for Ir(100) ($W = 5.67$ eV) and O/Fe(100) ($W = 4.9$ eV) is $z = 1.3$ a.u. and 1.9 a.u, respectively. For Ir(100), the most likely neutralization position is closer to the surface. This could be understood as follows. According to the jellium model, the electron density in vacuum is proportional to exp(-$az$), where $a = \sqrt{W - E}$, $E$ is the electron energy with respect to the Fermi level. For a higher work function surface, the electron density above the surface is lower, thus the ion has to come closer to the surface to get sufficient orbital overlap for the transition.

The feature A (or called low-energy component in literature) is extending from 0 eV to 15 eV for Ir(100), from 0 eV to 11 eV for O/Fe(100). The feature A appears to be identical with the $\mathrm{He}^{+}$ spectrum. This feature is assigned to AC(1,0) in literature [30, 89], $\mathrm{He}^{+}+\mathrm{M}^{2+} \xrightarrow{AC(1,0)} \mathrm{He}^{0}+\mathrm{M}^{4+}+e_2$. AC(1,0) is the same for the AC of $\mathrm{He}^{+}$, without considering the difference on surface. The similarity between the feature A and the $\mathrm{He}^{+}$ spectrum reflects this point. A difference between them should be noticed. The feature A is broader at the high energy side. This could be understood as follows. As explained in Sec. 2.1.4, for a primary $\mathrm{He}^{+}$, the most likely neutralization position is around the jellium edge. For a primary $\mathrm{He}^{2+}$, the AC(1,0) occurs after the transitions KLL AI or AC(2,0). Therefore the most likely neutralization distance of AC(1,0) could be closer to the surface, i.e. below the jellium edge. See Fig. 2.4, this can lead to the $\mathrm{He}^{+}$-1s level being pulled down further. In the coincidence experiments, it can be observed that the high energy edge for AC(1,0) is about 15 eV for Ir(100), and 11 eV for Fe(100). This corresponds the atomic level shift $\delta_1 =$ -4 eV, and the most likely distance $z =$ -1 a.u..

Note the neutralization scheme for $\mathrm{He}^{2+}$ in Fig. 2.7, there is another path AD(1,1) for the emission of $e_2$, $\mathrm{He}^{*}(1s, 2s)+\mathrm{M}^{3+} \xrightarrow{AD(1,1)} \mathrm{He}^{+}(1s)+\mathrm{M}^{4+}+e_2$. As announced, in the case of Ir(100) and O/Fe(100), the one-electron potential of $\mathrm{He}^{*}(1s, 2s)$ lies above the Fermi level. Hence, the $\mathrm{He}^{*}(1s, 2s)$ can be resonant ionized, $\mathrm{He}^{*}(1s, 2s)+\mathrm{M}^{3+} \xrightarrow{RI} \mathrm{He}^{+}(1s)+\mathrm{M}^{2+}$. The resonant ionization is fast, leading to a low population of $\mathrm{He}^{*}(1s, 2s)$. Therefore, the AD(1,1) is very unlikely compared to the AC(1,0). For the collision of $\mathrm{He}^{*}(1s, 2s)$ on a metal surface, the highest value of the branching ratio $\Gamma(\mathrm{AD})/\Gamma(\mathrm{AN})$ was found of the order of $10^{-2}$-$10^{-3}$, in the case of Au(111) surface [22]. For simplicity, the AD(1,1) is omitted.

We can make a summary for the $\mathrm{He}^{2+}$ non-coincidence spectrum. There are three features can be explained by the sequential neutralization scheme, AC(1,0) (feature A), AC(2,0) (features B), and KLL AI (feature C). In the transition AC(2,0) and KLL AI, the first electron ($e_1$) is emitted. The second electron ($e_2$) is from the transition AC(1,0). The highest energy of $e_1$ is about 37 eV for Ir(100) and O/Fe(100), and of $e_2$ is about 15 eV for Ir(100) and 11 eV for O/Fe(100). In the coincidence experiment, it

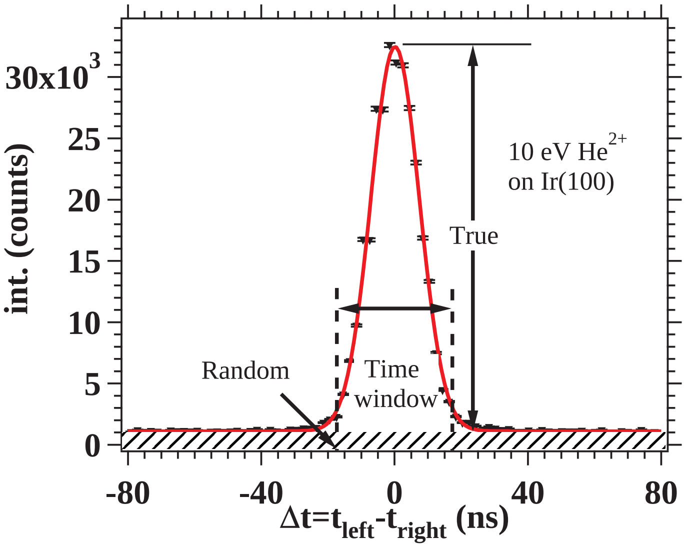

**Figure 4.6:** Events versus arrival time differences (Δt) for all detected electron pairs (solid triangles) obtained by the collision of 10 eV $He^{2+}$ ions on the Ir(100) surface. The red line is guide to eyes. The two spectrometers were both set to mean kinetic energies $E_k$ = 19 eV, pass energies $E_{pass}$ = 300 eV (energy window = 27 eV × 27 eV). The background (shaded area) is due to the random coincidences, and the peak above the background is due to the true coincidences. A time window is defined by two vertical dashed black lines at $\Delta t = \pm 18$ eV. The inset shows the same spectrum but for the collision of 5 eV $He^{+}$ on the Ir(100) surface. In this case, the two spectrometers were both set to $E_k = 6$ eV and $E_{pass} = 100$ eV (energy window = 9 eV × 9 eV). In contrast, there is no peak.

is expected to detect the ($e_1$, $e_2$) electron pair. There are also events which can not be assigned to the sequential neutralization scheme, i.e. the intensity between the AC(1,0) and AC(2,0) (15-20 eV). In principle there should be a gap separating the AC(1,0) peak and the AC(2,0) peak. However, the spectrum shows a continuous emission. This issue has also been noticed by Lorente *et al* [65]. The explanation of Lorente *et al* is that the events between the two peaks are due to the cascade electron emission produced by the AC electrons. In the coincidence experiment, we will provide new evidence for these events. These evidence indicate they are due to the energy sharing between the two emitted electrons.

## 4.2 Coincidence spectra of Ir(100)

In a coincidence experiment, we first study the arrival time difference (Δt) distribution for the electron pairs, see Sec. 3.1.1. Fig. 4.6 shows a typical histogram (solid triangles), which is obtained from the collision of 10 eV $He^{2+}$ ions on the Ir(100) surface. The two spectrometers were set to the mean kinetic energies $E_k$ = 19 eV, pass energies $E_{pass}$ = 300 eV. A clear peak can be observed on an essentially constant background (shaded area). The emergence of this peak is due to true coincidences, i.e. two electrons being emitted from the same collision event. The background is due to random coincidences, i.e. two electrons being emitted by two different collision events. The width of the peak is 18 ns, which reflects the time resolution of our instrument. A time window is selected, shown by the two dashed lines. The electron pairs inside the time window were used for further analysis, see Fig. 4.7. Inside the time window, the area between the peak and the baseline is proportional to the true coincidence events, and the area below the baseline is proportional to the random coincidence events. The true/random coincidence ratio can be estimated by comparing these two areas. In the case shown in Fig. 4.6, it is about 14, with a true coincidence count rate of 5.8 counts per second (cps) and a single count rate of 3500 cps for each detector.

The inset of Fig. 4.6 displays the arrival time difference histogram obtained by the collision of 5 eV normal incident $He^+$ ions on the Ir(100) surface. The two spectrometers were set to $E_k = 6$ eV and $E_{pass} = 100$ eV. The corresponding energy interval is about 1.5-10.5 eV, which almost covers the energy range of the non-coincidence spectrum shown in Fig. 4.1. With a single count rate of 2200 cps, in contrast to $He^{2+}$, there is no peak in the time histogram. It is essentially flat and therefore dominated by random coincidences. For the impact of $He^{2+}$ and $He^+$ ions, the single count rates in the two experiments are very close. Therefore, by a rough estimate, the two primary fluxes should have the same order of magnitude. This indicates that the cross section of the pair emission by primary $He^+$ is negligible compared to that by primary $He^{2+}$. The ionization potential $E_b$ of $He^+$ is 24.6 eV, and the maximum primary energy released during the ion neutralization is $E_b$ - $W$ = 18.93 eV ($W$ = 5.67 eV), corresponding to one valence electron from the Fermi level being captured into the He-1s level. We want to emphasize that the primary energy of 18.93 eV exceeds the threshold of the electron pair emission, which is twice the work function of Ir(100) ($2W$ = 11.34 eV). Therefore, the pair emission by $He^+$ is energetically allowed in the case. The question why the pair emission by the impact of $He^+$ has not been observed is still open.

In Fig. 4.7(a), we display the 2D-energy spectrum, generated by using the intensity inside the time window in Fig. 4.6. The two axes are the individual energies $E_{left}$ and $E_{right}$, corresponding to the two electrons detected by the "left" and "right" spectrometers (see Fig. 3.8), respectively. In the coincidence experiments, we use the sample current to monitor and quantify the primary flux. The data are normalized by the same primary flux, corresponding to sample current 1 pA. It should be noticed that, the 2D-energy spectrum plotted directly using the intensity inside the time window, contains the contributions both from true and random coincidences. We refer to such a spectrum as raw 2D-energy spectrum. Although it is impossible to separate the true and random coincidences, there is a method to remove approximately the contribution of the random coincidences [91]. We describe a typical procedure here. At first, we plot a 2D-energy spectrum in panel (b), with the events outside the time window. The spectrum is normalized to let the interval of Δt be same as the width of the time window. These events are random coincidences. We refer to this spectrum as random 2D-energy spectrum. We assume that the random 2D-energy spectrum is independent of the arrival time difference. In this case, the random 2D-energy spectrum plotted in this way is the same for the random coincidences inside the time window. Then, we subtract the random 2D-energy spectrum from the raw 2D-energy spectrum. At last, we get a spectrum in panel (c), mainly with the contribution of the true coincidences. We call it net 2D-energy spectrum. In the following, we only present the net 2D-energy

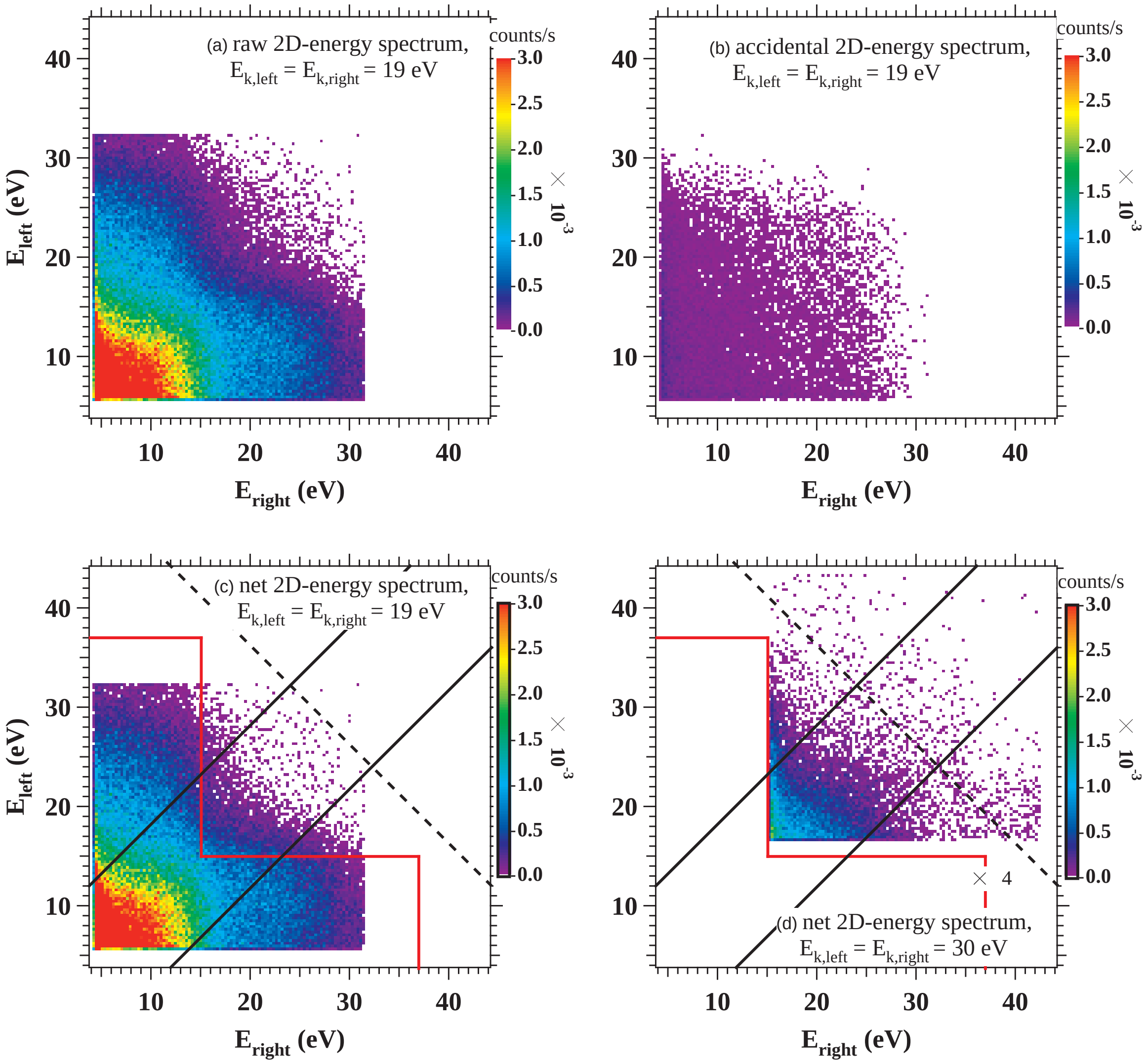

**Figure 4.7:** (Color) (a) Raw 2D-energy spectrum, plotted with the events inside the time window of Fig. 4.6. (b) Random 2D-energy spectrum, plotted with the events outside the time window, and normalized to have the same time interval as (a). (c) Net 2D-energy spectrum, obtained as the subtraction of (b) from (a). The intensity (events/s) is defined by the color bar on the right side. Panels (a-c) are obtained with two spectrometers being set to $E_k$ = 19 eV, while panel (d) is the net 2D-energy spectrum for $E_k$ = 30 eV. The intensity in (d) is multiplied by 4. The red lines at 15 eV and 37 eV, define a L-shaped region, which is expected by the sequential model. The dashed black diagonal lines label the maximum sum energy that an electron pair can have, $E_{sum}^{max}$ = 56.32 eV. The pair of black solid lines label the region, $E_{dif} = E_{right}$ - $E_{left}$ = ± 8 eV, from which the sum energy spectra in Fig. 4.8(a) are obtained.

spectra, which are generated in the same way as described above.

In Fig. 4.7(c), the energy distribution displays a L-shape. The L-shaped distribution is predicted by the sequential neutralization model, with two electrons being emitted by two successive transitions, $\mathrm{He}^{2+}+\mathrm{M} \rightarrow \mathrm{He}^{+}+\mathrm{M}^{2+}+e_1 \rightarrow \mathrm{He}^{0}+\mathrm{M}^{4+}+e_2$. In the discussion for the $\mathrm{He}^{2+}$ non-coincidence spectrum, it has been estimated the highest energy for $e_1$ and $e_2$ is 37 eV and 15 eV, respectively. Since our experimental setup is symmetric, the events inside the “L” region, labeled by the red lines, is expected by the sequential neutralization model.

In Fig. 4.7(c), the interesting observation is made by the events outside the L-shaped region. Since the energies of the two electrons are both higher than the highest energy for $e_2$, 15 eV, these events can not be accounted for by the sequential model. There are two potential arguments for the sequential model. One is that the kinetic energy of the ions can be transferred to the electrons, which is called “kinetic electron emission” [27]. The other one is the broadening effect in ion neutralization [88]. This effect, as discussed in the non-coincidence spectrum, can increase the electron energy by several eV. To clarify the origin of these events, it is advantageous to move the energy window to focus on them. Such a 2D-energy spectrum is shown in Fig. 4.7(d), with both spectrometers being set to $E_k = 30$ eV. In this case, the energy window is totally outside the “L” region. The coincidence count rate is about 0.15 cps, with a single count rates of 2500 cps and a true/random ratio of 2. The coincidence count rate was so low that it took two weeks to collect the data. Note, the 2D-energy spectrum in panel (d) does not display the “L” pattern. This indicates, the picture that $e_1$ and $e_2$ are distributed in two different energy ranges, breaks down.

For an electron pair, it is important to know the maximum sum energy ($E_{sum}^{max}$) that an electron pair can have. This can be directly calculated from energy conservation. In ($\alpha$,2e) the initial and final states are $\mathrm{He}^{2+}+\mathrm{M}$ and $\mathrm{He}^{0}+\mathrm{M}^{4+}$, respectively. Four electrons from the surface have to overcome the vacuum barrier given by the work function $W$. Then, by energy conversation, $E_{sum}^{max}$ is given by,

$$E_{sum}^{max} = E_b - 4W, \tag{4.1}$$

where $E_b$ is the ionization potential of the $\mathrm{He}^{2+} \rightarrow \mathrm{He}^{0}$ (79 eV). In this case, the four electrons are all taken from the Fermi level. The numerical result for Ir(100) is about 56.32 eV, indicated by the dashed lines in Figs. 4.7(c) and (d). Note, for $E_{sum}^{max}$, we assume the atomic level shift is zero, corresponding to a neutralization position far away from the surface.

In the frame work of the sequential neutralization model, the neutralization energy of $\mathrm{He}^{2+}$ (79 eV), is released in two steps, for $\mathrm{He}^{2+} \rightarrow \mathrm{He}^{+}$ (54.4 eV) and for $\mathrm{He}^{+} \rightarrow \mathrm{He}^{0}$ (24.6 eV). This means, only in the very unequal energy region, the $E_{sum}^{max}$ of a pair is 56.32 eV. By contrast, in the equal energy region ($E_{left} = E_{right}$), since the highest energy of $e_2$ is 15 eV, $E_{sum}^{max}$ is 30 eV. Hence, to test the validity of the sequential model, one effective way is to investigate the onset of the pair emission in the equal energy region.

In Fig. 4.8(a), we display the sum energy spectra in the equal energy region. The black and red curves are obtained by integrating the intensity with the constraint, $E_{dif} = |E_{right} - E_{left}| \pm 8$ eV, in Figs. 4.7(a) and (b), respectively. In principle, we should choose the equal energy region to be as narrow as possible. However, to get

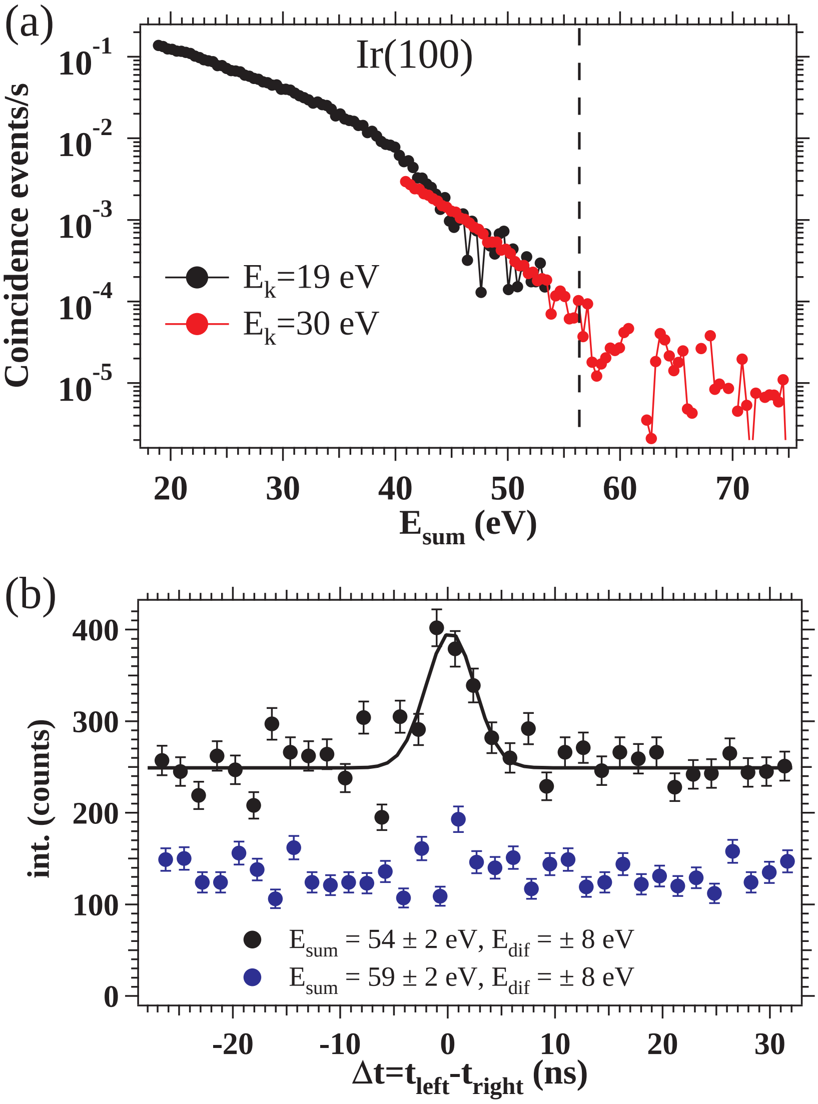

**Figure 4.8:** (a) Sum energy spectra with the constraint, $E_{dif}$ = ± 8 eV. The black and red curves are obtained by integrating the intensity along the region bound by the pairs of the solid lines in Figs. 4.7(c) and (d), respectively. Note the logarithmic scale. (b) Time histograms for the events with the constraint, $E_{sum}$ = 54 ± 2 eV and $E_{dif}$ = ± 8 eV (black), and $E_{sum}$ = 59 ± 2 eV and $E_{dif}$ = ± 8 eV (blue). The events are obtained from the ($\alpha$,2e) experiment for $E_k$ = 30 eV.

sufficient statistics, we have to lower the constraint. Basically, the two curves agree with each other. This is because they are measured for the same ($\alpha$,2e) process, just different energy windows. The coincidence intensity decreases nearly exponentially with increasing the sum energy. The intensity drops roughly three orders of magnitude from $E_{sum}$ = 20 eV to 56 eV. The dashed vertical line labels the maximum sum energy, 56.32 eV. Around the dashed line, the intensity decreases nearly one order of magnitude. This indicates the onset of the true coincidences in the equal energy region is around $E_{sum}^{max}$ = 56.32 eV.

Since the intensity near $E_{sum}^{max}$ is small, we have to double check the onset of pair emission. In the ($\alpha$,2e) experiment for $E_k$ = 30 eV, we select two energy regions: $E_{sum}$ = 54 ± 2 eV and $E_{dif}$ = ± 8 eV, and $E_{sum}$ = 59 ± 2 eV and $E_{dif}$ = ± 8 eV. They are located in the equal energy region, just below and above the $E_{sum}^{max}$, respectively. The events inside these two regions are used to generate the time histograms. These are shown in Fig. 4.8(b). In Fig. 4.8(b), for the black curve (events below $E_{sum}^{max}$), a peak due to "true" coincidences can be observed, with true/random ratio 0.29. By contrast, the blue curve (events above $E_{sum}^{max}$) is featureless and constant, implying that there are no "true" coincidences. In other words, in the 2D-energy spectra, the events above the maximum sum energy are due to the incomplete movement of "random" coincidences.

The results of Figs. 4.8 (a) and (b) together prove that, for the collision of $He^{2+}$ on Ir(100), the pair emission can be found up to the $E_{sum}^{max}$ = 56.32 eV, which is provided by the ionization potential of the $He^{2+} \to He^0$ (79 eV). More importantly, they are in the region where the energies of the two electrons are nearly equal (± 8 eV). In this region, the energy of an individual electron is about 28 eV, much higher than the energy of 15 eV, which is allowed by the sequential model. This rules out the argument of the broadening effect, which can just increase the energy by several eVs. As for the argument of the kinetic energy of the ions (10 eV), if it was involved in the neutralization, the $E_{sum}^{max}$ would be 10 eV more. Moreover, the threshold velocity of the ions for the so-called "kinetic electron emission" is about $10^5$ m/s [27], whereas the perpendicular velocity of the $He^{2+}$ ions in our experiment is just $10^3$ m/s. Therefore the argument of the kinetic energy of the ion can also be ruled out. Consequently, the results of Figs. 4.8 (a) and (b) provide clear proof that there are events can not be understood by the sequential neutralization model. We refer to these events as non-sequential events. The events can be understood by the sequential neutralization model are called sequential events. In the following, we will provide more evidence that the non-sequential events and sequential events coexist in the ($\alpha$,2e). Furthermore, we will give the estimation of the relative contribution of the non-sequential events.

We want to mention, the intensity in the vicinity of the $E_{sum}^{max}$ is little is simplify because the probability that the neutralization takes far away from the surface (to let the atomic level shift be zero) is small. Most of the neutralizations take place in the vicinity of the surface, and the atomic level shift is finite. This dose not indicate the non-sequential process is a small probability event. Actually, the non-sequential events are not limited in the vicinity of the $E_{sum}^{max}$. They can distribute in the whole energetically allowed region.

In the 2D-energy plane, the electron pairs are distributed in a right-angled triangle region, with $E_{sum} \leq E_{sum}^{max}$ = 56.32 eV. This region is larger than the energy window of our coincidence spectrometer (27 eV × 27 eV). Therefore, we have to move the energy

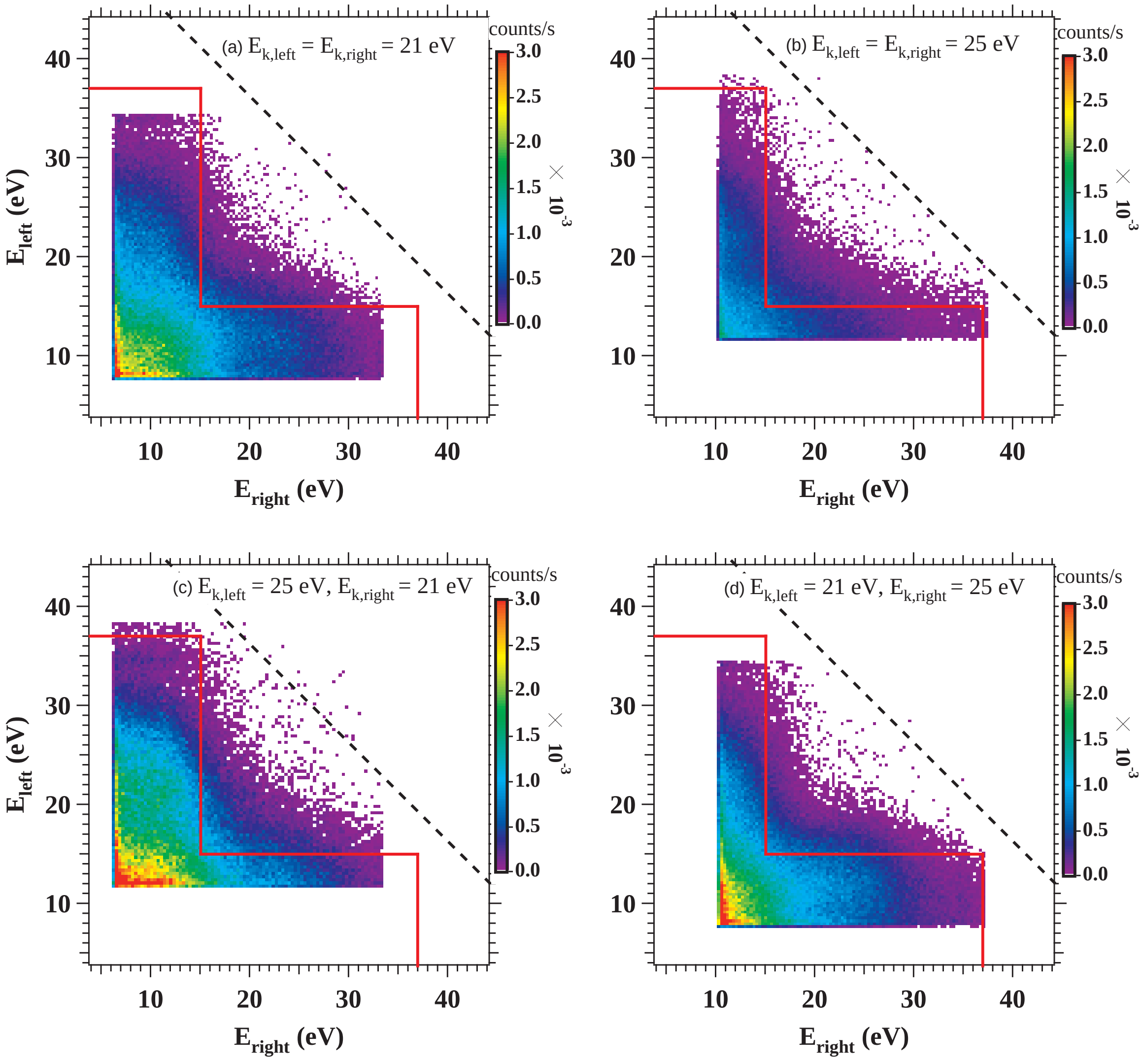

**Figure 4.9:** (Color) As Fig. 4.7, but for different settings of the mean kinetic energies of the two spectrometers: (a) $E_{k,left} = E_{k,right} = 21$ eV (b) $E_{k,left} = E_{k,right} = 25$ eV (c) $E_{k,left} = 25$ eV, $E_{k,right} = 21$ eV and (d) $E_{k,left} = 21$ eV, $E_{k,right} = 25$ eV.

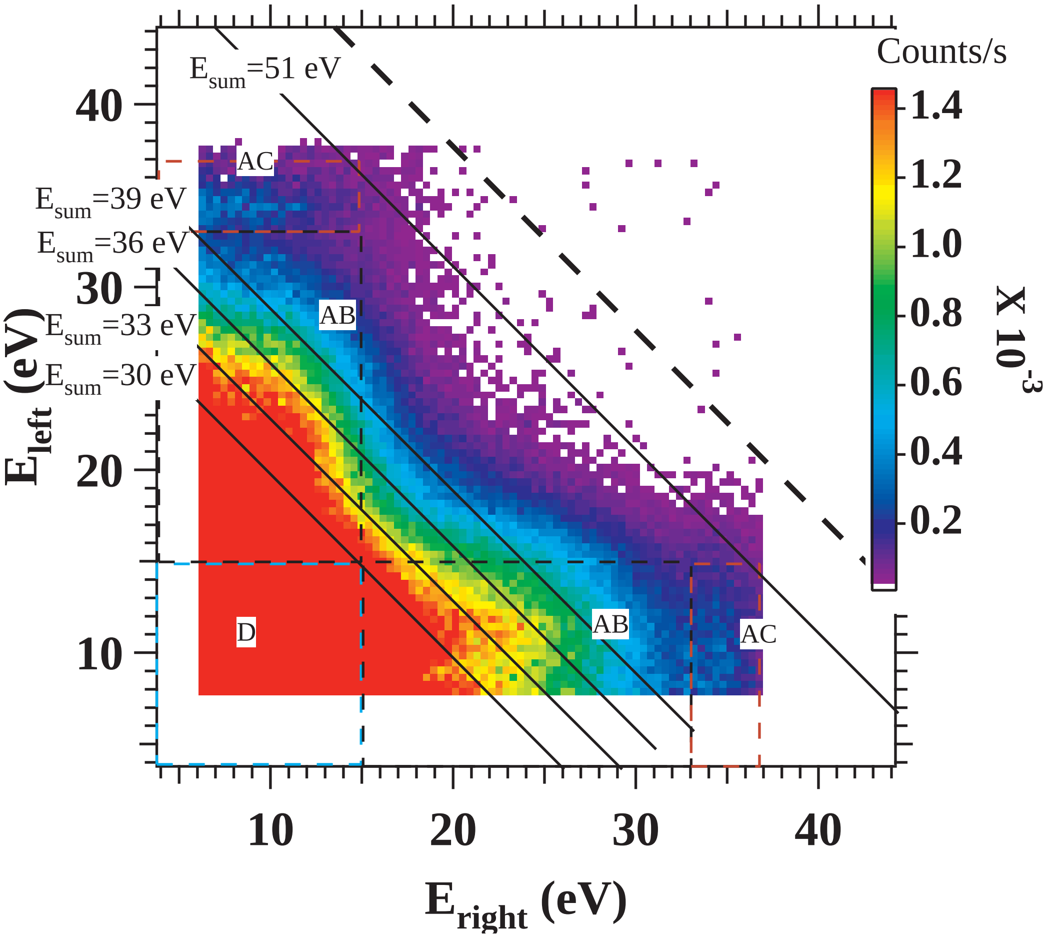

**Figure 4.10:** (Color) 2D-energy spectrum, merged from the four 2D-energy spectra in Fig. 4.9. The black, red, blue boxes label three regions “AB”, “AC” and “D”, corresponding to three mechanisms for the pair emission. The figure is overexposed to make the feature in the region “AC” be visible. The solid diagonal lines label the sum energies of two electron ($E_{sum}$), along which the sharing curves in Fig. 4.13 are obtained. See text for further details.

window (varying the mean kinetic energies $E_k$ of the two spectrometers) to study other 2D-energy regions. We present additional four 2D-energy spectra in Fig. 4.9, of which the mean kinetic energies of the two spectrometers are: $E_{k,left} = E_{k,right} = 25$ eV (Fig. 4.9(a)), $E_{k,left} = E_{k,right} = 25$ eV (Fig. 4.9(b)), $E_{k,left} = 25$ eV, $E_{k,right} = 21$ eV (Fig. 4.9(c)) and $E_{k,left} = 21$ eV, $E_{k,right} = 25$ eV (Fig. 4.9(d)). These four 2D-energy spectra are plotted in the same way as described for Fig. 4.7. We want to emphasize, these 2D-energy spectra were measured for the same ($\alpha$,2e) process, only the energy window of the spectrometer is different. It can be observed that these 2D-energy spectra are identical to each other. For example, they all display the same L-shaped region. From this point of view, it is possible to merge these 2D-energy spectra into one, to have a "larger" energy window.

In Fig. 4.10, we display the 2D-energy spectrum merged from the four 2D-energy spectra in Fig. 4.9. In the merged 2D-energy spectrum, we separate the "L" region into three regions: "AC", "AB" and "D", which are labeled by the red, black and blue boxes, respectively. In the region "AC", a feature around $E_{left}$ ($E_{right}$) = 35 eV can be observed. As explained in the $He^{2+}$ non-coincidence spectrum, the peak at 35 eV (feature C) is assigned to the KLL AI transition. In the sequential neutralization scheme, this transition is followed by AC(1,0). The two transitions and the RC prior to KLL AI together constitute a neutralization path, RC+KLL AI+AC(1,0), $He^{2+}+M \xrightarrow{RC} He^{**}(2l,2l')+M^{2+} \xrightarrow{KLL\ AI} He^{+}(1s)+M^{2+}+e_1 \xrightarrow{AC(1,0)} He^{0}+M^{4+}+e_2$. The energy of $e_1$ is around 35 eV, and the energy of $e_2$ is in the range 0-15 eV. The region "AB" corresponds to the neutralization path AC(2,0)+AC(1,0), $He^{2+}+M \xrightarrow{AC(2,0)} He^{+}(1s)+M^{2+}+e_1 \xrightarrow{AC(1,0)} He^{0}+M^{4+}+e_2$. The energy of $e_1$ is in the range 15-33 eV, and the energy of $e_2$ is in the range 0-15 eV. When an excited electron is propagating to the surface, this electron may collide with another valence electron, creating an electron pair. This is similar to a (e,2e) process, but the primary electron is from the inner, we call it an internal (e,2e) event. In this path, the energies of the two electrons are small, they contribute mainly in the region "D", which is located at the lower left-hand corner of the 2D-energy spectrum. We want to mention the boundary of these regions are not sharp, they can just give a rough idea how the electron pairs due to different mechanisms are distributed. Again, we want to emphasize the events outside these three regions can not be understood by the sequential neutralization model. They are non-sequential events.

For an electron pair, it is interesting to ask what is the energy distribution of one electron (free electron) by fixing the energy of the other one (fixed electron). Such a spectrum can be extracted from a 2D-energy spectrum. We call it line scan spectrum. **For two non-interacting electrons, obviously, the energy distribution of the free electron (line shape) is independent of the energy of the fixed electron**. Alternatively speaking, if the energy distribution of the free electron is dependent of the energy of the fixed electron, this is clear proof that the two electrons are correlated with other. In Fig. 4.11, we present the line scan spectra extracted from the 2D-energy spectrum in Fig. 4.10. We impose a constraint on the "right" electrons, $E_{right} = E_{fix}$ $\pm$ 1 eV, and plot the coincidence intensity as a function of the energy of the "left" electrons. $E_{fix}$ is the fixed energy. The coincidence spectra are normalized to let the intensity at $E_{left} = 7.7$ eV be the same. For comparison, the $He^{+}$ and $He^{2+}$ non-

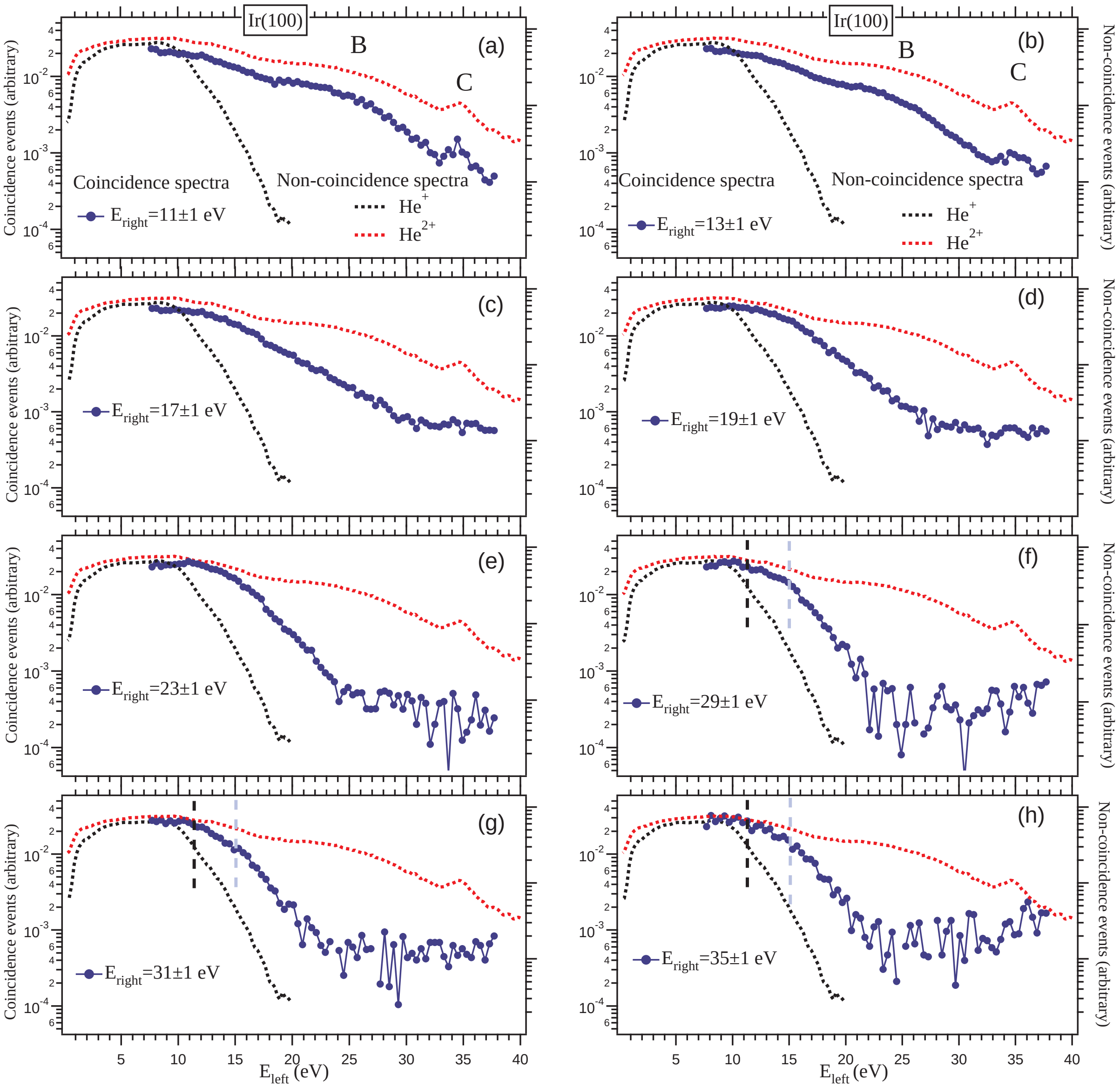

**Figure 4.11:** Electron energy spectra (coincidence) of the "left" electrons, by fixing their partner "right" electrons in the region $E_{right} \pm 1$ eV, which are extracted from the 2D-energy spectrum in Fig. 4.10. The coincidence spectra (arbitrary) are normalized to let the intensity at $E_{left} = 7.7$ eV be the same (needed for comparison). The black and red dotted curves represent the non-coincidence spectra by the primary $He^{+}$ and $He^{2+}$ ions, respectively. In (f-h), the black (11.26 eV) and blue (15 eV) dashed lines represent the high energy edges for the $He^{+}$ non-coincidence spectra and the coincidence spectra, respectively.

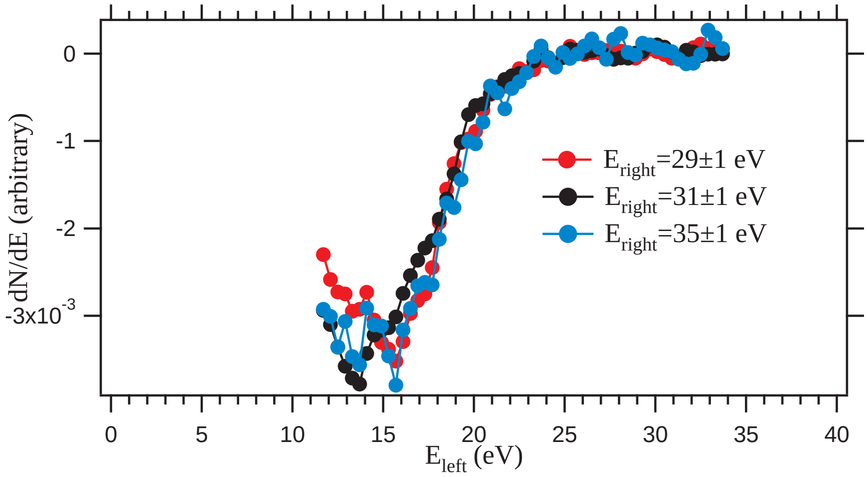

**Figure 4.12:** The derivative spectra of the line scan spectra $E_{left}$ = 29, 31 and 35 ± 1 eV in Fig. 4.11. They are calculated by the same way as described for Fig. 4.1(b).

coincidence spectra are included. They are the same as shown in Fig. 4.4. Both the left (coincidence) and right (non-coincidence) axis are plotted in logarithmic scales, with max/min = $10^3$.

First, let us focus on panels (a-b), $E_{fix}$ = 11-13 eV. In the line scan spectra, the features B (17-33 eV) and C (35 eV) can be observed. They are identical to the features in $He^{2+}$ non-coincidence spectrum. As for higher fixed energies, $E_{fix}$ = 17-35 eV (c-h), the features B and C can not be observed any more. This can be understood by the sequential neutralization scheme in Fig. 2.7. The features B (AC(2,0)) and C (KLL AI) belong to the first electron ($e_1$) emission process. They are followed by the transition AC(1,0), in which the second electron ($e_2$) is emitted. For these line scan spectra, when the fixed energy is in the range of the energy for $e_2$, 0-15 eV, the energy distribution of the free electron will reflect the features for $e_1$, i.e. AC(2,0) and KLL AI.

Then, pay attention to panels (f-h), $E_{fix}$ = 29-35 eV. The shape of these line scan spectra is similar. The intensity decreases slowly in the region $E_{left}$ = 8-15 eV. Above 15 eV, the intensity starts to decreases quickly. The shape is similar to the $He^+$ induced non-coincidence spectrum, except the high energy edge is shifted towards the high energy side. For the $He^+$ non-coincidence spectrum, the high energy edge is identified from the derivative curve, which is at 11.26 eV, indicated by the black dashed line. We employ the same method to identify the high energy edge of the coincidence spectra. We calculate the derivative for the line scan spectra, $E_{fix}$ = 29, 31 and 35 eV. The minimums of the derivative curves indicate that the high energy edge for the line scan spectra, $E_{fix}$ = 29-35 eV, is about 15 eV.

Last, pay attention to panels (c-e), $E_{fix}$ = 17-23 eV. In these line scan spectra, the features B and C can not be observed. This means the free electron can not be assigned to AC(2,0) or KLL AI. Their shapes are different from the $He^+$ non-coincidence spectrum. Therefore, the free electron can not be assigned to AC(1,0), either. Note, the shape varies with $E_{right}$. As announced, this indicates that the two electrons are correlated with each other. In other words, these spectra can not be understood by the sequential neutralization model.

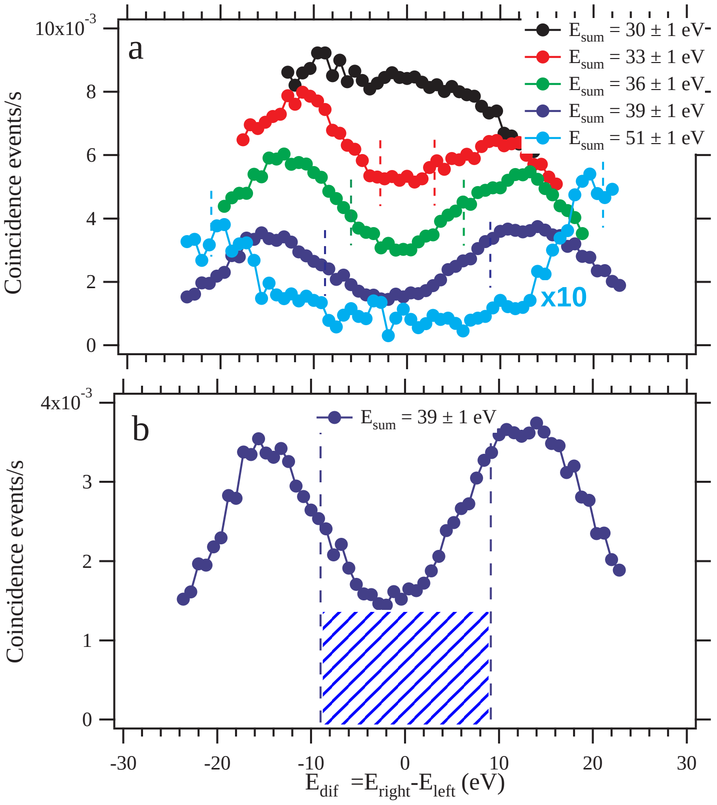

**Figure 4.13:** Energy sharing curves, for electron pairs with different sum energies ($E_{sum} \pm 1$ eV), which are extracted from the 2D-energy spectrum in Fig. 4.10. For a sharing curve, the two dashed lines label the region where the energies of the two electrons are both larger than 15 eV. In this region, the sequential events are not allowed. The shaded area in (b) is the assumed contribution from the non-sequential process.

The line scan spectra have provided an important information. In ($\alpha$,2e), when an electron pair is composed of a slow electron ($<$ 13 eV) and a fast electron ($>$ 29 eV), it is easy to distinguish that the slow electron is $e_2$, the fast electron is $e_1$. When an electron pair is composed of two electrons not fast and not slow (17-23 eV), it is difficult to distinguish which is $e_1/e_2$. In the 2D-energy spectrum, these events correspond to the region outside the “L” region.

For an electron pair, an important question is whether and how they share the available energy. For this question, a proper presentation is the so-called energy sharing curve. The energy sharing curve is the coincidence intensity as a function of the energy difference $E_{dif}$ for a given sum energy, $E_{sum}$. Fig. 4.13(a) shows the energy sharing curves, for selected values of $E_{sum}$ (30, 33, 36, 39, and 51 eV). They are extracted from the 2D-energy spectrum in Fig. 4.10, within the energy band $E_{sum} \pm 1$ eV. We want to mention that the experiment geometry is symmetric. The asymmetry of the sharing curve only reflects the difficulty to align the two spectrometers to be the same.

The sharing curve for $E_{sum} = 30$ eV is featureless. When the sum energy is increased by 3 eV ($E_{sum} = 33$ eV), the shape of the sharing curve changes dramatically. The shape of the sharing curves for $E_{sum} = 33$, 36, 39 eV is similar to each other. They display two broad peaks around $E_{dif}$ = -14 eV and 14 eV, and a minimum near the center, $E_{dif}$ = 0. See the 2D-energy spectrum in Fig. 4.10, the lines for $E_{sum}$ = 33, 36, 39 eV, go through the region "AB", which is for the AC(2,0)+AC(1,0) path. In the $He^{2+}$ non-coincidence spectrum shown in Fig. 4.4, the energy difference between the peaks for AC(2,0) (23 eV) and AC(1,0) (9 eV) is about 14 eV. Therefore, the two broad peaks (± 14 eV) are due to the AC(2,0)+AC(1,0) path. Since the line for $E_{sum}$ = 51 eV does not pass through the region "AB", the sharing curve for $E_{sum}$ = 51 eV does not display the two peaks.

The minimum near the center can be understood as follows. In the sequential path, the energies of the two electrons can not be higher than the highest value of $e_2$ (15 eV) at the same time. This requirement can be fulfilled for a sharing curve with $E_{sum} \leq$ 30 eV. While for an electron pair with a sum energy $E_{sum} >$ 30 eV, there is a region of the center, where the energies of the two electrons are both larger than 15 eV. This region is $|E_{dif}| < E_{sum}$ - 30 eV. Inside this region, the sequential events are forbidden. For the sharing curves $E_{sum}$ = 33, 36, 39 eV, these regions are indicated by pairs of dashed lines in Fig. 4.13(a). As $E_{sum}$ increases, this region grows larger. Since the sequential path is forbidden in this region, the intensity in this region originates from the non-sequential process. See the sharing curve $E_{sum}$ = 51 eV, which is basically flat near the center. This indicates the energy sharing distribution for non-sequential process is almost constant for $E_{dif}$. This is different from the sequential model, which prefers a very unequal energy sharing.

We want to estimate the relative contribution of the non-sequential path. Pay attention to the sharing curve $E_{sum}$ = 39 eV in the lower panel. It has been just discussed that the events between the two dashed lines are mainly from the non-sequential process. However, the distribution of the non-sequential events outside this region is unknown. A conservative estimation is that the non-sequential events are confined between the two dashed line, indicated by the dashed area. In this case, the relative contribution of the non-sequential path is about 20%. We employ the same method for the sharing cures $E_{sum}$ = 33, 36 eV, the numerical results are 13%, and 20%, respectively. Hence, it is clear that the non-sequential process is not a trivial process in ($\alpha$,2e).

## 4.3 Coincidence spectra of Fe(100)-p(1×1)O

The ($\alpha$,2e) experiments on the O/Fe(100) surface were performed in the same way as described for the Ir(100). Fig. 4.14 shows the time histogram of the ($\alpha$,2e) events from O/Fe(100), with the two spectrometers being set to $E_k$ = 19 eV and $E_{pass}$ = 300 eV. A peak based on a constant background can be observed. The peak and the constant background are attributed to true and random coincidences, respectively. The coincidence count rate, single count rate and the true/random ratio of the experiment are listed in Tab. 4.1. In comparison to Ir(100), the single count rates are the same. However, the coincidence count rate and the true/random ratio of O/Fe(100) are lower. We will come back to this issue later.

The inset of Fig. 4.14 shows the time histogram obtained by the collision of 5 eV normal incident $He^+$ ions. The two spectrometers were set to $E_k$ = 6 eV and $E_{pass}$ = 100 eV. The single count rate is about 4000 cps, close to that for the primary

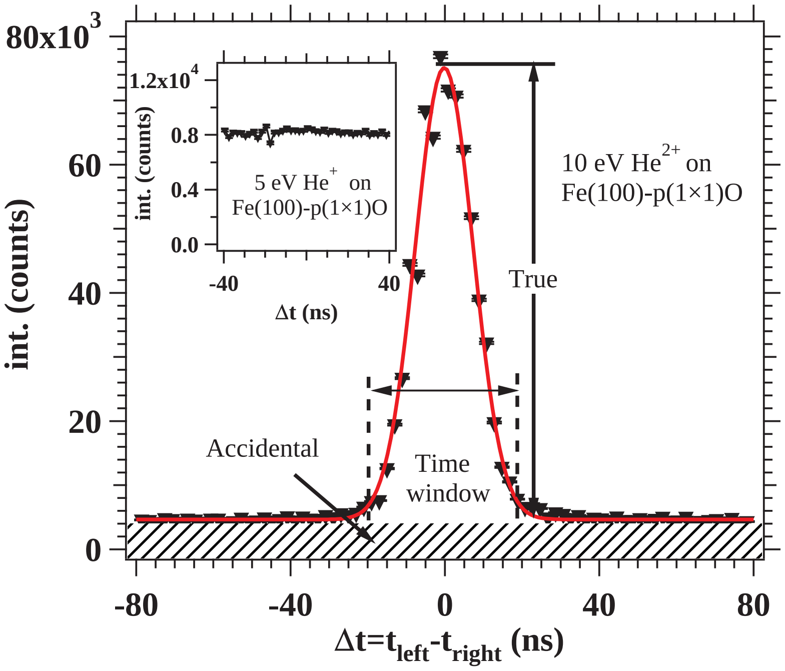

**Figure 4.14:** Time difference histogram (solid triangles) of the ($\alpha$,2e) events excited by the collision of 10 eV $He^{2+}$ onto O/Fe(100), using the same experimental conditions as for Fig. 4.6.

$He^{2+}$. Similar to the observation for Ir(100) (see the inset of Fig. 4.6), there is no peak in the spectrum. The detected electron pairs are dominantly contributed by random coincidences. This confirms the previous conclusion that the pair emission by primary $He^{+}$ can be negligible compared to that by primary $He^{2+}$.

**Table 4.1:** List of the coincidence count rate $r_c$, single count rate $r_s$, true/random ratio for Ir(100) and O/Fe(100) with the same settings of $E_k$ = 19 eV and $E_{pass}$ = 300 eV.

| Sample | $r_c$ (cps) | $r_s$ (cps) | true/random |
|---|---|---|---|
| Ir(100) | 5.8 | 3500 | 14 |
| O/Fe(100) | 3 | 3500 | 8 |

Fig. 4.15(a) shows the 2D-energy spectrum, with the spectrometer being set to $E_k$ = 19 eV. The red lines at 11 eV (highest energy for $e_2$) and 37 eV (highest energy for $e_1$) define a “L” region, which is expected by the sequential model. Similar with Ir(100), the ($\alpha$,2e) events from O/Fe(100) are mainly distributed in this “L” region. Note, there are also events outside the region, where the energies of the two electrons are both higher than the highest energy of $e_2$, 11 eV. These events are not allowed by the sequential model. To clarify the origin of these events, we move the energy window to a higher kinetic energy region. See the 2D-energy spectrum shown in the right panel, with the two spectrometers being set to $E_k$ = 25 eV. In this case, the energy window is totally outside the “L” region, and similar with the case of Ir(100), the 2D-energy spectrum dose not display the “L” shaped distribution. This proves that in this 2D-energy region,

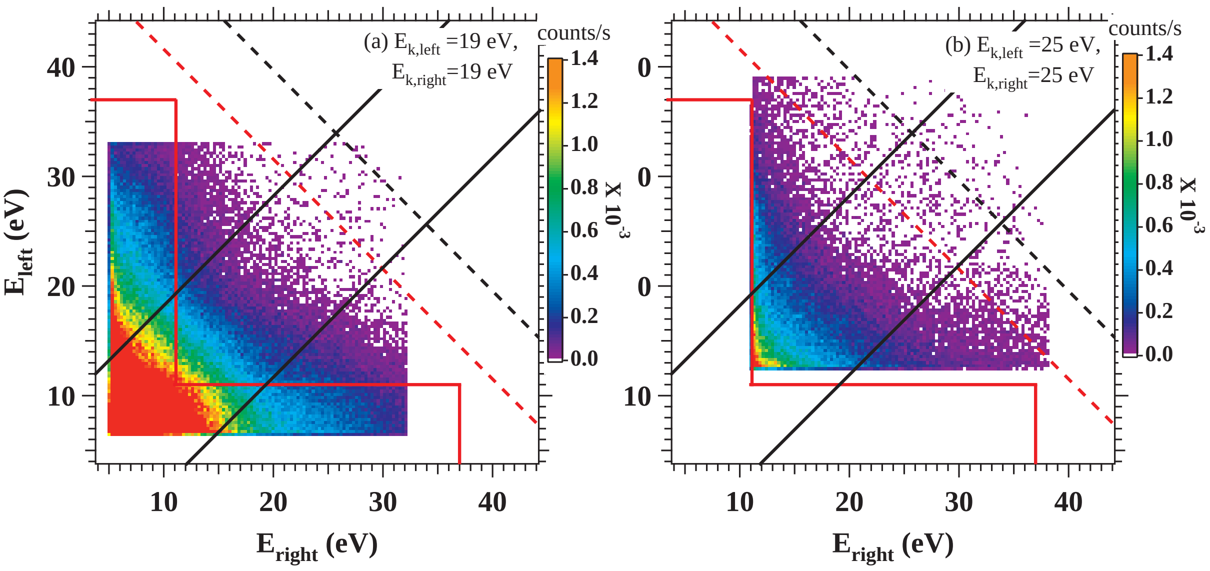

**Figure 4.15:** (Color) 2D-energy spectra, similar to Fig. 4.7, but for O/Fe(100). (a) $E_k$ = 19 eV, (b) $E_k$ = 25 eV. The dashed lines label the sum energies, when the four valence electrons are taken from the Fermi edge (black) and the Fe 3d band (red), respectively. The pairs of black solid lines define the region $E_{dif}$ = ± 8 eV, from which the sum energy spectrum (Fig. 4.16(a)) is obtained. The red solid lines label the "L" region, which is expected by the sequential neutralization model.

the energies of two electrons are not well separated in two different energy ranges.

It has been discussed that, for the $He^+$ non-coincidence spectrum with O/Fe(100) (see Fig. 4.5), the highest energy of AC corresponds to the situation when the two valence electrons are taken from the Fe 3d band, instead of the Fermi level. This is because the SDOS of the occupied states above the Fe 3d band is low. For $E_{sum}^{max}$, we also have to pay attention to this point. In Figs. 4.15(a) and (b), we draw a red dashed line and a black dashed line, which represents, respectively, two situations for $E_{sum}$: when the four valence electrons are taken from the 3d band, or from the Fermi level. The numerical results (from Eq. 4.1) are 51.4 eV (3d band, 2 eV below the Fermi level) and 59.4 eV (the Fermi level, $W = 4.9$ eV). The intensity near the red dashed line is higher than that near the black dashed line. However, it is not easy to determine which line represents the maximum sum energy from the 2D spectra directly. This point can be clarified in the sum energy spectrum, see Fig. 4.16.

We check the $E_{sum}^{max}$ for the ($\alpha$,2e) from O/Fe(100) in the near equal energy region. Fig. 4.16(a) shows two sum energy spectra, which are obtained by integrating the intensity, with the constraint, $E_{dif} = \pm$ 8 eV, in Figs. 4.15(a) and (b). The two curves are in agreement with each other. The sum energy spectra behave analogously to that of Ir(100) (see Fig. 4.8). The intensity is decreased nearly exponentially with increasing the sum energy, which drops roughly three orders of magnitude from $E_{sum} = 20$ eV to $E_{sum} = 50$ eV. The red (51.4 eV) and black (59.4 eV) dashed line are consistent with the ones in Fig. 4.15. Around the red dashed line, the intensity decrease nearly one order of magnitude. Therefore, it is the red dashed line that represents the onset of the pair emission.

Fig. 4.16(b) shows the time histograms for the events in two energy regions: $E_{sum} = 47 \pm 2$ eV and $E_{dif} = \pm$ 8 eV (black), and $E_{sum} = 54 \pm 2$ eV and $E_{dif} = \pm$ 8 eV (blue). These two regions are chosen such that they are located just below and above the red dashed line. For the black curve, a peak due to the true coincidence events can be observed, with true/random ratio being 0.42. By contrast, for the blue curve, no peak can be observed, which indicates no true coincidences. Similar with Ir(100), Figs. 4.16(a) and (b) indicate that the true coincidence events can be found up to the maximum sum energy provided by the ionization potential of the $He^{2+} \rightarrow He^0$ (79 eV). A situation different with Ir(100) is that the four electrons originate from the Fe 3d band instead of the Fermi level, which is due to the special electronic structure of the O/Fe(100). It should be noticed that, the sum energy spectra are obtained in the region where the energy of the two electrons are nearly equal ($\pm$ 8 eV). Therefore, for the same reason as for Ir(100), the arguments of broadening effect and the kinetic energy of the ions can be ruled out.

Return back to issue of the coincidence count rates for Ir(100) and O/Fe(100). The $E_{sum}^{max}$ for O/Fe(100) (51.4 eV) is lower than that for Ir(100) (56.32 eV). For the same 2D-energy window, this can make the effective detecting area for O/Fe(100) to be smaller than that for Ir(100). In other words, the intensity between $E_{sum} = 51.4$ eV and 56.32 eV is zero for O/Fe(100), but nonzero for Ir(100). This can help to understand why the coincidence count rate for O/Fe(100) is lower than for Ir(100).

Fig. 4.17 shows three additional 2D-energy spectra, for the same ($\alpha$,2e) experiment with the O/Fe(100) surface, but for different 2D-energy regions (the kinetic energies of the two spectrometers are different): $E_{k,left} = E_{k,right} = 21$ eV (Fig. 4.17(a)), $E_{k,left} = 21$

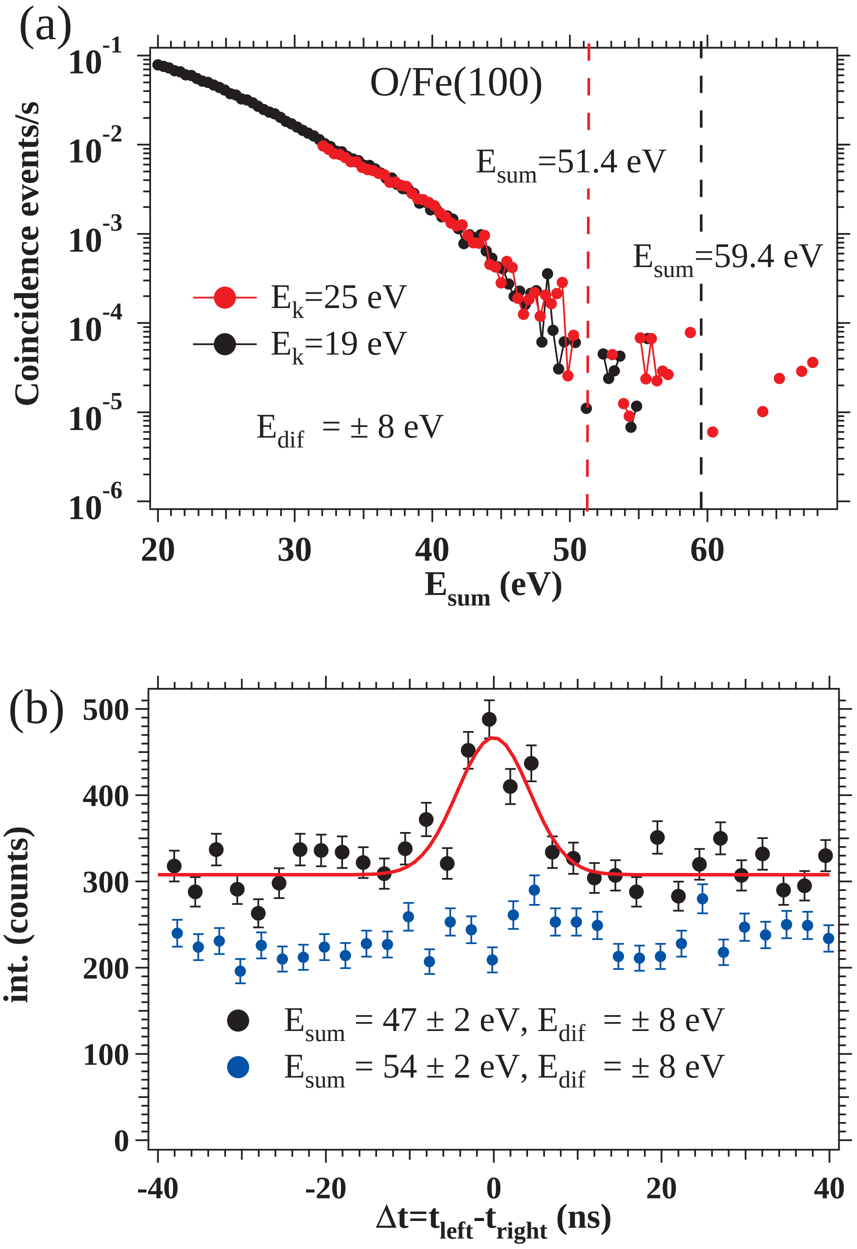

**Figure 4.16:** Similar with Fig. 4.8. (a) Sum energy spectra with the constraint, $|E_{left} - E_{right}| < 8$ eV, which are extracted from the 2D-energy spectra in Figs. 4.15(a) and (b). (b) Time histograms for the events: $E_{sum} = 47 \pm 2$ eV and $E_{dif} = \pm\ 8$ eV (black), and $E_{sum} = 54 \pm 2$ eV and $E_{dif} = \pm\ 8$ eV (blue). The electron pairs are obtained from the ($\alpha$,2e) experiment with $E_k = 25$ eV.

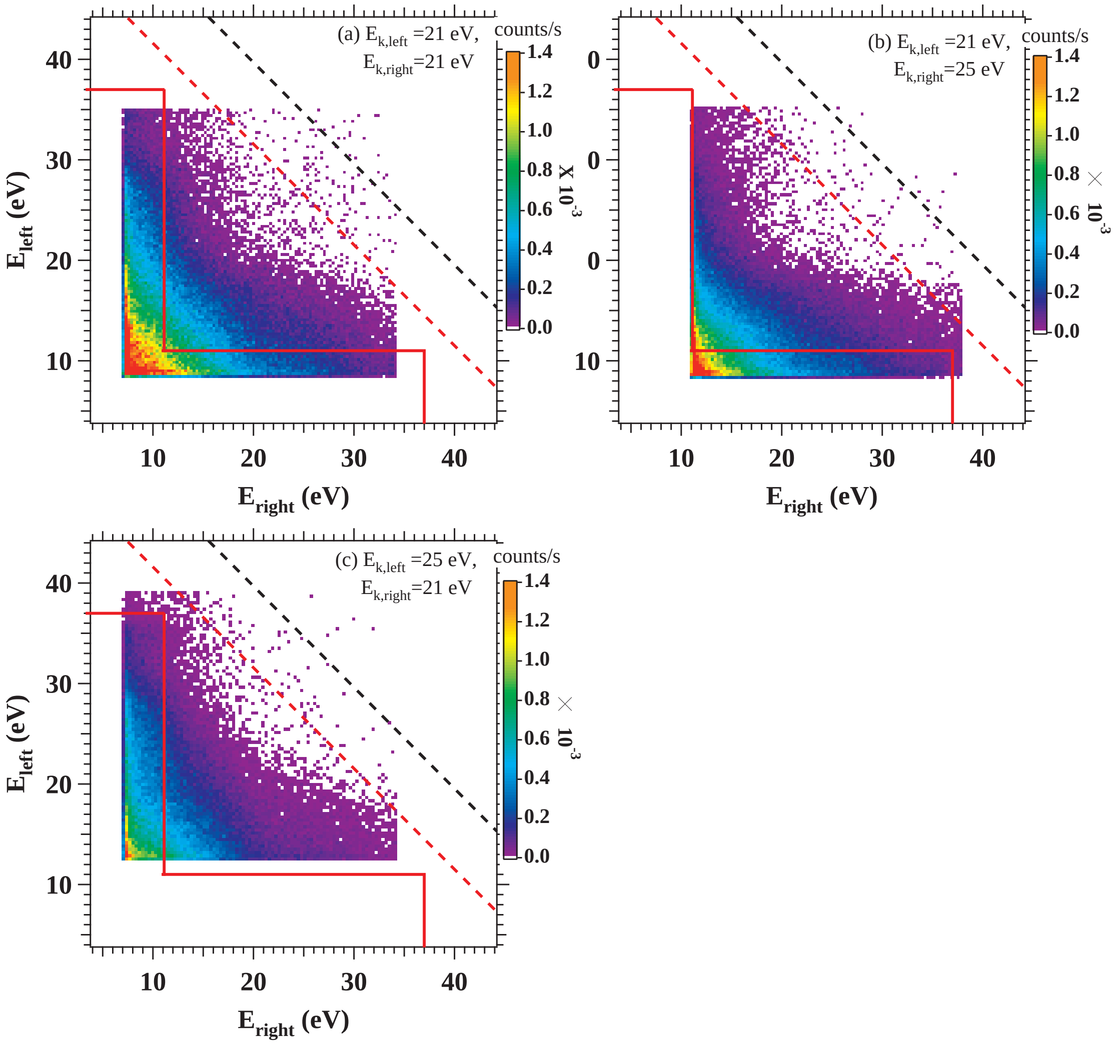

**Figure 4.17:** (Color) 2D-energy spectra of the ($\alpha$,2e) experiment, similar with Fig. 4.9, but for O/Fe(100), (a) $E_{k,left} = E_{k,right} = 21$ eV, (c) $E_{k,left} = 25$ eV, $E_{k,right} = 21$ eV and (d) $E_{k,left} = 21$ eV, $E_{k,right} = 25$ eV. The solid and dashed lines are consistent with the Fig. 4.15.

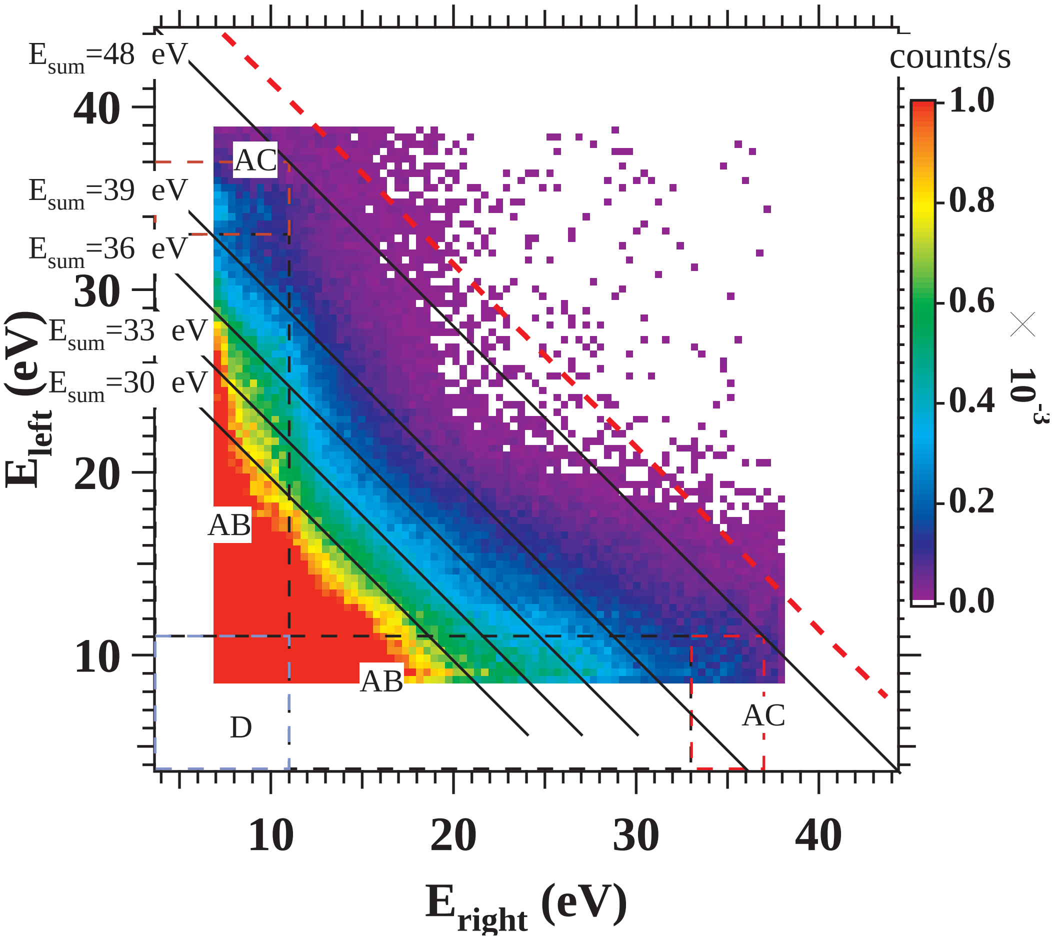

**Figure 4.18:** (Color) 2D-energy spectrum, merged from the three ones in Fig. 4.17. Similar with Fig. 4.10.

eV, $E_{k,right} = 25$ eV (Fig. 4.17(b)) and $E_{k,left} = 52$ eV, $E_{k,right} = 21$ eV (Fig. 4.17(c)). Since the three 2D spectra are in agreement with each other, we can merge them into one in order to get a larger 2D-energy spectrum. This is shown in Fig. 4.17. As described for Fig. 4.10, in Fig. 4.17, we separate the "L" region into three small ones: "AB", "AC" and "D". They correspond to three mechanisms for the electron pair emission, respectively, AC(2,0)+AC(1,0), RC+KLL AI+AC(1,0), and internal (e,2e).

Fig. 4.19 shows the line scan spectra. The energy of the "left" electrons are free, while the energy of the "right" electrons are fixed at 9-37 eV (a-h). The black ($He^+$) and red ($He^{2+}$) dashed lines are the non-coincidence spectra for O/Fe(100), which are displayed for comparison. All the spectra are presented in the same way as described for Fig. 4.11. The line scan spectra $E_{fix}$ = 9-11 eV (a-b) can be classified into one type, in which the features B (AC(2,0)) and C (KLL AI) can be observed. The line scan spectra $E_{fix}$ = 27-37 eV (f-h) are classified into another type. The shape of these spectra is identical to each other. They are also similar to the $He^+$ induced spectra,

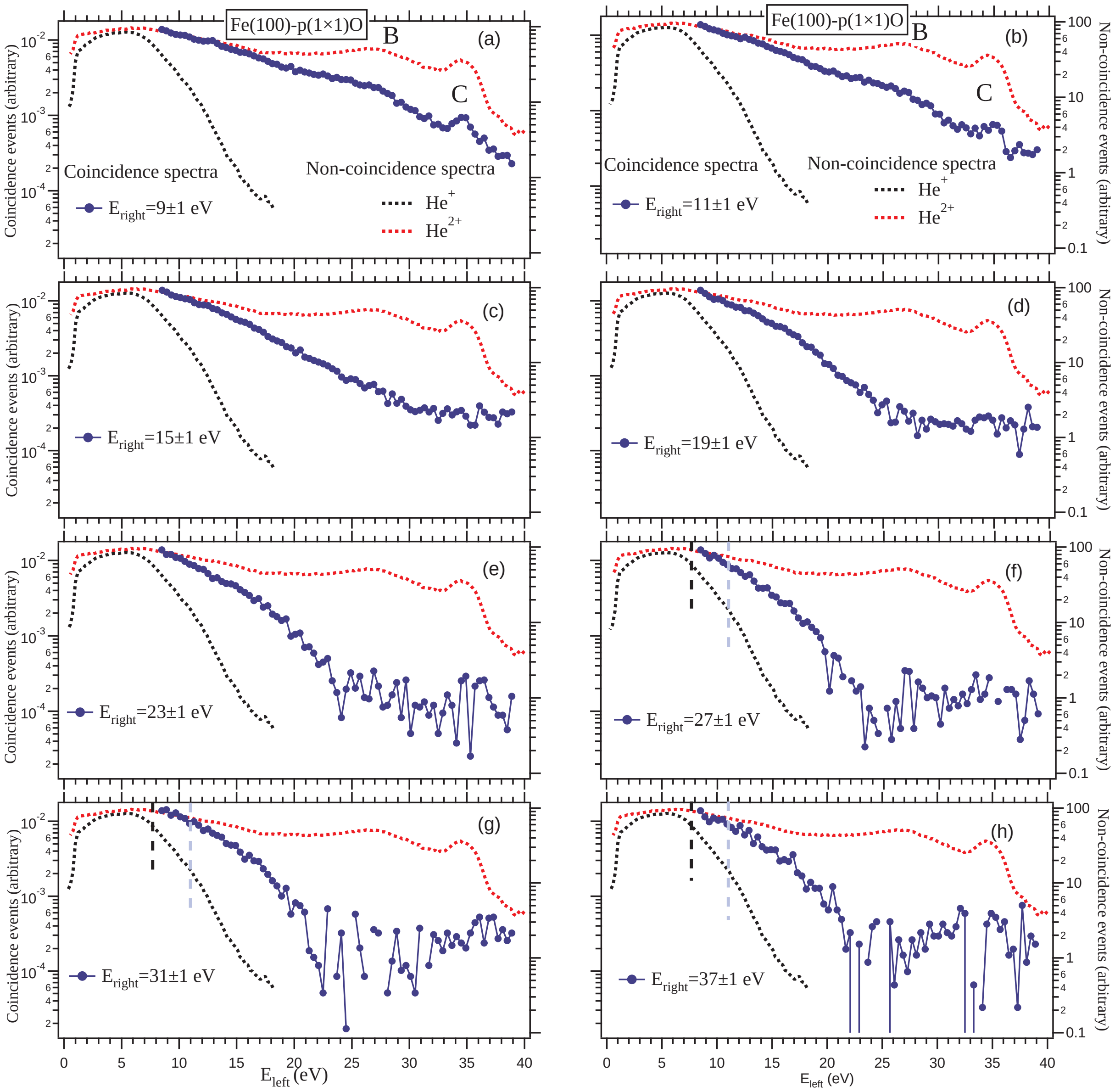

**Figure 4.19:** Line scan spectra of $E_{left}$, by fixing the energy of the "right" electrons. Similar with Fig. 4.11, but for O/Fe(100).

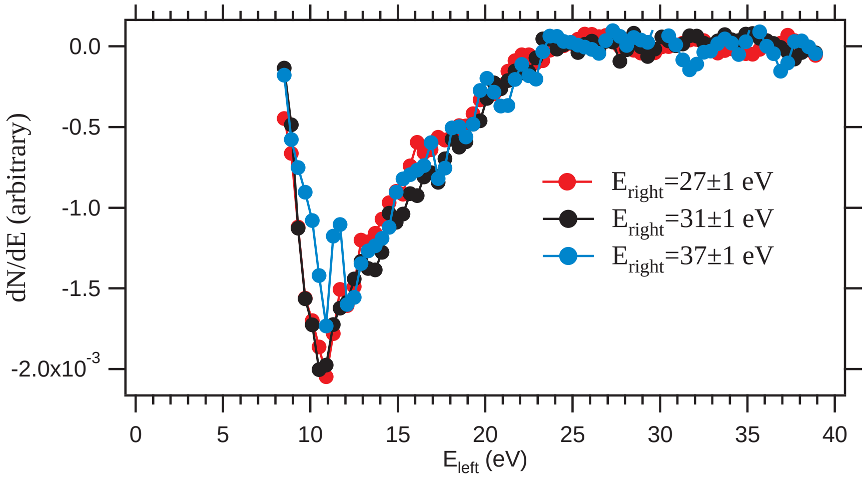

**Figure 4.20:** The derivative of the line scan spectra $E_{left}$ = 29, 33 and 37 ± 1 eV in Fig. 4.19. They are calculated by the same way as described for Fig. 4.1(b).

except obviously, the high energy edge is shifted towards the high energy side. In order to identify the high energy edge, we plot the derivative curves, shown in Fig. 4.20. The minimums of the derivative curves show that the high energy edge of the line scan spectra $E_{fix}$ = 27-37 eV (f-h) is at 11 eV. These two types of line scan spectra can be explained by the sequential neutralization model. When one electron is fixed in the low ($\leq$ 11 eV)/high ($\geq$27 eV) energy range, the energy distribution of the other electron in the high/low energy range, reflects the first/second electron emission process, respectively.

Now pay attention to the line scan spectra $E_{fix}$ = 15, 19 and 23 eV, panels (c-e). In these spectra are the features B and C can not be observed, and they are different from the $He^+$ non-coincidence spectrum. The variation of the line shape with $E_{fix}$ indicates that the two electrons are correlated with each other. In other words, if the two electrons are both in the middle energy range, it is impossible to distinguish which electron is $e_1/e_2$. These observations are all similar with the case of Ir(100).

Fig. 4.21 shows the energy sharing curves ($E_{sum}$ ± 1 eV), which are extracted from the 2D-energy spectrum in Fig. 4.18. We selected the values of $E_{sum}$ = 30, 33, 36, 39, and 48 eV. They are presented by the same way as described for Fig. 4.13. For these sharing curves, the intensity in the center is lower than the two sides. The explanation is the same as for the case of Ir(100), the region in the center, $|E_{dif}| < E_{sum}$ - 22 eV, is "forbidden" by the sequential neutralization model. Because, in this region, the energies of the two electrons are both larger than the highest energy of $e_2$. The intensity in this region is contributed by the non-sequential process.

See the 2D-energy spectrum in Fig. 4.18, the lines for $E_{sum}$ = 30, 33, 36 and 39 eV, go through the region "AB", which is for the AC(2,0)+AC(1,0) path. However, the corresponding sharing curves do not show the feature of two broad peaks, as for the case of Ir(100). In the $He^{2+}$ non-coincidence spectrum shown in Fig. 4.5, the energy difference between the peaks for AC(2,0) (27 eV) and AC(1,0) (6 eV) is about 21 eV. Hence, two broad peaks are expected at $E_{dif}$ = ± 21 eV. The range of $E_{dif}$ is limited by the size of the energy window. The longest range of $E_{dif}$ is from -21 eV to 21

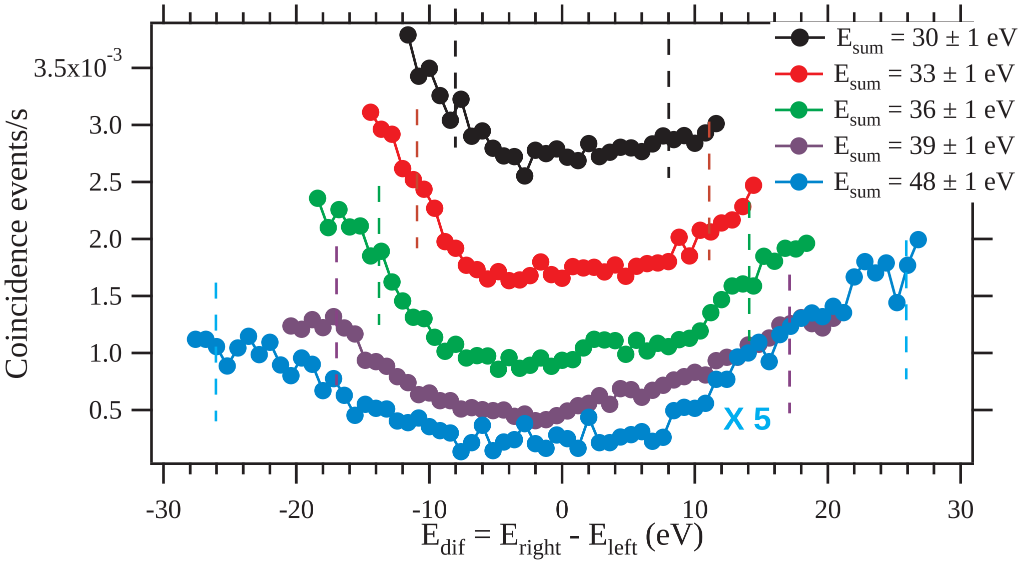

**Figure 4.21:** Energy sharing curves for $E_{sum}$ = 30, 33, 36, 39 and 48 ± 1 eV, similar to Fig. 4.21. They are extracted from Fig. 4.18.

eV, for the sharing curve $E_{sum} = 39$ eV. Our energy window is not large enough to cover the main contribution of the AC(2,0)+AC(1,0) path (the expected two broad peaks). Lack of the main contribution of the sequential path (AC(2,0)+AC(1,0)), in this case it is impossible to estimate the relative contribution of the non-sequential path. However, since the intensity in the "forbidden" region is comparable to the intensity outside this region, it is clear that the non-sequential process is not a trivial process for He$^{2+}$-O/Fe(100).

# Chapter 5

# Discussion

In the ($\alpha$,2e) experiments, we have found the events can be understood by the sequential neutralization model. However, we have also provided the evidence of the events, which can only be understood by a non-sequential process. As introduced in Sec. 2.1.5, the neutralization of He$^{2+}$ can follow different paths, see Fig. 2.7. This gives a hint that, for some paths the sequential description is applicable, for some paths it is not applicable. Similar sequential emission models are used in the description of other processes, for example, the Auger decay after photo-excitation, and the two-photon double ionization of He. In Sec. 2.2, we have discussed, from a general point of view, the applicability of the sequential models. The point is that, the time interval between two successive emissions should be sufficiently long to reach a **stationary** state, i.e. a well defined intermediate state. Before we discuss the applicability/inapplicability of the sequential neutralization model, it is advantageous to discuss the scenario of the ($\alpha$,2e) process first.

We present in Fig. 5.1 the schematic depiction of the neutralization of He$^{2+}$ in front of a metal surface. The ion is moving towards the normal surface direction. We consider two typical sequential neutralization paths: AC(2,0)+AC(1,0) (left panel) and RC+KLL AI+AC(1,0) (right panel). In total, four electrons are involved: $e_1$ and $e_1^i$ are for the first electron emission step, $e_2$ and $e_2^i$ are for the second one. The electrons $e_1^i$ and $e_2^i$ are finally transferred to the He-1s orbital, while the electrons $e_1$ and $e_2$ are finally emitted to the vacuum. Since both the ion neutralization and the electron pair emission are surface sensitive, it is most likely that the four electrons originate from the topmost layer.

First, we discuss the path AC(2,0)+AC(1,0). In an AC transition, two valence electrons interact with each other, leading to one electron being captured by the ion, one electron being emitted to the vacuum. This is similar to an Auger decay. The interaction between the two valence electrons can be described by the Thomas-Fermi approximation, $U \propto \exp(-q_{TF}r)/r$, where $q_{TF}$ is the screening length, $r$ is the distance between the two electrons. In the topmost layer, $q_{TF}$ is estimated to be 0.1 a.u.. This is smaller than the value for bulk, 1 a.u. [12]. The transition rate of AC is proportional to $U$. This means that, the distance between the two electrons is most likely less than 10 a.u. (5.29 Å). Since the He$^{2+}$ is moving towards the surface normal, we estimate the four valence electrons are initially distributed in a small area with a radius of 5 a.u., in the topmost layer, just below the ion, see the gray area in Fig. 5.1. In Sec. 2.1.1, we

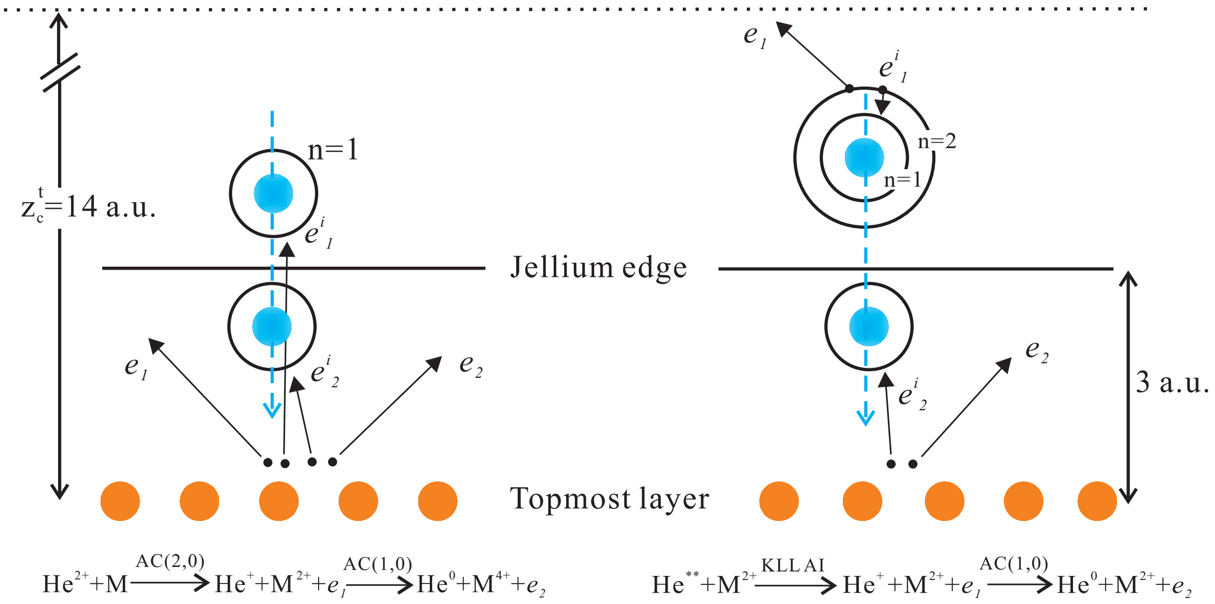
$z_c^t$=14 a.u.
n=1
$e_1^i$
Jellium edge
$e_1$
$e_2^i$
$e_2$
$e_1$
$e_1^i$
n=2
n=1
$e_2$
$e_2^i$
3 a.u.
Topmost layer
$He^{2+}+M \xrightarrow{AC(2,0)} He^{+}+M^{2+}+e_1 \xrightarrow{AC(1,0)} He^{0}+M^{4+}+e_2$
$He^{**}+M^{2+} \xrightarrow{KLL\,AI} He^{+}+M^{2+}+e_1 \xrightarrow{AC(1,0)} He^{0}+M^{2+}+e_2$

**Figure 5.1:** Schematic depiction of the sequential neutralization of $He^{2+}$ in front of a metal surface. The dashed arrows represent the trajectories of the ion. Electrons $e_1$ and $e_1^i$ are involved in the first electron emission step, and electrons $e_2$ and $e_2^i$ are involved in the second electron emission step. The four electrons originate most likely from the top most layer, in a small area (gray) just below the ion, with a radius of 5 a.u.. Left panel: AC(2,0)+AC(1,0); right: RC+KLL AI+AC(1,0). The black dashed line labels the critical neutralization distance, $z_c^t = 14$ a.u., which is derived from the COB model, see Sec. 2.1.1. The first/second step takes place most likely above/below the jellium edge.

have calculated that the upper time limit for the neutralization process of 10 eV $He^{2+}$ is 27 fs. In other words, the time interval ($t_{12}$) between the two electron emissions should be less than 27 fs. In the part of non-coincidence spectra, we have estimated that the most likely position for AC(2,0) is above the jellium edge. Later, we will further prove that the most likely position for AC(1,0) is below the jellium edge.

For the RC+KLL AI+AC(1,0) path, we recognize three steps. In the first step, two valence electrons ($e_1$ and $e_1^i$) are resonantly captured into the $n = 2$ atomic shell. According to the COB model, the resonant capture occurs when the ion reaches the critical distance, see the dashed line in Fig. 5.1. In this process, no electron is emitted, and we can focus on the following two steps, i.e. KLL AI and AC(1,0). In this case, the upper bound of 27 fs for the time interval between the two electron emission steps is also applicable here. One difference should be noticed, in the case of AC(2,0)+AC(1,0), the two electrons ($e_1$ and $e_2$) are both emitted from the surface. In this path, the first electron ($e_1$) is emitted from the ion, the second electron ($e_2$) is emitted from the surface.

The idea of the sequential model is that, two successive transitions are well separated by a well defined intermediate state, thereby, the two emitted electrons can be treated as two non-interacting particles. More specifically, in the above two sequential paths, only the electron-electron interactions between $e_1$ and $e_1^i$, and $e_2$ and $e_2^i$ have been considered.

While the interactions of electrons involved in different emissions, for example, $e_1$ and $e_2$, and $e_1^i$ and $e_2^i$, are assumed to be negligible. This could be reasonable for the RC+KLL AI+AC(1,0) path, because, the two emissions occur at different systems, i.e. the ion (KLL AI) and the surface (AC(1,0)). In addition, the electrons $e_1$ and $e_2$, or $e_1^i$ and $e_2^i$ are initially well separated in real space, thus the interaction between them is small.

However, this assumption is doubtful for the AC(2,0)+AC(1,0) path. Since the four electrons are all emitted/captured from the same system (surface), and they originate from a small area (the gray area in Fig. 5.1), it is highly possible that, during the neutralization, the electrons involved in different emissions can interact with each other. We propose four possible mechanisms. In this case, since four electrons are involved, it is a complicated many-body problem. In order to simplify, we only consider the interaction between the two captured electrons ($e_1^i$ and $e_2^i$), and the interaction between the two emitted electrons ($e_1$ and $e_2$).

(i) The interaction between $e_1^i$ and $e_2^i$ during the capture, see Sec. 2.2.4. In the sequential description, the second electron ($e_2^i$) capture occurs after the first electron ($e_1^i$) has arrived at the ion from the surface. If when the second electron capture occurs, the first electron is still in the path, from the point view of the second electron, the ion has not been completely screened by the first electron, and the ion is not in a stationary state. In other words, the second capture can not be simply understood by the transition, $\mathrm{He}^+ + e_2^i \rightarrow \mathrm{He}^0$. When the two electrons are both in the path, since the path is less than 14 a.u., the two electrons can interact with each other, for example by Coulomb interaction, during the path. We consider that the $\mathrm{He}^{2+}$ is located at the most likely position for AC(2,0), $z = 1.3$ a.u.. for Ir(100), and 1.9 a.u. for O/Fe(100). The velocity of a valence electron in surface is in the range, $0 \leq v(r_{t=0}) \leq v_{fe}$, where $v_{fe}$ is the Fermi velocity. A typical value for the Fermi velocity of a metal surface is about 0.5 a.u. (10.9 Å/fs) [78]. For a valence electron with the Fermi velocity, the travel time is, $t_{tra} \geq 6.6$ a.u. (0.16 fs) and 9.8 a.u. (0.24 fs). This provides a lower limit for the timescale of this interaction, about 0.2 fs.

(ii) Quantum interference between different paths. After $e_1^i$ has arrived at the ion, there is a probability for this electron to occupy the $n = 1$ level ($\mathrm{He}^+$(1s)), or the $n = 2$ level ($\mathrm{He}^{+*}$(2s)). We have introduced in Sec. 2.2.3, if there is more than one available intermediate state between two successive transitions, the lifetime broadening of the intermediate sates should be smaller than the energy separation between these intermediate states. Otherwise, the quantum interference between the different paths (i.e. via different intermediate states) should be considered. In ($\alpha$,2e), it requires that, $t_{life} \geq \hbar/|(E_b(\mathrm{He}^{+*}(2s))$ - $E_b(\mathrm{He}^{+}(1s))| \approx 16$ as, where $t_{life}$ is the lifetime of the intermediate state. The binding energies, $E_b(\mathrm{He}^{+*}(2s)) =$ -13.6 eV and $E_b(\mathrm{He}^{+}(1s)) =$ -24.6 eV are taken for free He.

(iii) The interaction of $e_1$ and $e_2$ in the continuum. If when $e_2$ is emitted, $e_1$ is still in the vicinity of the surface, the two electrons can interact each other in the continuum and exchange an amount of energy. This has been introduced in Sec. 2.2.1. We arbitrarily define that, when the exchange energy is smaller than 2 eV, the sequential description is a good approximation. The energy range of $e_1$ is in the range of 10-40 eV. Then, the timescale of this interaction is about 0.2-0.3 fs.

(iv) Dynamic screening, see Sec. 2.2.2. After the two electrons ($e_1$ and $e_1^i$) are

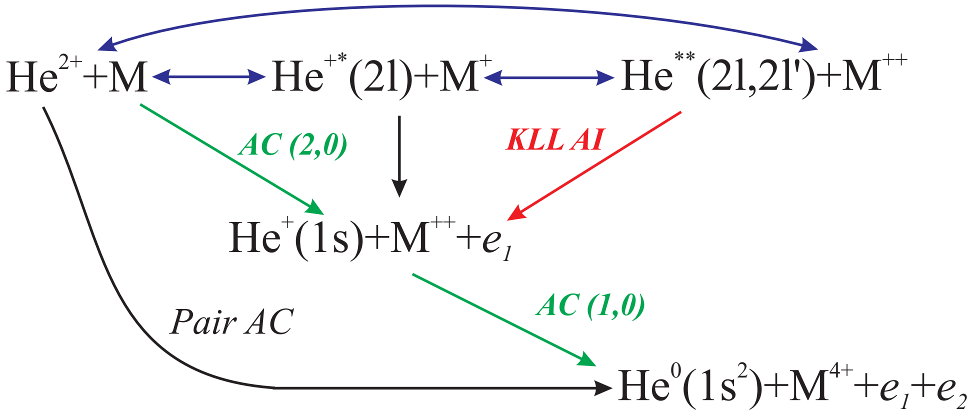

**Figure 5.2:** Proposed neutralization scheme, which focuses on the processes observed in the energy distributions.

removed from the surface, two holes with two positive charges are left. The existence of the two holes can alter the potential seen by the surrounding electrons (including $e_2$ and $e_2^i$), they will react to screen the two holes. For a metal surface, the timescale of the screening can be roughly estimated by, $t_{sc} = 1/\omega_s$ [74], where $\omega_s$ is the surface plasmon frequency. For Ir(100) and O/Fe(100), $\hbar\omega_s = 7.2$ eV [92] and 10.5 eV [93, 94], respectively, with the screening time being 0.09 fs and 0.06 fs. If the second emission takes place before the screening is finished, the electrons $e_2$ and $e_2^i$ are still in the dynamic screening process. In this case, the assumed well defined $M^{2+}$ state does not exist, and the sequential description is inappropriate.

Come back to the experimental data. To explain the data, we suggest a new neutralization scheme shown in Fig. 5.2. For simplicity, we only keep the processes which can be assigned in the non-coincidence and coincidence spectra, AC(1,0) (feature A), AC(2,0) (feature B) and KLL AI (feature C). Additionally, to understand the non-sequential events, a pair AC process is added. More details are described in the following.

(i) RC+KLL AI+AC(2,0),

$$He^{2+} + M \xrightarrow{RC} He^{**}(2l, 2l') + M^{2+} \xrightarrow{KLL\ AI} He^{+}(1s) + M^{2+} + e_1 \xrightarrow{AC(1,0)} He^0 + M^{4+} + e_2.$$

In the non-coincidence spectra, see Figs. 4.4 and 4.5, the features C (KLL AI) and A (AC(1,0)) belong to this path. In the coincidence 2D-energy spectra, this path can be observed in the region “AC”, see Figs. 4.10 and 4.18.

The sequential description is applicable in this path. The evidence are the following. First, In the line scan spectra, see Figs. 4.11 and 4.19, the energy of the feature C (KLL AI) is independent of $E_{fix}$. Second, The feature B (AC(2,0)) can only be clearly observed when $E_{fix}$ is in the energy range of the feature A (AC(1,0)).

(ii) AC(2,0)+AC(1,0),

$$He^{2+} + M \xrightarrow{AC(2,0)} He^{+}(1s) + M^{2+} + e_1 \xrightarrow{AC(1,0)} He^0 + M^{4+} + e_2.$$

In the non-coincidence spectra, see Figs. 4.4 and 4.5, the features A (AC(1,0)) and B (AC(2,0)) belong to this path. In the coincidence 2D-energy spectra, the events from this path are distributed in the region “AB”, see Figs. 4.10 and 4.18.

The sequential description is applicable in this path. The evidence are the following: (i) In the $He^{2+}$ non-coincidence spectrum, the feature A (AC(1,0)) is similar with the $He^{+}$ non-coincidence spectrum. (ii) The 2D-energy spectrum displays the "L" shaped distribution, which is expected by the sequential model. (iii) In the line scan spectra, see Figs. 4.11 and 4.19, the feature B (AC(2,0)) can only be clearly observed when $E_{fix}$ is in the energy range of feature A (AC(1,0)).

It should be noticed that, in ($\alpha$,2e), the highest energy of $e_2$ is about 4 eV higher than the highest energy of the electron emitted by the impact of primary $He^{+}$, $He^{+}$+M $\xrightarrow{AC}$ $He^{0}$+$M^{2+}$+$e$. It is well known that, for primary $He^{+}$, the most likely transition distance for AC is at the jellium edge, $z_{AC} = 0$, see Sec. 2.1.4. This corresponds to the atomic level shift, $\delta = 2$ eV. The atomic level shift for AC(1,0) is estimated to be $\delta_1$ = -2 eV. In ($\alpha$,2e), AC(1,0) follows AC(2,0). In the discussion of the $He^{2+}$ non-coincidence spectra, we have estimated that the most likely distance for AC(2,0) is about $z_{AC(2,0)}$ = 1.3 a.u. for Ir(100), 1.9 a.u. for O/Fe(100).

According to the calculation of the He-1s level in front of a metal surface, see Fig. 2.4, the atomic level shift $\delta_1$ = -2 eV corresponds to the distance $z$ = -1 a.u.. This is the most likely distance for AC(1,0). The velocity of the ion when AC(2,0) takes place, is about 0.017 a.u. for $He^{2+}$-Ir(100), and 0.015 a.u. for $He^{2+}$-O/Fe(100), from Eq. 2.7. Then the travel time for the ion to go from $z_{AC(2,0)}$ to $z_{AC(1,0)}$ is about 140 a.u. (3.2 fs) and 190 a.u. (4.6 fs). This number is reasonable, since in the vicinity of the jellium edge, the theoretical timescale for AC(1,0) is about $\tau_{AC(1,0)}$ = 100-1000 a.u (2.4-24 fs), see Sec. 2.1.5. This means that $z_{AC(1,0)}$ = -1 a.u. is a reasonable estimation.

(iii) Pair AC,

$$He^{2+} + M \xrightarrow{pair AC} He^{0} + M^{4+} + 2e.$$

In the coincidence 2D-energy spectra, the events due to this path are distributed in the energy range allowed by the pair emission, i.e. the region below $E_{sum}^{max}$. This has been proven in Figs. 4.8(a) and 4.16(a). The existence of the events in the region not allowed by the sequential model, i.e. the region outside "L" region, is the main proof of this path. In the non-coincidence spectra, the intensity between the features A and B can be explained by this path.

In the non-sequential path, the $He^{2+}$ is neutralized by a one-step. For the non-sequential path, we propose a pair AC process, in which the electron pair, instead of single electron, is treated as an entity. As shown in Fig. 5.3, a pair is captured by the $He^{2+}$, another pair from the surface is emitted taking away the excess energy. For an electron pair, there is no constraint on the energy of each electron. The two electrons can share the available energy continuously.

Similar cases, where an electron pair instead of a single electron acts as an entity, can be found in other Auger process. For example, a well known example is the double Auger decay [95, 96]. In this case, one electron from the outer shell can fill the hole left by the emission of a photoelectron, inducing the emission of two Auger electrons, see Fig. 5.4(a). The sum energy of the emitted two Auger electrons is well defined and the two emitted electrons can share the sum energy continuously. This indicates the emitted two electrons should be understood as an entity. Another example is for an ion with two inner shell vacancies and several electrons in the next out shell, which can be generated by photoionization or impact a bare ion onto a surface, it is possible

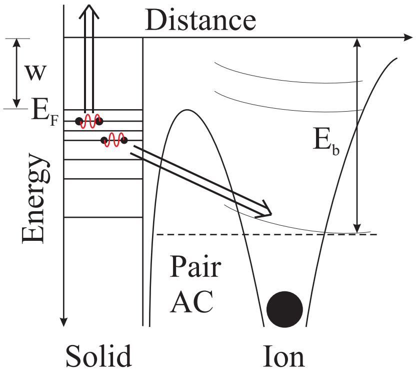
Distance
W
$E_F$
Energy
$E_b$
Pair
AC
Solid
Ion

**Figure 5.3:** Sketch of the pair Auger capture (pair AC) for $He^{2+}$, similar with (single electron) Auger capture (Fig. 2.3(b)), but here the pair electron is treated as an entity.

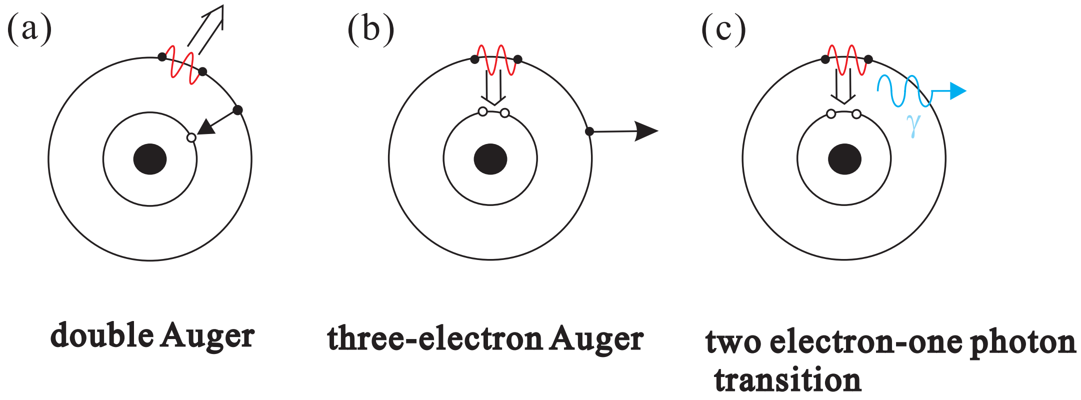
(a)
(b)
(c)
$\gamma$
double Auger
three-electron Auger
two electron-one photon transition

**Figure 5.4:** (a) Double Auger: one electron from the outer shell jump to fill one inner hole, leading to the emission of an electron pair. (b) Three-electron Auger: one electron pair from the outer shell jump to fill a double inner shell hole, leading to the emission of one Auger electron. (c) Two electron-one photon transition: similar with (b), but with one photon being emitted.

that the other shell electrons fill the two inner shell vacancies simultaneously, with one outer shell electron (Fig. 5.4(b)) or one photon being emitted (Fig. 5.4(c)). They are called three-electron Auger decay [42] and two electron-one photon transitions [43, 97], respectively.

To better understand the coexistence of the sequential and non-sequential path for the neutralization of $He^{2+}$, we recall the two-photon double ionization of He experiment, which can be seen as a reverse process of the ion neutralization. It has been theoretically demonstrated by Feist *et al* [98] that, a sequential path and a non-sequential path can coexist in the two-photon double ionization of He by an intense photon pulse ($\hbar\omega = 70$ eV), with a pulse duration from 100 as to few fs. The explanation is that if the time interval between the two photo-absorptions is sufficiently long, the two-photon double ionization will undergo a sequential path, $\mathrm{He} \xrightarrow{\hbar\omega} \mathrm{He}^{+}(1s) + e_1 \xrightarrow{\hbar\omega} \mathrm{He}^{2+} + e_2$. If the time interval between the two photo-absorptions is short, such that when the "second" electron ($e_2$) is ionized, the "first" electron ($e_1$) is still in the vicinity of the nucleus, the two electrons will interact each other and exchange an amount of energy [98]. In this case, the two-photon double ionization will undergo a non-sequential path. Since the time interval between the two photon absorptions is homogeneously distributed, from 0 to the pulse duration, the probability to choose a non-sequential/sequential path is finite. This theory, which is for the ionization process, could also be applicable in the ion neutralization process. To understand the choice between a sequential path and a non-sequential path for the neutralization of $He^{2+}$, the key is to know the time interval between the two electron emissions ($t_{12}$), and the timescale of the correlation between the two emissions.

For ($\alpha$,2e), the calculation of $t_{12}$ is a difficult task. This is because, first the ion is moving, where the electron takes place is uncertain. The transition rate is a function of the ion-surface distance, which increases for a smaller distance. Second, after the two electrons are removed, the response of the surface is a complicated dynamic many particle problem. Here, we propose a simple model. We assume that the transition rate ($1/\tau_2$) of the second emission is a constant value, i.e. independent of the ion-surface distance, and the electronic state of the surface and the ion. This is to say that, we assume $1/\tau_2$ to be the same as the transition rate of AC(1,0) in the sequential path. Since the most likely position for AC(2,0) and AC(1,0) is in the vicinity of the jellium edge, according to the theoretical calculations, see Sec. 2.1.5, $\tau_2$ in this regime is about 2.4-24 fs.

The Auger transition is an exponential decay. This has been demonstrated by time-resolved spectroscopy [99, 100]. In our simple model, after the "first" Auger electron is emitted ($t = 0$), the production rate of the "second" Auger electron is,

$$dN/dt = Cexp(-\frac{t}{\tau_2}), \tag{5.1}$$

where C is a constant. In this model, the mean of $t_{12}$ is $\tau_2$.

In previous, we have proposed four possible mechanisms for the interactions of the electrons involved in different emissions. The longest timescale is the timescale of the correlation between the two emissions, or to say the time needed to build up an intermediate state, $t_{inter}$. If $t_{12} > t_{inter}$, the sequential path is chosen. The probability to choose the sequential path is, exp(-$t_{inter}/\tau_2$), while 1 - exp(-$t_{inter}/\tau_2$) is for the non-

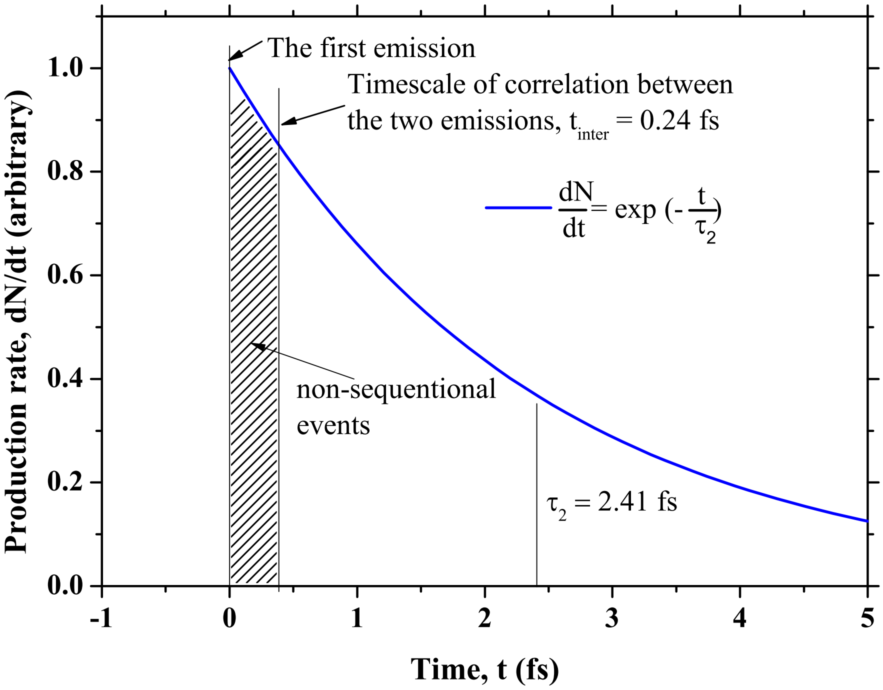

**Figure 5.5:** The production rate ($\mathrm{d}N/\mathrm{d}t$) of the "second" Auger electrons, as a function of the time. The first "Auger" electron is emitted at t = 0. We choose a possible value for the transition rate of the "second" Auger emission, $1/\tau_2 = 1/2.4$ fs$^{-1}$, and a possible value for the correlation between the two emissions, $t_{inter} = 0.24$ fs. The shaded area represents the number of the electron pairs, that the time interval between the two emission is smaller than $t_{inter}$. This is the number of non-sequential events.

.

sequential path. In our case, the timescales of the mechanisms (i), (iii) and (iv) are in the range of 0.05-0.3 fs, while the timescale of the mechanism (ii) is much shorter, 0.016 fs. The mechanisms (i), (iii) and (iv), determine $t_{inter}$. However, since the timescales of these mechanisms are close to each other, these mechanisms are entangled. Since our estimates are very rough, it is difficult to tell which mechanism dominates. We estimate that $t_{inter}$ could be in the range of 0.2-0.4 fs. The estimate for $\tau_2$ is 2.4-24 fs. Then, the relative contribution of the non-sequential path is estimated to be 1%-16%. We want to mention that, it is the ratio $t_{inter}/\tau_2$ that determines the relative contribution of the non-sequential path.

This model is exemplified in Fig. 5.5. We choose two possible values, $t_{inter} = 0.24$ fs and $\tau_2 = 2.4$ fs. The shaded area represents the number of the non-sequential pair emission events. In this case, the relative contribution of the non-sequential path is 10%.

In the real case, the transition rate is not constant, and the formula for $dN/dt$ can be more complicated. However, the point is, for ($\alpha$,2e), the electron emission/capture should be continuous. There is no reason for the second emission has to wait for that the first emission is completely finished. The probability to choose the non-sequential path is finite. From this point of view, the sequential description is only an approximation. According to our simple model, the sequential model is a good approximation, only when $\tau_2 \gg t_{inter}$. When $\tau_2 \ll t_{inter}$, the non-sequential path dominants. When $t_{inter}$ is comparable to $\tau_2$, the sequential path and the non-sequential path coexist.

# Chapter 6

# Conclusion

In this work, we have studied the electron pair emission by the impact of 10 eV $He^{2+}$ onto Ir(100) and O/Fe(100) surfaces. The neutralization of $He^{2+}$ can follow three paths: pair AC (non-sequential), AC(2,0)+AC(1,0) (sequential), and RC+KLL AI+AC(2,0) (sequential). The interesting observation is the coexistence of the sequential path (AC(2,0)+AC(1,0)) and the non-sequential path (pair AC). This can be explained by a theory developed for its reverse process, two-photon double ionization of He [98]. When the time interval ($t_{12}$) between the two electron ionizations/captures is larger than the time ($t_{inter}$) needed to build up a well defined intermediate state, the ionization/neutralization of $He^0$/$He^{2+}$ will undergo a sequential path. Otherwise, the non-sequential path will be chosen. If the mean of $t_{12}$ is comparable to $t_{inter}$, the probabilities to choose the sequential path and non-sequential path are comparable. The existence of the non-sequential path reflects the short time correlation between the two emissions.

For the neutralization of MCI with q $\geq$ 3, especially for a highly charged ion, the sequential neutralization model is more doubtful. Because more electrons are emitted in a very short time. Consider the case mentioned in the introduction, the impact of $Th^{79+}$ ion on a clean gold surface. According to Ref. [28], about 280 electrons are emitted in less than $10^{-13}$ s. In a sequential model, the average time interval between two successive emissions is less than 0.36 fs. In light of the study of ($\alpha$,2e), this time interval is too short to build up a well defined intermediate state. Therefore, in this case, the sequential neutralization model could be inappropriate.

# Bibliography

[1] E. Wigner and F. Seitz, *Phys. Rev.* **43**, 804 (1933).

[2] J. C. Slater, *Rev. Mod. Phys.* **6**, 209 (1934).

[3] P. Fulde, in *Electron correlations in molecules and solids*, Springer, 1991.

[4] B. D. Napitu and J. Berakdar, *Phys. Rev. B* **81**, 195108 (2010).

[5] J. Berakdar, *Phys. Rev. B* **58**, 9808 (1998).

[6] F. O. Schumann, L. Behnke, C. H. Li, J. Kirschner, Y. Pavlyukh, and J. Berakdar, *Phys. Rev. B* **86**, 035131 (2012).

[7] F. O. Schumann, L. Behnke, C. H. Li, and J. Kirschner, *J. Phys: Condens. Matter* **25**, 094002 (2013).

[8] F. O. Schumann, J. Kirschner, and J. Berakdar, *Phys. Rev. Lett.* **95**, 117601 (2005).

[9] F. O. Schumann, C. Winkler, and J. Kirschner, *New Journal of Physics* **9**, 372 (2007).

[10] F. O. Schumann, C. Winkler, and J. Kirschner, *Phys. Rev. Lett.* **98**, 257604 (2007).

[11] F. O. Schumann, C. Winkler, and J. Kirschner, *physica status solidi (b)* **246**, 1483 (2009).

[12] F. Giebels, H. Gollisch, R. Feder, F. O. Schumann, C. Winkler, and J. Kirschner, *Phys. Rev. B* **84**, 165421 (2011).

[13] F. O. Schumann, C. Winkler, J. Kirschner, F. Giebels, H. Gollisch, and R. Feder, *Phys. Rev. Lett.* **104**, 087602 (2010).

[14] G. A. van Riessen, F. O. Schumann, M. Birke, C. Winkler, and J. Kirschner, *J. Phys.: Condensed Matter* **20**, 442001 (2008).

[15] F. Giebels, H. Gollisch, and R. Feder, *J. Phys: Condens. Matter* **21**, 355002 (2009).

[16] H. D. Hagstrum, *Phys. Rev.* **150**, 495 (1966).

[17] H. Winter and J. Burgdörfer, *Slow Heavy-Particle Induced Electron Emission from Solid Surfaces*, Springer-Verlag, 2004.

[18] H. D. Hagstrum, *Phys. Rev.* **96**, 325 (1954).

[19] H. D. Hagstrum and G. E. Becker, *Phys. Rev.* **159**, 572 (1967).

[20] M. L. E. Oliphant, *Proc. R. Soc. London. Ser. A* **124**, pp. 228 (1929).

[21] H. D. Hagstrum, *Phys. Rev.* **96**, 336 (1954).

[22] S. Masuda, K. Sasaki, M. Sogo, M. Aoki, and Y. Morikawa, *Phys. Rev. A* **80**, 040901 (2009).

[23] H. Brenten, H. Müller, and V. Kempter, *Surf. Sci.* **274**, 309 (1992).

[24] D. Niemann, M. Grether, M. Rösler, and N. Stolterfoht, *Phys. Rev. Lett.* **80**, 3328 (1998).

[25] R. A. Baragiola and C. A. Dukes, *Phys. Rev. Lett.* **76**, 2547 (1996).

[26] P. Riccardi, A. Sindona, P. Barone, A. Bonanno, A. Oliva, and R. A. Baragiola, *Nucl. Instrum. Methods Phys. Res., Sect. B* **212**, 339 (2003).

[27] H. Eder, F. Aumayr, and H. Winter, *Nucl. Instrum. Methods Phys. Res., Sect. B* **154**, 185 (1999).

[28] F. Aumayr, H. Kurz, D. Schneider, M. A. Briere, J. W. McDonald, C. E. Cunningham, and H. Winter, *Phys. Rev. Lett.* **71**, 1943 (1993).

[29] L. Folkerts, S. Schippers, D. M. Zehner, and F. W. Meyer, *Phys. Rev. Lett.* **74**, 2204 (1995).

[30] P. A. Zeijlmans van Emmichoven, P. A. A. F. Wouters, and A. Niehaus, *Surf. Sci.* **195**, 115 (1988).

[31] J. Burgdörfer, P. Lerner, and F. Meyer, *Phys. Rev. A* **44**, 5674 (1991).

[32] A. Arnau, F. Aumayr, P. M. Echenique, M. Grether, W. Heiland, J. Limburg, R. Morgenstern, P. Roncin, S. Schippers, R. Schuch, N. Stolterfoht, P. Varga, T. J. M. Zouros, and H. P. Winter, *Surface Science Reports* **27**, 113 (1997).

[33] P. A. Zeijlmans van Emmichoven, C. C. Havener, and F. W. Meyer, *Phys. Rev. A* **43**, 1405 (1991).

[34] P. Varga, *Appl. Phys. A* **44**, 31 (1987).

[35] H. D. Hagstrum and G. E. Becker, *Phys. Rev. B* **8**, 107 (1973).

[36] A. Rudenko, L. Foucar, M. Kurka, T. Ergler, K. U. Kühnel, Y. H. Jiang, A. Voitkiv, B. Najjari, A. Kheifets, S. Lüdemann, T. Havermeier, M. Smolarski, S. Schössler, K. Cole, M. Schöffler, R. Dörner, S. Düsterer, W. Li, B. Keitel, R. Treusch, M. Gensch, C. D. Schröter, R. Moshammer, and J. Ullrich, *Phys. Rev. Lett.* **101**, 073003 (2008).

[37] Y. Nabekawa, H. Hasegawa, E. J. Takahashi, and K. Midorikawa, *Phys. Rev. Lett.* **94**, 043001 (2005).

[38] A. A. Sorokin, M. Wellhöfer, S. V. Bobashev, K. Tiedtke, and M. Richter, *Phys. Rev. A* **75**, 051402 (2007).

[39] S. Rioual, B. Rouvellou, L. Avaldi, G. Battera, R. Camilloni, G. Stefani, and G. Turri, *Phys. Rev. Lett.* **86**, 1470 (2001).

[40] M. Wiedenhoeft, S. E. Canton, A. A. Wills, T. Gorczyca, J. Viefhaus, U. Becker, and N. Berrah, *Journal of Physics B: Atomic, Molecular and Optical Physics* **41**, 095202 (2008).

[41] P. Lablanquie, S. Sheinerman, L. Andric, J. Palaudoux, Y. Hikosaka, K. Ito, and F. Penent, *Journal of Electron Spectroscopy and Related Phenomena* **185**, 198 (2012).

[42] L. Folkerts, J. Das, S. Bergsma, and R. Morgenstern, *Physics Letters A* **163**, 73 (1992).

[43] H. J. Andrä, A. Simionovici, T. Lamy, A. Brenac, G. Lamboley, J. J. Bonnet, A. Fleury, M. Bonnefoy, M. Chassevent, S. Andriamonje, and A. Pesnelle, *Z. Phys. D: At., Mol. Clusters* **21**, S135 (1991).

[44] G. A. van Riessen, Z. Wei, R. S. Dhaka, C. Winkler, F. O. Schumann, and J. Kirschner, *J. Phys.: Condensed Matter* **22**, 092201 (2010).

[45] B. Nieuwenhuys, R. Bouwman, and W. M. H. Sachtler, *Thin Solid Films* **21**, 51 (1974).

[46] K. O. Legg, F. Jona, D. W. Jepsen, and P. M. Marcus, *J. Phys. C: Solid State Physics* **10**, 937 (1977).

[47] M. Busch, S. Wethekam, and H. Winter, *Surf. Sci.* **605**, 733 (2011).

[48] M. Busch, S. Wethekam, and H. Winter, *Nucl. Instrum. Methods Phys. Res., Sect. B* **267**, 2625 (2009).

[49] T. Hecht, H. Winter, and A. Borisov, *Surface Science* **406**, L607 (1998).

[50] B. van Someren, P. A. Zeijlmans van Emmichoven, and A. Niehaus, *Phys. Rev. A* **61**, 022902 (2000).

[51] A typical value for the Fermi velocity is 1.57 × $10^6$ m/s for the case of Cu. The ion velocity in our case (10 eV $^3He^{2+}$) is 2.7 × $10^4$ m/s. This means in our case the image charge model is a proporiate description.

[52] J. Jackson, in *Classical Electrodynamics*, 1998.

[53] N. D. Lang and W. Kohn, *Phys. Rev. B* **7**, 3541 (1973).

[54] S. Wethekam, A. Mertens, and H. Winter, *Phys. Rev. Lett.* **90**, 037602 (2003).

[55] J. P. Briand, L. de Billy, P. Charles, S. Essabaa, P. Briand, R. Geller, J. P. Desclaux, S. Bliman, and C. Ristori, *Phys. Rev. Lett.* **65**, 159 (1990).

[56] W. More, J. Merino, R. Monreal, P. Pou, and F. Flores, *Phys. Rev. B* **58**, 7385 (1998).

[57] H. Winter, *Journal of Physics: Condensed Matter* **5**, A295 (1993).

[58] S. Wethekam, A. Mertens, and H. Winter, *Nuclear Instruments and Methods in Physics Research Section B: Beam Interactions with Materials and Atoms* **212**, 308 (2003).

[59] H. Winter, *Physics Reports* **367**, 387 (2002).

[60] M. A. Cazalilla, N. Lorente, R. D. Muiño, J.-P. Gauyacq, D. Teillet-Billy, and P. M. Echenique, *Phys. Rev. B* **58**, 13991 (1998).

[61] C. Tusche and J. Kirschner, Correlated double electron capture by slow helium ions above the surface, unpublished, 2012.

[62] Y. Ralchenko, A. E. Kramida, J. Reader, and N. A. Team., NIST Atomic Spectra Database (ver. 4.1.0)@ONLINE, 2012.

[63] E. Lindroth, *Phys. Rev. A* **49**, 4473 (1994).

[64] J. C. Slater, *Phys. Rev.* **36**, 57 (1930).

[65] N. Lorente and R. Monreal, *Surface Science* **303**, 253 (1994).

[66] S. Thurgate and C. Lund, *Journal of Electron Spectroscopy and Related Phenomena* **72**, 289 (1995).

[67] E. Jensen, R. A. Bartynski, S. L. Hulbert, and E. D. Johnson, *Review of Scientific Instruments* **63**, 3013 (1992).

[68] G. Stefani, R. Gotter, A. Ruocco, F. Offi, F. D. Pieve, S. Iacobucci, A. Morgante, A. Verdini, A. Liscio, H. Yao, and R. Bartynski, *Journal of Electron Spectroscopy and Related Phenomena* **141**, 149 (2004).

[69] R. Huber, F. Tauser, A. Brodschelm, M. Bichler, G. Abstreiter, and A. Leitenstorfer, *Nature* **414**, 286 (2001).

[70] A. S. Moskalenko, Y. Pavlyukh, and J. Berakdar, *Phys. Rev. A* **86**, 013202 (2012).

[71] F. O. Schumann, C. H. Li, L. Behnke, G. Di Filippo, G. Stefani, and J. Kirschner, Electron coincidence studies from S-overlayers on Cu(100) and Ni(100), Unpublished manuscript, 2013.

[72] M. Ohno, *J. Electron. Spectrosc. Relat. Phenom.* **162**, 134 (2008).

[73] Y. Ma, P. Rudolf, E. E. Chaban, C. T. Chen, G. Meigs, and F. Sette, *Phys. Rev. B* **41**, 5424 (1990).

[74] A. Borisov, D. Sánchez-Portal, R. Díez Muiño, and P. M. Echenique, *Chemical Physics Letters* **387**, 95 (2004).

[75] P. F. Robusto and R. Braunstein, *physica status solidi (b)* **107**, 443 (1981).

[76] O. Gunnarsson and K. Schönhammer, *Phys. Rev. B* **22**, 3710 (1980).

[77] G. A. Sawatzky, Auger Photoelectron Coincidence Spectroscopy, in *Treatise on materials science and technology*, volume 30, pp. 168–243, Academic Press, New York, 1988.

[78] N. W. Ashcroft and D. N. Mermin, Solid state physics, Thomson Learning, Toronto, 1 edition, 1976.

[79] P. Hayes, M. A. Bennett, J. Flexman, and J. F. Williams, *Rev. Sci. Instrum.* **59**, 2445 (1988).

[80] O. Kugeler, S. Marburger, and U. Hergenhahn, *Review of Scientific Instruments* **74**, 3955 (2003).

[81] *User's manual of 3300 SERIES MCP RAE SENSOR.*

[82] C. Tusche and J. Kirschner, A low energy ion source for electron capture spectroscopy, unpublished, 2012.

[83] *User's manual of Ion Source IQE 12/38.*

[84] *SIMION sold by Scidentific Instruments Services Inc.*

[85] K. Zakeri, T. R. F. Peixoto, Y. Zhang, J. Prokop, and J. Kirschner, *Surf. Sci.* **604**, L1 (2010).

[86] A. Tange, C. L. Gao, B. Y. Yavorsky, I. V. Maznichenko, C. Etz, A. Ernst, W. Hergert, I. Mertig, W. Wulfhekel, and J. Kirschner, *Phys. Rev. B* **81**, 195410 (2010).

[87] The calculation is done by Dr.Ernst in Max-Planck-Institute, using the self-consistent KKR Green's-function method.

[88] H. D. Hagstrum, Y. Takeishi, and D. D. Pretzer, *Phys. Rev.* **139**, A526 (1965).

[89] S. Schippers, S. Oelschig, W. Heiland, L. Folkerts, R. Morgenstern, P. Eeken, I. Urazgil'din, and A. Niehaus, *Surf. Sci.* **257**, 289 (1991).

[90] S. Wethekam, M. Busch, and H. Winter, *Surface Science* **603**, 209 (2009).

[91] F. O. Schumann, R. S. Dhaka, G. A. van Riessen, Z. Wei, and J. Kirschner, *Phys. Rev. B* **84**, 125106 (2011).

[92] J. H. Weaver, C. G. Olson, and D. W. Lynch, *Phys. Rev. B* **15**, 4115 (1977).

[93] L. Plucinski, Y. Zhao, B. Sinkovic, and E. Vescovo, *Phys. Rev. B* **75**, 214411 (2007).

[94] Y. Sakisaka, T. Miyano, and M. Onchi, *Phys. Rev. B* **30**, 6849 (1984).

[95] J. Viefhaus, S. Cvejanović, B. Langer, T. Lischke, G. Prümper, D. Rolles, A. V. Golovin, A. N. Grum-Grzhimailo, N. M. Kabachnik, and U. Becker, *Phys. Rev. Lett.* **92**, 083001 (2004).

[96] F. Penent, J. Palaudoux, P. Lablanquie, L. Andric, R. Feifel, and J. H. D. Eland, *Phys. Rev. Lett.* **95**, 083002 (2005).

[97] J. Hoszowska, J.-C. Dousse, J. Szlachetko, Y. Kayser, W. Cao, P. Jagodziński, M. Kavčič, and S. H. Nowak, *Phys. Rev. Lett.* **107**, 053001 (2011).

[98] J. Feist, R. Pazourek, S. Nagele, E. Persson, B. I. Schneider, L. A. Collins, and J. Burgdörfer, *Journal of Physics B: Atomic, Molecular and Optical Physics* **42**, 134014 (2009).

[99] M. Drescher, M. Hentschel, R. Kienberger, M. Uiberacker, V. Yakovlev, A. Scrinzi, T. Westerwalbesloh, U. Kleineberg, U. Heinzmann, and F. Krausz, *Nature* **419**, 803 (2002).

[100] T. Shimizu, T. Sekikawa, T. Kanai, S. Watanabe, and M. Itoh, *Phys. Rev. Lett.* **91**, 017401 (2003).

# Appendix A

Fig. 6.1 shows the filter box mentioned in Sec. 3.2.2. It has three functions, reduce the noise, distribute the voltage into different units, and extract the MCP pulse signal.

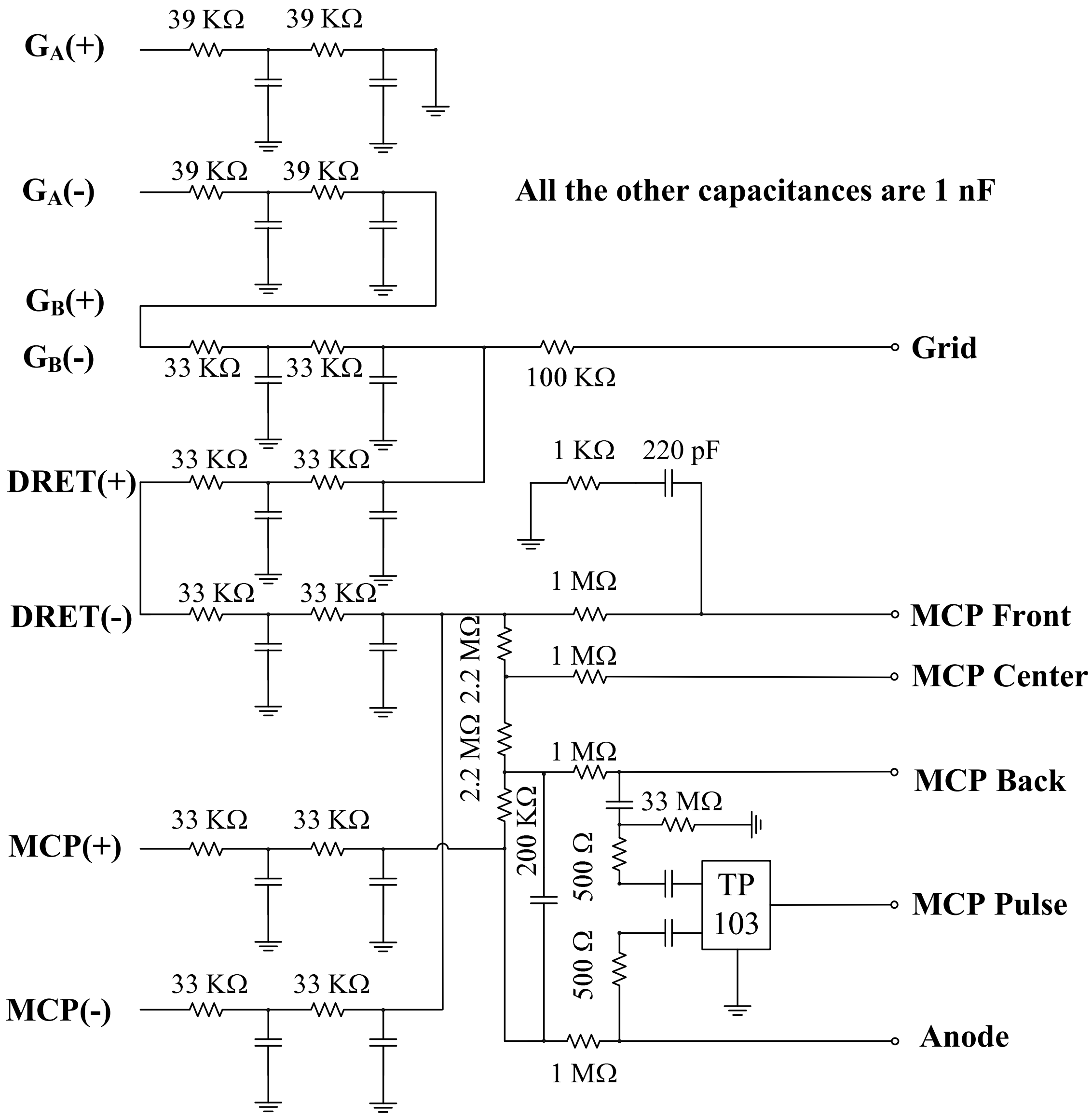

39 KΩ
39 KΩ
GA(+)
39 KΩ
39 KΩ
GA(-)
All the other capacitances are 1 nF
GB(+)
GB(-)
33 KΩ
33 KΩ
100 KΩ
Grid
33 KΩ
33 KΩ
1 KΩ
220 pF
DRET(+)
33 KΩ
33 KΩ
1 MΩ
DRET(-)
MCP Front
2.2 MΩ
2.2 MΩ
1 MΩ
MCP Center
1 MΩ
MCP Back
33 MΩ
200 KΩ
500 Ω
TP
103
MCP Pulse
500 Ω
33 KΩ
33 KΩ
MCP(+)
33 KΩ
33 KΩ
MCP(-)
Anode
1 MΩ

**Figure 6.1:** The filter box

# Appendix B

There are two different kinds of atomic units, Hartree atomic units and Rydberg atomic units. In this thesis, we use the Hartree atomic units, which are widely used in the atomic physics. The below table shows the Hartree atomic units and the values. $\alpha$ is the fine-structure constant.

**Table 6.1:** Atomic units

| Hartree atomic unit | Definition | Value |
|---|---|---|
| length | Bohr radius $a_0$ | $5.29\times10^{-11}$ m |
| velocity | velocity of an electron in the first Bohr orbit $\alpha$c | $2.18\times10^{6}$ m/s |
| time | $a_0/\alpha$c | $2.41\times10^{-17}$ s |
| energy | twice the binding energy of hydrogen $m_e(\alpha \mathrm{c})^2$ | $4.36\times10^{-18}$ J (27.211 eV) |
| mass | electron mass $m_e$ | $9.10\times10^{-31}$ kg |
| charge | electron charge $e$ | $1.60\times10^{-19}$ C |
| Reduced Planck's constant | $\hbar$ | $6.58\times10^{-16}$ eV·s |
| Coulomb's constant | $1/(4\pi\epsilon_0)$ | $8.98\times10^{9}$ Nm$^2$/C$^2$ |

# Acknowledgments

At the end of my thesis I would like to express my gratitude to the people who have given their supports to me during this work.

First and foremost, I would like to thank my advisor Prof. Jürgen Kirschner, for giving me a chance to pursue my Ph. D. in Max-Planck-Institut für Mikrostrukturphysik. The electron coincidence research project is quite interesting and fundamental. I thank for his continuous support and guidance. I am deeply impressed by his persistence and enthusiasm in physics. I wish him good health and more "coincidence" in the future.

I would like to thank Dr. Schumann. Thanks for taking care of me with experiments and teaching me how to present the data in a scientific manner.

I would like to thank Dr. Tusche for the collaboration in the ($\alpha$,2e) experiments, especially for the pioneer work for the ($\alpha$,2e) experiments. Thanks for the numerous and fruitful discussions we have had.

I would like to thank Prof. Winter. When I have a lot of puzzles for the ($\alpha$,2e) experiments, I go to ask help from him, because he is professional in the field of ion neutralization. Prof. Winter is very nice, and has given me a lot of useful advice.

I would like to thank Dr. Ernst, for the calculations of the surface DOS of Ir(100).

My sincere thanks also go to Dr. Wei, Dr. Swapnil, Dr. Dhaka, Dr. Huth, Miss Behnke and Mr. Brandt. It has been a happy time to work with you all. Thank you for the help in the experiments.

I would like to acknowledge the excellent technique support from Mr. Helbig, Mr. Neumann for their assistance at Halle, and from Dr. Mahler and Miss. Zada at the BESSY beam line.

Last but most importantly, I would like to thank my parents and my wife, for all the love and support.

# Eidesstattliche Erklärung

Ich erkläre hiermit, dass ich keine anderen als die von mir angegebenen Quellen und Hilfsmittel zur Erstellung meiner Dissertation verwendet habe. Den benutzten Werken wörtlich oder inhaltlich entnommene Stellen sind als solche gekennzeichnet.

Changhui Li

Halle (Saale), December 2014

# Curriculum vitae

| | |
|---|---|
| First Name | Chang-Hui |
| Family Name | Li |
| Date of Birth | June 13, 1982 |
| Place of Birth | Liaoning, China |
| Nationality | P. R. China |
| E-mail | chli@mpi-halle.de |

## EDUCATION

| | |
|---|---|
| Sep. 2000 - Jul. 2004 | University of Science and Technology of China (Hefei, China)<br>Department of Physics<br>Bachelor of Science |
| Sep. 2005 - Jan. 2008 | Graduate University of Chinese Academy of Sciences (Beijing, China)<br>Institute of Physics<br>Master of Science |
| Since July. 2009 | Max-Planck Institute of Microstructure Physics<br>and Martin-Luther-Universität Halle-Wittenberg<br>Ph. D. candidate (Supervisor: Prof. Jürgen Kirschner) |

Li, Chang-Hui

Halle (Saale), December 2014

# Publications

**Articles**:

**Li, C. H.**, Zhang, X. Q., Cheng, Z. H., and Sun, Y. *Room temperature giant dielectric tunability effect in bulk* $LuFe_2O_4$. Appl. Phys. Lett. **92**, 182903 (2008).

**Li, C. H.**, Zhang, X. Q., Cheng, Z. H., and Sun, Y. *Electric field induced phase transition in charge-ordered* $LuFe_2O_4$. Appl. Phys. Lett. **93**, 152103 (2008).

Liu, Y., **Li, C. H.**, Zhang, X. Q., Cheng, Z. H., and Sun, Y. *Influence of Mg doping on the giant dielectric tunability in* $LuFe_2O_4$. J. Appl. Phys. **104**, 104112 (2008).

**Li, C. H.**, Wang, F., Liu, Y., Zhang, X. Q., Cheng, Z. H., and Sun, Y. *Electrical control of magnetization in charge-ordered multiferroic in* $LuFe_2O_4$. Phys. Rev. B **79**, 172412 (2009).

**Li, C. H.**, Liu, Y., Wang, F., Luo, X., Zhang, Sun, Y. P., X. Q., Cheng, Z. H., and Sun, Y. *Photoinduced Magnetization Change in Multiferroic* $YbFe_2O_4$. Chin. Phys. Lett. **26**, 127501 (2009).

Shen, X., Xu, C. H., **Li, C. H.**, Zhang, Y., Zhao, Q., Yang, H. X., Sun, Y., Li, J. Q., Jin, C. Q., and Yu, R. C. *Pressure effects on multiferroic* $LuFe_2O_4$. Appl. Phys. Lett. **96**, 102909 (2010).

Vitucci, F. M., Nucara, A., Nicoletti, D., Sun, Y., **Li, C. H.**, Soret, J. C., Schade, U., and Calvani, P. *Infrared study of the charge-ordered multiferroic* $LuFe_2O_4$. Phys. Rev. B **81**, 195121 (2010).

Wang, F., **Li, C. H.**, Zou, T., Sun, Y., Liu, Y., Sun, Y. *Electrically driven magnetic relaxation in multiferroic* $LuFe_2O_4$. J. Phys.: Condens. Matter **22**, 496001 (2010).

Liu, Y., Zou, T., Wang, F., **Li, C. H.**, Zheng, L., and Sun, Y. *Percolative effects and giant dielectric tunability of* $BaTiO_3$-$LuFe_2O_4$ *composites.* Physica B **406**, 1263 (2011).

Xu, C. H., Shen, X., **Li, C. H.**, Sun, Y., Zhao, Q., Jin, C. Q., and Yu, R. C. *The transport properties of* $Pr_{1.2}Sr_{1.8}Mn_2O_7$ *and* $PrSr_2Mn_2O_7$ *under pressure.* J. Appl. Phys. **110**, 073705 (2011).

Schumann, F. O., Behnke, L., **Li, C. H.**, Kirschner, J., Pavlyukh, Y., and Berakdar, J. *Electron pair emission from a highly correlated material.* Phys. Rev. B **86**, 035131 (2012).

Schumann, F. O., Behnke, L., **Li, C. H.**, Kirschner, J. *Exploring highly correlated materials via electron pair emission: the case of NiO/Ag(100).* J. Phys.: Condens. Matter **25**, 094002 (2013).

**Talks**:

**Li, C. H.**, Patil, S., Wei, Z., Behnke, L., Schumann, F. O., di Filippo, G., Stefani, G., and Kirschner, J. *Electron coincidence studies from S-overlayers on Cu(100) and Ni(100).* Frühjahrstagung der Sektion Kondensierte Materie der Deutschen Physikalischen Gesellschaft, Berlin, Germany (2012).

**Posters**:

Behnke, L., **Li, C. H.**, Schumann, F. O., and Kirschner, J. *Electron pair emission from NiO(100).* Frühjahrstagung der Sektion Kondensierte Materie der Deutschen Physikalischen Gesellschaft, Dresden, Germany (2011).

Behnke, L., **Li, C. H.**, Schumann, F. O., and Kirschner, J. *Electron pair emission from NiO(100).* International Symposium on (e,2e), Double-ionization & Related Topics, Dublin, Ireland (2011).

**Li, C. H.**, Tusche, C., Behnke, L., Schumann, F. O., and Kirschner, J. *Electron pair emission from surfaces upon* $He^{2+}$ *impact.* International Conference on Many Particle Spectroscopy of Atoms, Molecules, Clusters and Surfaces, Berlin, Germany (2012).

**Li, C. H.**, Tusche, C., Behnke, L., Schumann, F. O., and Kirschner, J. *Electron pair emission from surfaces upon* $He^{2+}$ *impact.* Frühjahrstagung der Sektion Kondensierte Materie der Deutschen Physikalischen Gesellschaft, Regensburg, Germany (2013).